Functional Polymer Coatings

μ-Patterning and μ-Analysis

Dissertation

zur Erlangung des Grades
Doktor der Naturwissenschaften

Am Fachbereich Chemie, Pharmazie und Geowissenschaften
der Johannes Gutenberg-Universität Mainz

Sebastian Karl Borromäus Nett
geboren in Memmingen
Mainz, Januar 2009

Dekan: ...
Erstgutachter: ...
Zweitgutachter: ...
Datum der mündlichen Prüfung: 29.05.2009

Die vorliegende Arbeit wurde am Institut für Physikalische Chemie der
Johannes-Gutenberg Universität Mainz
und am Max-Planck-Institut für Polymerforschung in Mainz
unter der Betreuung von

Prof. Dr. ...

in der Zeit von März 2006 bis März 2009 angefertigt.

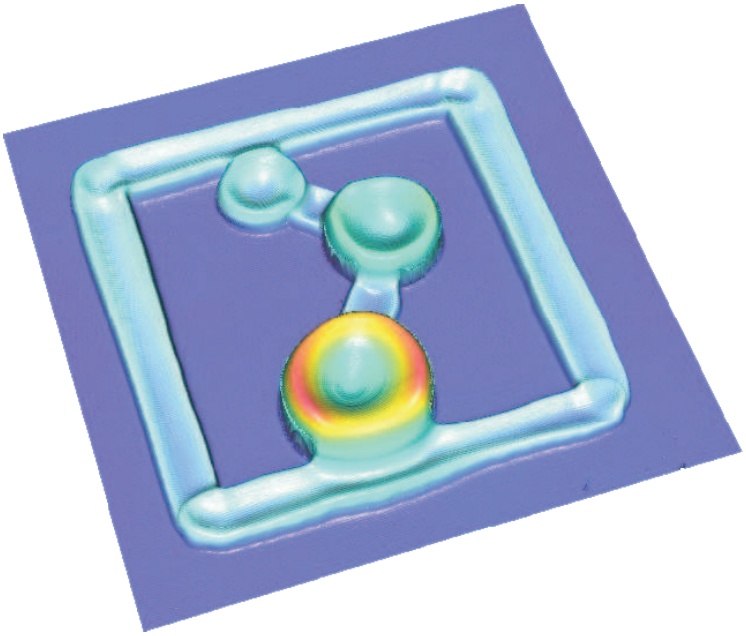

Alle Weisheit kommt vom Herrn und ist bei ihm auf ewig.
Die Bibel, Sir 1,1.

Für meine Familie.

Contents

1. Introduction

Surfaces and interfaces play an important role in many situations of daily life. Endless applications range from natural surfaces [1] like skin [2], the lotus leaf [3] or the feet of a gecko [4], over various processes like catalysis [5], filtration [6], chromatography [7], to industrial products such as paintings [8], adhesives [9] or lubrication [10]. In all cases the properties and the structure of the molecules close to the interface are essential compared to the bulk properties [11]. Controlling the part at the interface is of high importance.
Since the development of synthetic polymers other materials e.g. wood, metals and many more were displaced in a lot of applications . Because one of the major advantages is that the physical properties (elasticity, friction, density, optical properties, polarity...) can be altered very specifically through controlled synthesis [12, 13]. Thus, polymers are under extensive investigation to tailor surfaces. Polymerbrushes [14] and polyelectrolytes [15] are well known examples to coat surfaces.
A key feature is the ability to process polymers from solution which is advantageous compared to more complex procedures such as vapor depositioning in vacuum. Established techniques are cast-, spin-, blade-, and spraycoating. Besides simple covering of an interface by a polymer, structuring of the interface from the micro to the nanoscale is of equal importance e.g. to get microelectronic devices [16], microelectromechanical systems (MEMS) [17], microfluidic devices [18], microlenses [19], and more. Recently inkjet printing [20,21] gathered a lot of attention because of the ability to "directly write" [22] patterns on surfaces. Droplets in the volume range of micro- to picoliter can be placed on substrates precisely with modern inkjet devices consisting of a x/y/z translation stage and a print head. Through inkjet printing microstructures can be prepared even onto microdevices used as substrates [23].
Nanomechanical cantilever sensors (NCS) are an established sensoric system

in the field of MEMS [24, 25]. In order to deal with NCS certain scientific difficulties have to be overcome. First, the cantilevers need to be coated single sided with a functional layer for sensing purposes. Second the layer quality has to be checked with appropriate tools which are sufficient surface sensitive such as atomic force microscopy (AFM) [26], optical confocal microscopy [27], ellipsometry [28] and μ-grazing incidence small angle x-ray scattering [29]. However, NCS itself is used as a sensing platform for various purposes such as biomolecules, physical properties, thermal response and mass change. So, the data obtained from measurements performed on NCS give insight into the probed system and turn NCS into a prospective analytical tool.

The main focus of this thesis is the development of new methods to coat and pattern surfaces on the micro scale (chapter 3 and 4) and new methods to analyze micro structures (chapter 5 and 6).
In order to investigate fundamental reactions in small volumes, a poly(methyl methacrylate) (PMMA) polymer brush was synthesized in the confined geometry of a micro droplet of ionic liquid (IL) 1-butyl-3-methylimidazolium hexafluorophosphate ([Bmim][PF_6]) at room temperature, described in chapter 3. Another advantage of IL may be the replacement of the conventional, mostly toxic solvents in organic synthesis towards "green chemistry".
Solvent droplets were deposited onto a polymeric surface by drop-on-demand inkjet printing for producing microlenses, discussed in chapter 4.1. A combination of the phenomena of solvation and the coffee-stain effect led to craters. These spherical shaped cavities were verified by fitting a circle profile to each cavity. Secondly, polyelectrolyte multilayer (PEM) films made from poly(allylamine hydrochloride) (PAH) and poly(styrene sulfonate) (PSS) were formed layer by layer 3D-structures on silicon (chapter 4.2) and onto nanomechanical cantilever sensors (NMC) using drop-on-demand inkjet printing. The PEM coated cantilevers were probed as an humidity sensor (chapter 5.2). Chapter 5.1 focuses on the thermally responsive polymer coatings that were fabricated onto the cantilever sensors as well. Exemplarily two different types of these systems were investigated poly(N-isopropylacrylamide) (PNIPAM) and plasma polymerized N,N-diethylacrylamide (ppDEA). Chapter 6 picks up cantilever sensors and polyelectrolyte multilayer structures to be studied

by μ-reflectivity and μ-GISAXS to gain complementary results to the ellipsometric data.

2. Methods

2.1. Ellipsometry

Ellipsometry is a method to characterize the optical properties of thin layers [28, 30]. The basic principle of the measurement is the change in the polarization state of the light which is interacting with the sample. Parameters such as refractive index, film thickness, surface roughness and crystallinity can be determined. A suitable model of the layer system has to be chosen to calculate the desired parameter from the measured ellipsometric angles Ψ and Δ.

A monochromatic and polarized beam of light is an electromagnetic wave with the wave vector $\vec{E}$. The state of polarization can be described by two orthogonal electric waves (see figure 2.1). One is oriented parallel $\vec{E}_p$ the other perpendicular $\vec{E}_s$ to the sample surface. The two waves can have a phase shift $\xi_{s/p}$ to each other.

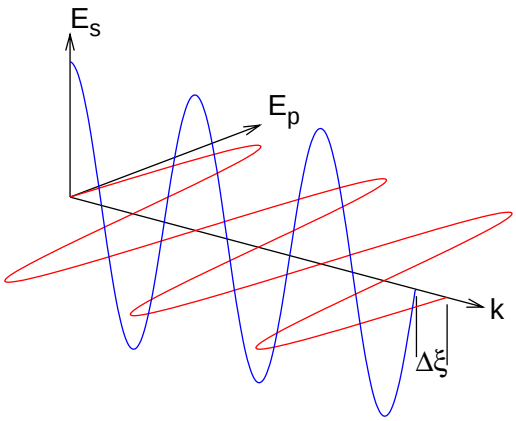

Fig. 2.1.: Schematic drawing of an electromagnetic wave. The state of polarization can be described as two orthogonal electric waves with the wave vector $\vec{E}_s$ and $\vec{E}_p$ [31].

When a beam of light enters a transparent film on a reflecting substrate, the state of polarization changes (see figure 2.2). The state of polarization depends on the wavelength, the incident angle, the refractive index and the thickness of the layer. This results is a change in the relation between the amplitudes of the incident wave E^i and the reflected wave E^o, which is determined by Ψ (eq.2.1):

$$\tan(\Psi) = \frac{|E_p^o|/|E_s^i|}{|E_p^o|/|E_s^i|} = \frac{|R_p|}{|R_s|} \tag{2.1}$$

In contrast Δ holds the information of the phase shift (eq. 2.2):

$$\Delta = (\xi_p^i - \xi_s^i) - (\xi_p^o - \xi_s^o) \tag{2.2}$$

Combining the two equations for the ellipsometric angles one obtains the fundamental equation of ellipsometry 2.3.

$$\tan(\Psi)\exp(i\Delta) = \frac{R_p}{R_s} \tag{2.3}$$

The most used type of ellipsometer is a ***P**olarizer–**C**ompensator– **S**ample–**A**nalyzer–Null–Ellipsometer* (see fig. 2.3)
The name is composed of the optical components in the following order: As light source a laser or a Xenon-lamp (with monochromator) is typically used. The first polarizer polarizes the monochromatic light circular to get an angle independent light intensity. This is followed by a second polarizer, compensator and analysator. The compensator is put at the fixed value of $\pm 45°$. Now

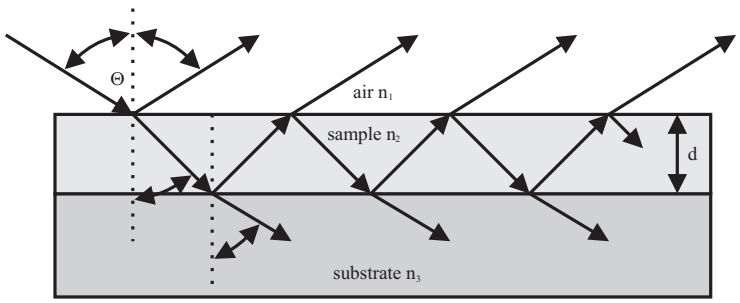

Fig. 2.2.: Reflection and transmission of an incidence beam of light in a multilayer system [32].

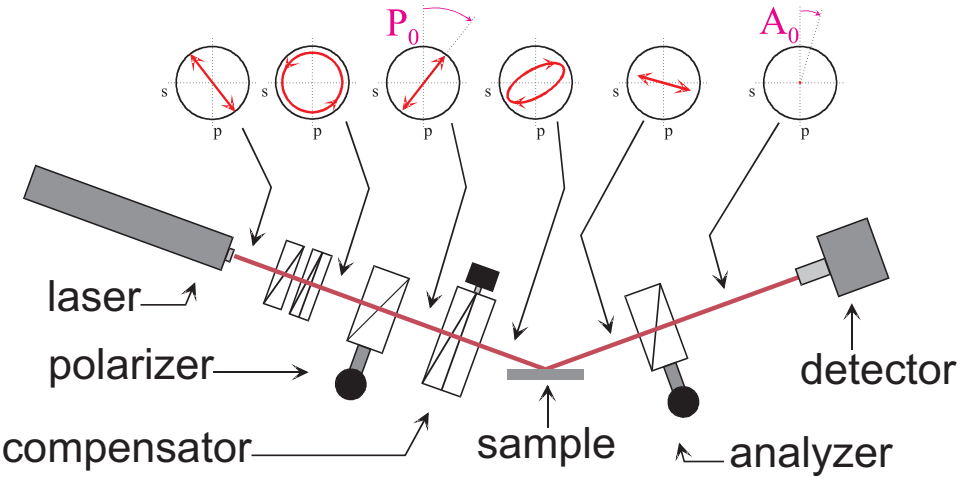

Fig. 2.3.: Setup of a PCSA-Null-Ellipsometers. The polarization state is drawn after every optical component. [31]

the polarizer before the sample and the analysator after the sample are rotated until the intensity at the detector is minimal. Ψ and Δ are calculated from the known position of polarizer, compensator and analyzer. This setup has the advantage that the setup is simple and errors are minimized. Because of the fixed angle C of the compensator the following mathematical expression is derived (eq. 2.4):

$$\tan(\Psi)\exp(i\Delta) = \frac{R_p}{R_s} = \pm\tan A_0 \exp\left[i\left(2P_0 + \frac{\pi}{2}\right)\right] \quad \text{if} \quad C = \pm 45^\circ \tag{2.4}$$

$$\Longrightarrow (\hat{P}_0, \hat{A}_0) = (P_0 + 90^\circ, 180^\circ - A_0) \quad \text{if} \quad I(P_0, A_0) = 0 \tag{2.5}$$

If a pair of polarizer and analyzer angles match the condition $I(P_0, A_0) = 0$ a further pair of angles will be given according to equation (2.5). Different pairs of angles are corresponding to different zones:

$$\underline{\text{Zone 1+3:}} \quad \Psi = |A_0| \quad \Delta = 2P_0 \pm 90^\circ \quad \text{if} \quad C = -45^\circ \tag{2.6}$$

$$\underline{\text{Zone 2+4:}} \quad \Psi = |A_0| \quad \Delta = -2P_0 \pm 90^\circ \quad \text{if} \quad C = +45^\circ \tag{2.7}$$

Therefore 8 varying pairs of angles are existing. A 4-zone measurement is averaging inaccuracy of the motors for the polarizers. Every material in the

layer system is characterized by both the refractive index and the layer thickness. In order to get valuable information from the ellipsometric angles Ψ and Δ a box model is assumed for the specimen consisting of the individual layers. A fit is applied to solve the unknown parameter. The layer thickness is periodic for a given pair of Ψ and Δ. This ambiguousness can be solved by measuring a variety of the incident angles. Thereby the number of data points for the fit is increased.
The measurements were performed on an imaging ellipsometer EP^3 from Nanofilm Technologies GmbH, Göttingen. The light source is a laser with the wavelength of $\lambda = 532\ nm$ and a xenon lamp having a wavelength range from 403 nm to 1000 nm. For all measurement in this thesis the incident angle was set to an angle of interest (AOI) = 60° if not described else. In order to image a part of the surface the laser beam is widened additionally with the optics of a microscope. The ellipsometric angles can be determined for every pixel or averaged over parts (ROI: Region of interest) of the field of view (0.22 mm). Inside the field of view several ROI's can be defined and analyzed individually. In figure 2.4 a typical box model is illustrated. The model consists of the silicon substrate covered by silicon oxide (n = 1.4603), ATRP initiator (n = 1.46) coupled by a silane and the polymer brush layer (PMMA: n = 1.49, PNIPAM: n = 1.5).

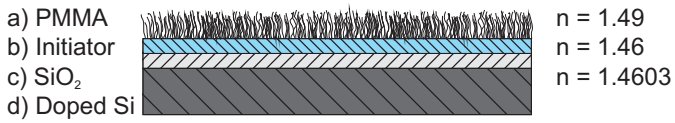

Fig. 2.4.: A box model for polymerbrush layers consisting of the silicon substrate covered by silicon oxide (n = 1.4603), ATRP initiator (n = 1.46) coupled by a silane and the polymer brush layer (PMMA: n = 1.49, PNIPAM: n = 1.5)

2.2. X-ray Reflectivity

X-ray reflectivity is a useful tool to study surface properties like thickness, roughness and density [33, 34]. The x-rays penetrate the sample and interact with the matter density. Therefore, it is a non destructive method and reveals structural information beneath the film surface which is easy to obtain

compared to microscopic methods like scanning probe microscopy or optical microscopy.
A x-ray reflectivity experiment is conducted as following, the sample surface is illuminated by a highly collimated x-ray beam under a very small incidence angle. The intensity of the direct reflected beam is monitored ($\alpha_i = \alpha_f$) as a function of the incidence angle close to the critical angle of the material.
The spectrum shows a sharp edge at the critical angle. The specular intensity decreases rapidly for angles $> \alpha_c$ according to a power-law. Depending on the structural properties of the sample a characteristic decay is obtained. Upon the presence of surface layers the curve exhibits an interference pattern so called Kiessig fringes.
When the x-ray beam hits an interface, reflection ($\theta_i = \theta$) and refraction occur (see figure 2.5). This relation is described in a classical model by the index of refraction:

$$n = 1 - \delta - i\beta \tag{2.8}$$

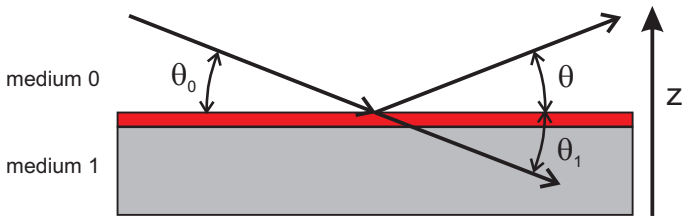

Fig. 2.5.: An incident beam is reflected and refracted at an interface.

The δ term accounts for the scattering of the x-rays and dependents on the electron density ρ_{el} and the wavelength λ. For a copper source λ = 1.5418 Å. r_0 is the classical radius of an electron.

$$\delta = \frac{\lambda^2 \rho_{el} r_0}{2\pi} \tag{2.9}$$

The β term stands for the mass absorption μ.

$$\beta = \frac{\lambda \mu}{4\pi} \tag{2.10}$$

Snell's law (eq. 2.11) determines the beam refraction by the ratio between the refractive indices of medium 0 and 1 (n_0 and n_1). A typical value for δ is in

the order of 10^{-6} while β is 2 to 3 orders of magnitude smaller. Therefore, the materials refractive index is < 1, but close to unity using x-rays.

$$n_0 cos(\theta_0) = n_1 cos(\theta_1) \tag{2.11}$$

For air and vacuum the refractive index is 1. Therefore, at an air/ specimen interface n_0/n_1 is smaller than 1 and total reflection occurs.

$$n_0 cos(\theta_c) = n_1 \tag{2.12}$$

Combining Snell's law with the expression of the critical angle leads to:

$$n_1^2 sin^2(\theta_1) = n_0^2 sin^2(\theta_0) - n_0^2 sin^2(\theta_c) \tag{2.13}$$

Because in the geometry of a reflectivity experiment the detection angle is set equal to the angle of incidence. Thus, the z component of the wavevector is of interest. Equation 2.13 can be rewritten into the notation of the wavevector (normal to the surface $k_{z0} = (2\pi/\lambda)sin\theta$):

$$k_{z1} = (k_{z0}^2 - k_{zc}^2)^{\frac{1}{2}} \tag{2.14}$$

At the air or vacuum interface of a specimen the reflection coefficient r_{01} is given by:

$$r_{01} = \frac{k_{z0} - k_{z1}}{k_{z0} + k_{z1}} \tag{2.15}$$

The fraction of the reflected beam intensity is the so called Fresnel reflectivity R:

$$R = \left| \frac{k_{z0} - k_{z1}}{k_{z0} + k_{z1}} \right|^2 \tag{2.16}$$

A system is considered which is composed of a substrate (medium 2) with a single layer on top (medium 1) in contact with air/ vacuum (medium 0) (see figure 2.6).
There are two interfaces with a given distance d. At each interface the x-ray beam is reflected and refracted. The reflection coefficients at the interface be-

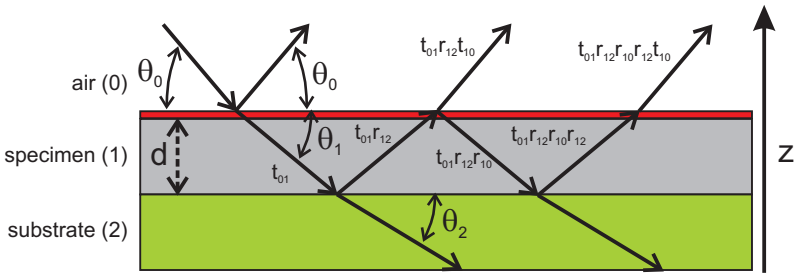

Fig. 2.6.: Reflection and refraction at a multilayer system.

tween substrate and the sample r_{12} and between the sample and air/ vacuum r_{01} are crucial. Then the reflectance is described as follows:

$$r = \frac{r_{01} + r_{12} exp(2ik_{zi}d)}{1 + r_{01}r_{12} exp(2ik_{z1}d)} \tag{2.17}$$

and the reflectivity is

$$R = \left| \frac{r_{01} + r_{12} exp(2ik_{zi}d)}{1 + r_{01}r_{12} exp(2ik_{z1}d)} \right|^2 \tag{2.18}$$

In soft matter science this equation is applicable for most of the samples e.g. figure 2.7 shows a simulated reflectivity profile of a sample containing a 250 Å polystyrene film on a silicon substrate. The surface roughness for both interfaces is 5 Å.

The typical pattern so called Kiessig fringes represent the finite thickness of the sample layer. The distance between two successive minima results in the thickness directly from the relation:

$$d = \frac{2\pi}{\Delta k_z} \tag{2.19}$$

2.2.1. Roughness

Up to now just infinitely sharp interfaces (2.8(a)) were considered, but this is generally not true for more realistic samples [33,34]. Under real conditions exists a density gradient from one interface to the next e.g. air/ sample, sample/ substrate. This results in a reduction in the reflectivity from that interface. It can be distinguished between waviness and roughness of an interface (2.8(b)

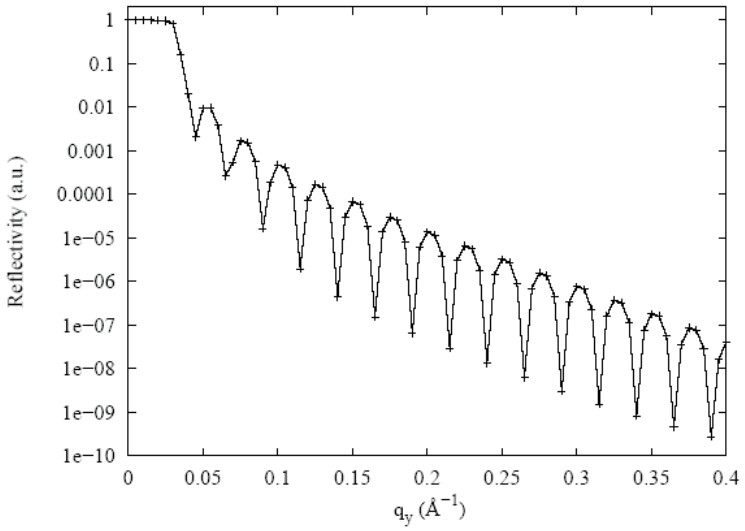

Fig. 2.7.: Simulated reflectivity curve of a polystyrene film (PS) with a thickness of 25 nm. The roughness σ_{rms} is 5 Å.

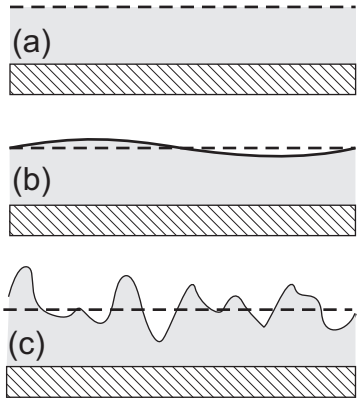

Fig. 2.8.: Schematic drawing of different configurations at interfaces: (a) Sharp transition between two interfaces. (b) Long-range waviness at the interface (c) Rough surface as a more realistic model. The dashed line corresponds to the median interface.

and (c)). The difference between the two cases is the curvature in relation to the coherence length of the incident radiation. If the curvature is much greater than the coherence length than the surface is waved. If the curvature is much smaller than the coherence length than the surface is rough.
A simple approach to deal with roughness is to select a variation in the density across an interface. This profile is then sliced in a series of layers thinner than the interface itself. The transition can be described by a Gaussian statistic:

$$G(z) = \frac{1}{(2\pi)^{1/2}\sigma} \exp\left(\frac{-z^2}{2\sigma^2}\right) \tag{2.20}$$

This leads to the Fresnel reflectivity containing the contribution of the roughness σ:

$$R(K_{z,0}) = R_F(K_{z,0}) \exp(-4k_z^2\sigma^2) \tag{2.21}$$

The reflectivity is strongly affected by the parameter σ. These lateral inhomogeneities are causing off-specular scattering.

2.3. Grazing Incidence Small Angle X-ray Scattering

Scattering techniques are important tools to analyze structures inside of bulk material [35]. The advantage is that x-rays are penetrating the sample and are non destructive. Scattering is caused by spatial electron density fluctuations. Hence buried structures on different length scales (crystal lattices, molecular distances, block-co-polymer arrangement, and so on) can be addressed by the analysis of angle regimes from 0 to 5°(small and wide angle x-ray scattering). In comparison the imaging techniques like atomic force microscopy (AFM), scanning electron microscopy (SEM) are very localized (μm^2) and are just surface sensitive. In a typical scattering experiment the sample is studied in transmission. However, for thin films the scattering volume becomes very small in transmission geometry. Therefore, grazing incidence small angle x-ray scattering ($\alpha_i <= 1°$), was developed to increase the amount of probed

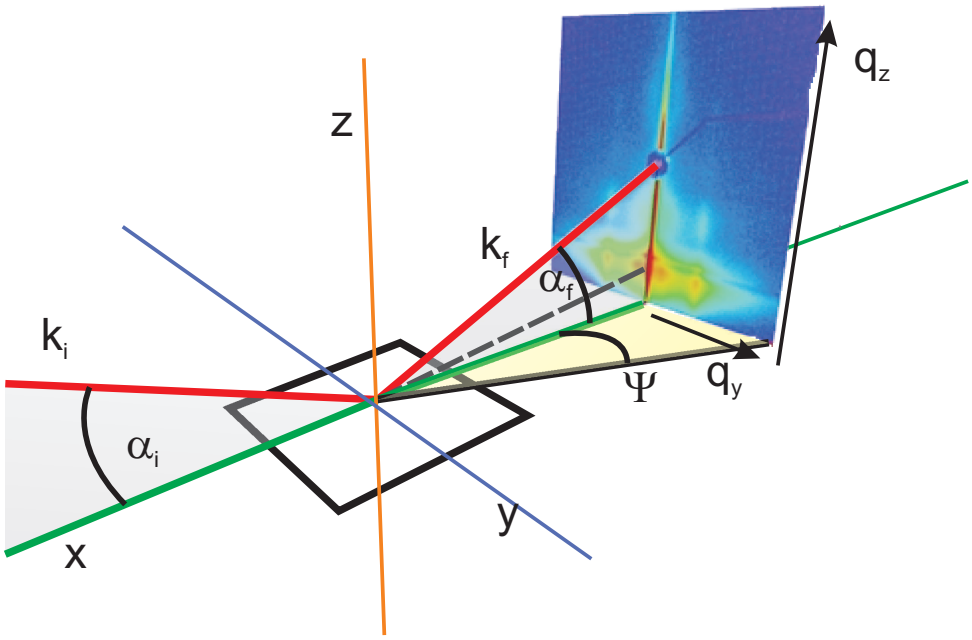

Fig. 2.9.: Scattering geometry of grazing incidence small angle x-ray scattering (GISAXS)

matter [29, 36, 37] and additionally enhance the surface sensitivity. This was first introduced by Dosch et al. [38–40]. Figure 2.9 illustrates the geometry of GISAXS and introduces the notation for the angles and wave vectors. By varying the sample to detector distance (either ∼2 m or ∼12 m) different length scale regimes can be resolved from a few nm to 100 nm in the GISAXS regime and up to μm for the GIUSAXS regime (grazing incidence Ultra small angle x-ray scattering).
The scattering vector q for x,y,z direction is defined as:

$$q_{x,y,z} = \begin{pmatrix} q_x \\ q_y \\ q_z \end{pmatrix} = \begin{pmatrix} cos(\alpha_f)cos(2\theta_f) - cos(\alpha_i) \\ cos(\alpha_f)sin(2\theta_f) \\ sin(\alpha_f) + sin(\alpha_i) \end{pmatrix} \tag{2.22}$$

And the intensity of the scattered x-ray beam is described as:

$$I(\vec{q}) = \langle |F|^2 \rangle S(q_{||}) \tag{2.23}$$

Where F is the form factor of the structure and $S(q)$ is the total interference function which explains the spatial arrangement and further lateral correla-

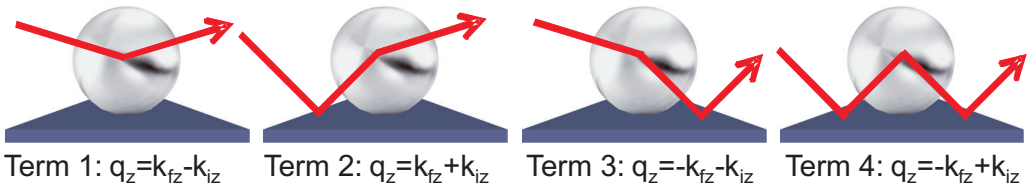

Fig. 2.10.: The four possible scattering events in the distorted Born wave approximation [36].

tion of the objects on the surface. By Fourier transformation the object position autocorrelation function is achieved. Assuming the simple Born approximation (BA), then F is the Fourier transform of the shape function of the objects defined as:

$$F(\vec{q}) = \int_V exp(i\vec{q}\vec{r})d^3r \tag{2.24}$$

However, in typical grazing incidence experiments the incidence angle α_i is close to the critical angle. Therefore, reflection-refraction effects at the surface of the substrate have to be considered. Then F has to be calculated within the distorted wave Born approximation (DWBA) and the expression gets more complex. Figure 2.10 illustrates the four possible scattering events of the x-ray beam which have to be used for a full calculation of the scattering cross section in the DWBA:

$$\frac{d\sigma}{d\Omega} \propto \big|F(\vec{q_{||}}, K_{fz} - K_{iz}) + R(\alpha_i)F(\vec{q_{||}}, K_{fz} + K_{iz}) + R(\alpha_f)F(\vec{q_{||}}, -K_{fz} - K_{iz}) + R(\alpha_i)R(\alpha_f)F(\vec{q_{||}}, -K_{fz} + K_{iz})\big|^2 \tag{2.25}$$

These waves interfere coherently giving an effective DWBA form factor F_{DWBA}. The classical form factor is transferred corresponding to the specific wave vector and the Fresnel reflection coefficient R.
Surface sensitivity is achieved when the incidence angle α_i is chosen between about half the critical angel α_c and several times the critical angle of the respective film material. A good approximation to calculate the critical angel is

as followed:

$$\alpha_c = \sqrt{2\delta} \tag{2.26}$$

δ is the real part of the refractive index. The CCD-image of a GISAXS experiment shows a typical intensity pattern (see equation 2.26): at $\alpha_f = \alpha_i$ is the specular peak, which is the direct reflected beam and at the critical angle α_c is the Yoneda peak [41, 42]. The Yoneda peak occurs when the exit angle α_f of the scattered beam is close to the critical angle α_c of the total external reflection due to a maximum in the Fresnel transmission function of the reflected beam. A characteristic bright band appears by the interference of the incoming and outgoing waves at the critical angle which is a material property. To analyze the observed scattering pattern characteristic cuts can be performed. The angular map (Ψ,α_f) is transferred into the reciprocal map (q_y,qz) (see 2D-CCD image in 2.9). The q_x-dependency can be neglected because of the the low curvature of the Ewald Sphere of $\sim 1^{-10}$ m^{-1} at typical x-ray wavelengths of $\sim$1 Å, leading to $q_x \ll q_y$ and $q_x \ll q_z$. In principal two types of cuts are meaningful: a horizontal slice at constant q_y (Out of plane scan) and a vertical slice at constant q_z (Detector scan) [29].

Out of Plane Scan

The horizontal slice contains information of the wave vector component q_y. Consequently structures parallel to the sample surface are investigated. Historically, these cuts are called "Out of plane cut" because it was measured by a point detector which was moved in the scattering plane along the y-direction. The slice is cut at the exit angle of the critical angle of the probed material because there is the materials contribution to the scattered intensity at the maximum. The detector pixels are converted to the wave vector q_y and plotted versus the intensity in a double logarithmic presentation. The detectable length scale is dependent on the geometric set-up and by the resolution. In a typical GISAXS experiment length scale from 0.1 to 100 nm are accessible.

Detector Scan

In contrast, the vertical slice contains the information of the wave vector component q_z. It is called "Detector scan" because the cut is like it would be measured by a point detector which is moved along the exit angle α_f at $\Psi = 0$. Thus, the structures perpendicular to the sample surface are probed. Typically the logarithmic intensity is plotted as a function of the incident and exit angle. From the detector scan correlation between interfaces can be identified. Partially or fully correlated roughness causes partial coherence and resonant diffuse scattering. Scattering which originates from different interfaces interferes and causes Bragg like peaks in the q_z scattering plane which fulfill the on-dimensional Bragg condition $\Delta q_z = 2\pi/d_{corr}$. This leads to the direct determination of the distance d_{corr} of the correlated interfaces [43].

2.3.1. Beamline BW4 at HASYLAB in Hamburg

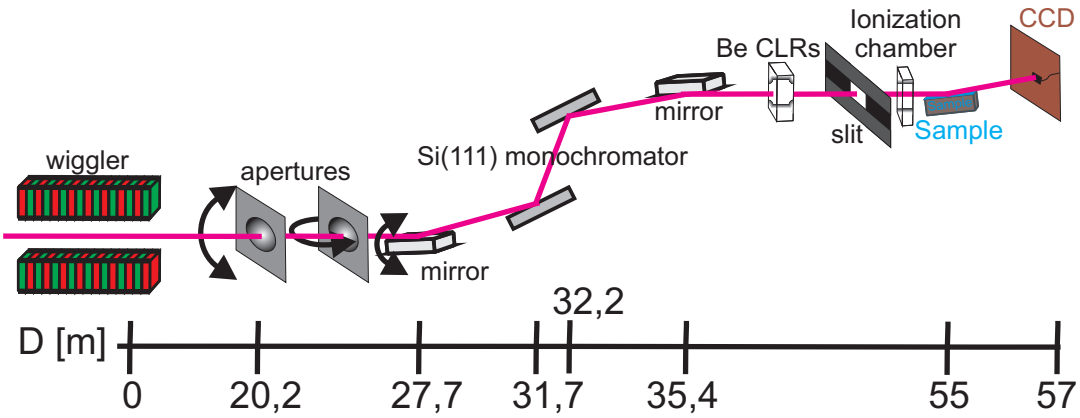

Fig. 2.11.: Layout of the Beamline BW4 at the HASYLAB Hamburg, Germany.

μ-Reflectivity and μ-GISAXS measurements were carried out at the beamline BW4 of the DORIS III storage ring at HASYLAB (DESY, Hamburg) [44]. The general layout of the beamline is shown in figure 2.11. By the monochromator the wavelength is set to 1.38 Å. An ionization chamber records the actual intensity close to the sample stage. In front of the sample an assembly of refractive beryllium lenses [45] focuses the x-ray beam down to a size of $17\times35\ \mu m^2$. The size of the beam is measured by a scan of the beam profile vertically and

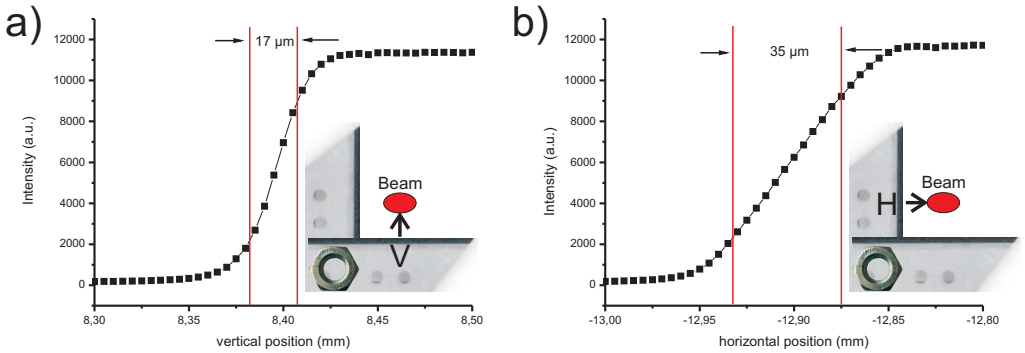

Fig. 2.12.: Knife-edge scan of the primary beam in vertical a) and horizontal b) direction. The inset shows the knife edge configuration and the scan direction. By the boundaries of the intensity at 20 % and 80 % (red lines) the beam size is calculated.

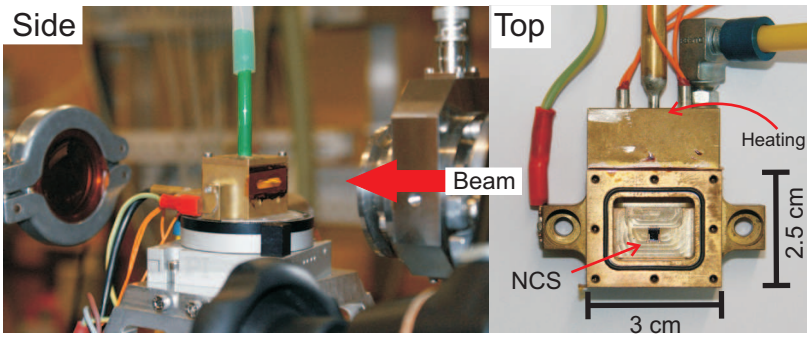

Fig. 2.13.: Side- and topview of the sample cell for NCS arrays. The side view shows the cell mounted on the goniometer stage at the beamline BW4. On top of the cell is a lid which allows to exchange the gas inside. The top view of the cell shows the NCS Position in beam direction and the connections for the heating and cooling by pressurized air. The cell is closed to the surrounding by an inlet and outlet kapton window.

horizontally. This is achieved with two crossing knife blades which are put at the sample position. The scan is performed by simply moving the blades on the beam (see inset in 2.12). The beam intensity is monitored on the primary beamstop. It results in an error function. By determination of the boundaries where the intensity is 20 % and 80 % the vertical and horizontal width is calculated (see figure 2.12).The beam divergence in and out of the plane of reflection is set by two entrance cross-slits.
The sample is placed on a two-dimensional goniometer equipped with a x/y/z-translation stage in a distance of about 1.9 to 2.2 m from the detector. For the analysis of microcantilever arrays a sample cell (see figure 2.13) was engineered to have the array mounted in beam direction and in the center of rotation. For detection a 2D-CCD (MARCCD) with 2048 x 2048 pixels (pixelsize = 79.1 μm) is used. Two different types of measurements were performed: static GISAXS and reflectivity. In the case of a static measurement the incident angle is kept at 0.7 °, if not stated else. The specular intensity is blocked by a small beamstop made of lead. In reflectivity mode the incident angle was moved from 0.15 °to 1.8 °and subsequently CCD images are taken (detailed description in section 6).

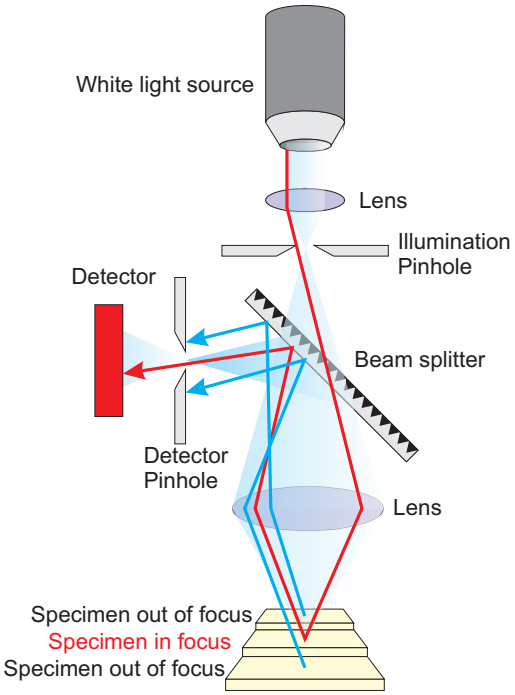

Fig. 2.14.: Basic principle of a white light confocal microscope [46]. Light is focused on the specimen. For that purpose the light emitted from the xenon white light source passes a lens, illumiation pinhole, the beam splitter, and a second lens. The reflected beam is detected after passing the detector pinhole. Only light from the surface which is in the focal plane reaches the detector (red beam). All other light is blocked by the pinhole in front of the detector (blue beams).

2.4. White Light Confocal Microscopy

White light confocal microscopy is based on the confocal microscopy which was introduced by Marvin Minsky in 1957 [47]. Confocal microscopy is an imaging technique used in the field of biology and material science to study morphology and surface topology of materials. The confocal principle increases micrograph contrast and the depth resolution up to a few nm. This offers the possibility to reconstruct a three-dimensional image of the surface. In contrast to bright field microscopy a confocal microscope allows to observe a defined spot on the specimen due to point illumination and blocking of out-of-focus information.

Figure 2.14 shows the basic principle of a confocal microscope. The specimen is illuminated by a white light source. The beam of light passes a first lens, the illumination pinhole, the beam splitter and a second focussing lens. Thus,

only the light which is reflected from the surface and is in the focal plane (have the same height) passes the pinhole in front of the detector and is detected. In such a way, a single point can be measured.
To get a full image of the field of view the surface is scanned vertically by moving the objective using a piezo motor. A μSurf© white-light confocal profilometer (Nanofocus AG, Germany) was used to image the surface topography. The light source is an external xenon lamp which illuminates the sample through the microscope. The magnification of the objective that was used is $20\times$. The corresponding maximum measurement area is 46 mm^2 and the vertical resolution is 5 nm. With this device, physical parameters of features on the surface such as length, width, radius, depth or height are measured from the surface profile.

2.5. Drop-on-Demand Inkjet Printing

The Nano-Plotter© 2.0 ("Gesellschaft fuer Silizium-Mikrosysteme mbH", Germany) is a computer-assisted drop-on-demand inkjet system [48, 49]. Essential parts of the system are the piezoelectric working micropipettes. A piezoactuator ejects the drops from the tip of the nozzle. Therefore, a high reproducibility of the drop volume is obtained and only 2% of 1000 drops deviate in the pre-set volume. Two types of commercial micropipettes are available for the use with the Nano-Plotter©: Nanotips and Picotips which differ in the dispensable drop volumes. The Nanotip ejects droplets with a volume of $\sim$ 0.4 nL while the Picotip ejects droplets with a volume of $\sim$ 0.1 nL. A maximum of 8 pipettes can be mounted at the pipetting head which is moved via step motors in x-y-z direction. The positioning resolution is about 10 μm. Controlling and operation of the Nano-Plotter© are carried out by the associated computer program NPC16 Vers. 2.14 which is a very flexible software. All functions of the inkjet system can be used either interactive or via programs written in the internal script language "Nano-Plotter-Language" which is related to Pascal. A selection of used programs are presented in the appendix B. In this way all desired even complex spot patterns can be printed. Additionally a video microscope is attached to the pipetting head. The three

used modes for printing droplets on various surfaces are explained in the following subsections.

Matrix Drop Positioning

Prior to the printing a matrix n x m can be defined. The distance between the rows and columns is individually adjustable. In this mode the pipette moves to the first position of the matrix and the desired number of droplets is ejected. The following positions are addressed sequentially by increasing the columns and rows one after the other. This is programmed with a for-loop. Thus, gradients in parameters can be introduced for each row or column e.g. the number of ejected droplets is increased by one for each row (see figure 4.36).

Continuous Drop Positioning (line)

In this case a start and an end point are defined either by absolute x/y positions or n x 2 matrix where column one is the start point and column two is the end point. Then, the pipette moves with a constant speed from the start to the end position and continuously ejects droplets with a set frequency (50-1000 Hz). Finally, a line results. Depending on the surface wettability and the parameters it is a line of merged droplets or single droplets [50] (see figures 4.45 and 4.50).

Video Assisted Drop Positioning

For complex samples like microcantilevers the video microscope is utilized to define the exact drop positions. On the live image of the sample surface the respective drop position is marked (see fig. 2.15 before). Then exactly on the marked position a drop is ejected. Afterwards a second image serves as quality control (see fig. 2.15 after).

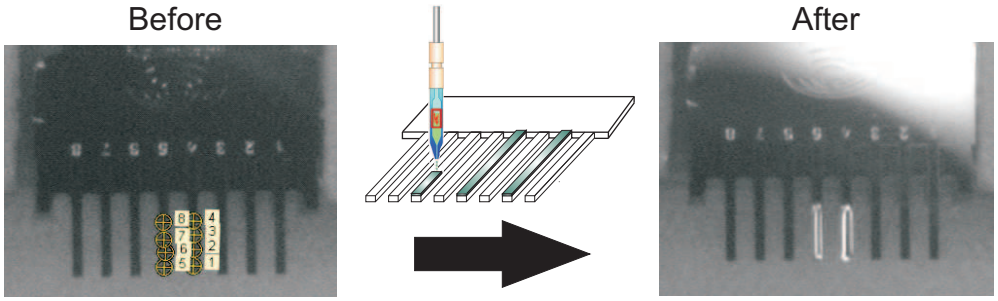

Fig. 2.15.: Contact less printing of polymer solution on microcantilever by video assisted drop positioning. In the left image the drop positions are manually marked. Then droplets are ejected at these positions. For control purposes the right image is taken afterwards. The coating covers the cantilevers completely.

2.6. Beam Deflection Read Out of Microcantilever Sensors

In this thesis microcantilever are utilized as mechanical transducers. Tiny changes in surface properties result in bending of the cantilever. The sensor array consists of 8 individual nanomechanical cantilevers having a length of 750 μm or 500 μm, a width of 90 μm, and a thickness from 1.0 to 5.0 μm (Octosensis, Micromotive GmbH, Mainz, Germany). The general beam deflection principle is applied to read out the nanomechanical deflection of a microcantilever sensor [51]. The principle is equal to the one used in every scanning probe microscope (SPM). The sample configuration can be seen in figure 2.16. A commercial device Scentris™ (Veeco, Santa Barbara, USA) is used. A light source consisting of eight superluminous diodes emits a collimated light beam which is adjusted by a mirror on the free end of the cantilever. The reflected beam is directed by a second mirror on a position sensitive detector (PSD).

An array is mounted in a steel cell which is closed by a glass window and is equipped with an inlet and outlet for exchanging the environment either with liquid or gas. Additionally a resistive foil heater (28x28 mm, 75 Ω, Minco, USA) is glued underneath the cell for temperature control. The temperature is recorded by a PT100 which is located close to the cantilever array. In order to avoid heating of the electronics situated below the fluidic cell a thermal insulation made from PEEK was placed between the fluidic cell and the elec-

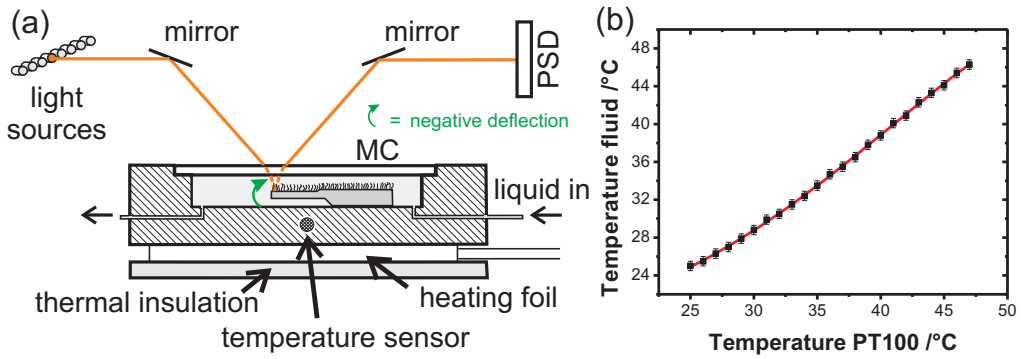

Fig. 2.16.: (a) Setup for the read out of nanomechanical cantilever sensors by beam deflection. (b) Temperature calibration curve.

tronic housing. Temperature ramps for heating can be driven by the home-made temperature controller. The heating rate is varied from 0.1°C to 10°C per minute. Prior to the measurements the temperature control was calibrated in a temperature range of 20 - 60°C (see figure 2.16 (b)). So the temperature was measured in the fluid at the cantilever position with a second PT100. All measurements were adjusted according to the calibration. For cooling the electronics is switched off and the heat dissipates in the surrounding environment. Therefore, the cooling rate is not linear and after an appropriate time interval the setup was at room temperature again (30 min to cool down from 50°C to room temperature).

Static Mode

In a static mode experiment the bending of a NCS is monitored on the PSD. The obtained deflection data is recorded as function of the time, temperature or humidity.

Dynamic Mode

The beam deflection principle is also able to determine the resonance frequency of the cantilever. This can be done by analyzing the thermal vibration or by external actuation with a piezo stage. The resonance frequency is a characteristic value for the material (E-modulus) and cantilever properties (length, width, thickness, mass). If an additional mass is loaded on a can-

tilever, then the frequency shifts to lower values. Therefore, the extra mass Δm can be detected very precisely in a pg range.

$$\Delta m = \frac{K}{4\pi^2 \cdot n}\left(\frac{1}{f_2^2} - \frac{1}{f_1^2}\right) \tag{2.27}$$

When the initial resonance frequency f_1 and the spring constant K is known, then the mass change Δm is calculated from frequency f_2 which is the resonance frequency of the cantilever plus the additional mass. Herein n is an effective function due to the shape of cantilever (n = 0.2427 for rectangular cantilevers and 1st resonance frequency; n = 0.006179 for rectangular cantilevers and 2nd resonance frequency).

2.7. Further Instruments

2.7.1. White Light Microscope

A light microscope is used to get magnified optical images using optical elements like lenses. In this work a conventional Zeiss light microscope equipped with a 10× objective was used to take pictures of the fabricated PEM patterns.

2.7.2. Atomic Force Microscope

The atomic force microscope (AFM) or scanning probe microscope (SPM) is used to scan the surface topography with a small tip either in contact or intermitted mode (or tapping mode). Obtained images are in the real space and can be analyzed for surface roughness, height profiles and dimensions of objects. The resolution is in the nanometer range. In this work two different instruments are used: (a) A Dimension 3100 atomic force microscope was used to study the surface roughness, bilayer thickness, etc. in smaller scales. (b) A Nanowizard© (JPK Instruments AG, Germany) atomic force microscope was used in intermittent contact mode to probe individual microlenses.

2.7.3. Contact Angle Measurement

The contact angle measurements were performed on the substrates using a Krüss, DSA10-MK2. The static contact angle was measured in air atmosphere at room temperature with Millipore water as solution.

2.7.4. Gel Permeation Chromatography

Gel permeation chromatography (GPC) is used to determine the molecular weight and polydispersity index of the synthesized polymers. It is a chromatographic technique which fractionates the polymer by diffusion into pores of different size depending on the molecular weight. A prior calibration is needed to calculate the molecular weight and is performed routinely. For this thesis the following devices are used: PSS (SDV) PS column, Waters 590 pump and RI ERMA Inc. ERC 7512 ERC Detector. The eluent was DMF in the case of PNIPAM and THF in the case of PMMA. The flow rate was set to 1 mL/min.

2.7.5. Nuclear Magnetic Resonance Spectroscopy

^{1}H nuclear magnetic resonance spectroscopy (NMR) is used to analyze the molecular structure of the synthesized materials. For the measurements a Bruker Avance DPX 250 was utilized having a resonance frequency of 250 MHz.

3. PMMA Brush Synthesis in an Ionic Liquid

*

In this chapter, the synthesis of poly(methyl methacrylate) (PMMA) brushes in the room temperature ionic liquid 1-butyl-3-methylimidazolium hexafluorophosphate ([Bmim][PF_6]) is demonstrated. The brushes were prepared on functionalized silicon by atom transfer radical polymerization (ATRP). Kinetic study of the ATRP process identified linear and dense brush growth up to thicknesses of 8.3 nm. Thickness measurements were performed by ellipsometry (see section 2.1) and x-ray reflectivity (see section 2.2).
[Bmim][PF_6] is a non-volatile solvent. This advantage was used to prepare polymer brush coatings in the confined geometry of a "micro" droplet. The living character of the ATRP synthesis supported this method because sequential addition of MMA to the micro droplet increased the brush thickness. Imaging ellipsometry is used to monitor the thickness and structure of the formed polymer layer.
Generally, ionic liquids (IL) are intensively under investigation because of their unique behavior as solvents. Due to their ionic nature their vapor pressure is negligible and their thermal stability is much higher compared to common organic solvents. Combined with their possibility to solvate many organic, inorganic and organometallic substances, turns IL's into substitutes for volatile and hazardous solvents in organic synthesis. Therefore, the use of IL's is a step towards "green chemistry" as discussed in various review articles [52–55].

*This section is based on the following publication: **Nett, S. K.**, Kircher, G., und Gutmann, J. S., *Macromolecular Chemistry and Physics* **2009**, *submitted*, PMMA Brushes Prepared in an Ionic Liquid.

Alternatively, shifting reactions to small volumes in the range of micro to nanoliter is another field where IL's may replace more conventional solvents. Kinetic and diffusion processes are crucial for reactions and thus a minimum of time is required to get a certain conversion. IL's reveal the great opportunity to meet this condition and therefore can be used as microreactors for analytics applications such as batch analysis of many drops, biochemistry and modification of planar surfaces at the micrometer scale.
In sub microliter volumes, liquids tend to evaporate faster, since their vapor pressure depends on the curvature of the liquid gas interface. Kelvin's equation (see eq. 3.2) for a sphere-like volume of radius r describes this situation [11]. Typical volumes for ink jet printing are 1 to 1000 pL. Even liquids with boiling points up to 200°C (corresponding vapor pressure $< 10^{-1}$ mmHg) are evaporating in around 1 min [56]. The ultimate aim of these studies is inkjet printing reaction solutions for polymer synthesis. The specific purpose addressed here is the functionalization of microcantilevers with polymer brushes for sensing application [57]. The aim is to establish a process which is easy and reproducible. Controlled radical polymerization processes proofed to be a versatile method to prepare polymer brushes.
IL's have been used for different polymerization [52, 58, 59] methods like radical [60], ATRP [61], ROMP, RAFT [62], cationic polymerization. Especially for radical polymerization IL's as reaction media exhibit significant increase in the rate of propagation k_p when the content of [Bmim][PF_6] increases [63], whereas at the same time the rate of termination is decreased. In the literature the synthesis of Poly(methyl methacrylate) (PMMA) in IL's was reported here [61, 64, 65]. So far, IL's have not been used as reaction media for the surface initiated polymerization of PMMA brushes. In this thesis the synthesis of PMMA brushes on silicon surfaces functionalized by an ATRP starter is demonstrated. In detail the kinetics of the polymer brush is investigated. Furthermore this chapter shows that [Bmim][PF_6] can be used as a microreactor for polymer brush synthesis.

Table 3.1.: Static contactangle of water and thickness for different substrates. The thickness was determined by ellipsometry. For the model based thickness calculation from the ellipsometric angles the here stated value for the starter layer was used.

Substrate	Contactangle / °	Thickness /nm
Clean Silicon	∼0 °	1.6 nm
Starter layer	77.2 °	1.6 nm
PMMA No.7	66.7 °	6.5 nm
PMMA No.6	62.6 °	7.5 nm

3.1. Anchoring of the Starter Layer

The ATRP starter was attached to the surface via a chlorosilane forming a self assembled monolayer. This changed the surface energy and the thickness compared to clean silicon. Successful monolayer formation was monitored by two complementary physical methods, contact angle measurements and ellipsometry. For calculating the thickness a box model was applied (for details see section 2.1 and fig. 2.4). Because of the small difference in refractive indices between silicon oxide (n = 1.4603) and a silane (n = 1.46) these layers are simplified to one layer which has an average thickness of 2.1 nm. As shown in table 3.1 the contact angle changes from 0°to 77.2°.

3.2. Catalytic System for ATRP in [Bmim][PF_6]

The basic element of the ATRP synthesis is the catalytic system which defines the equilibrium between activation and deactivation of the dormant radical. For a given monomer and solvent the catalyst has to be adapted. In the literature [64] the synthesis of poly(methyl methacrylate) is reported using CuBr / PMDETA. Biederon et.al. obtained molecular weights of around 2700 g/mol. CuBr / PMDETA is the established catalyst to perform controlled polymerization of PMMA in conventional solvents (e.g. Anisol). Using this system in [BMIM] [PF6] resulted in a very fast reaction indicated by a gelation in less than 15 minutes. For the reaction a monomer to starter ratio was calculated to result in a molecular weight of 10000 g/mol, however the actual values obtained are M_w = 36804 g/mol and D = 1.46. This implies an uncontrolled polymerization which necessitates an improvement of the catalytic system.

Different catalytic systems were investigated in order to obtain a slower reaction rate for a better control of the molecular weight. Table 3.2 gives an overview of the used catalysts. Exchanging the halogen from bromine to chlorine (III and IV) or different ligands (IV and V) did not give the intended enhancement. The addition of $CuBr_2$ in a ratio of 8.6 to 1 for CuBr resulted in a controlled reaction. Cu(II) acts as the deactivator [66–68] in the mechanism of ATRP. Therefore the addition of $CuBr_2$ slowed the reaction. The molecular weight and distribution of M_w = 14780 g/mol and D = 1.12 are in agreement with a controlled ATRP synthesis.

3.3. Kinetic Studies of PMMA Brush Formation

With catalytic system VIII (table 3.2) the kinetics of the polymer brush growth was further investigated. The reaction bath was prepared as described in the experimental section 7.5 with a target molecular weight of 20000 g/mol at room temperature and afterwards transferred to a glove box. In the glove box it is possible to take out silicon pieces of the solution without introduction of oxygen into the system which oxidizes the active catalyst and stops the reaction. After a certain time period a piece of silicon and in parallel a small volume of the reaction solution were taken from the reaction bath.
Sacrificial initiator is added to increase the concentration of catalyst in the reaction bath and to get free polymer which was analyzed by GPC and NMR. Detailed studies showed that the molecular weight of the free polymer chains in solution and the tethered polymer chains are similar [69–72]. All NMR spectra showed the typical peak structure for PMMA. The brush thickness was determined by ellipsometry and x-ray reflectivity. From the measured data the thickness was calculated with the corresponding models described in the methods section 2.1. Figure 3.17 compares the values for the samples taken out after different times.
Comparing the values determined by x-ray measurements, there is a systematic deviation of about 1 nm. This is due to the fact that for the calculation of the ellipsometric thickness the refractive index of the bulk material of 1.49 was

Table 3.2.: Overview of the tested catalytic systems. Adding $CuBr_2$ to the reaction mixture decreased the speed of the reaction significantly. The time for gelation is the point when the liquid was so viscous that stirring was not longer possible. Molecular weight and molecular weight distribution were analyzed by size exclusion chromatography. BrPEthE: Brompropionateethylester. For the other abbreviations refer to the experimental part 7.5.

No	Metal salt	Ligand	Starter	Gelation /min	M_n /g/mol	D	d /nm	t_{ges} /min
I	CuBr	PMDETA	2-EiBBr	15	36804	1.46	9.2	60
II	CuBr	PMDETA	BrPEthE	15	31493	1.34	-	45
III	CuCl	PMDETA	ECP	10	24807	2	-	20
IV	CuCl	Me_6TREN	ECP	20	39979	1.93	-	30
V	CuBr	BiPy	2-EiBBr	45 viskos	13788	1.16	-	45
VI	CuBr/ $CuBr_2$	PMDETA	2-EiBBr	180	12776	1.14	-	240
VII	CuBr/ $CuBr_2$	PMDETA	2-EiBBr	150	14780	1.12	-	21h
VIII	CuBr/ $CuBr_2$	PMDETA	2-EiBBr	150	13875	1.13	4.3	21h

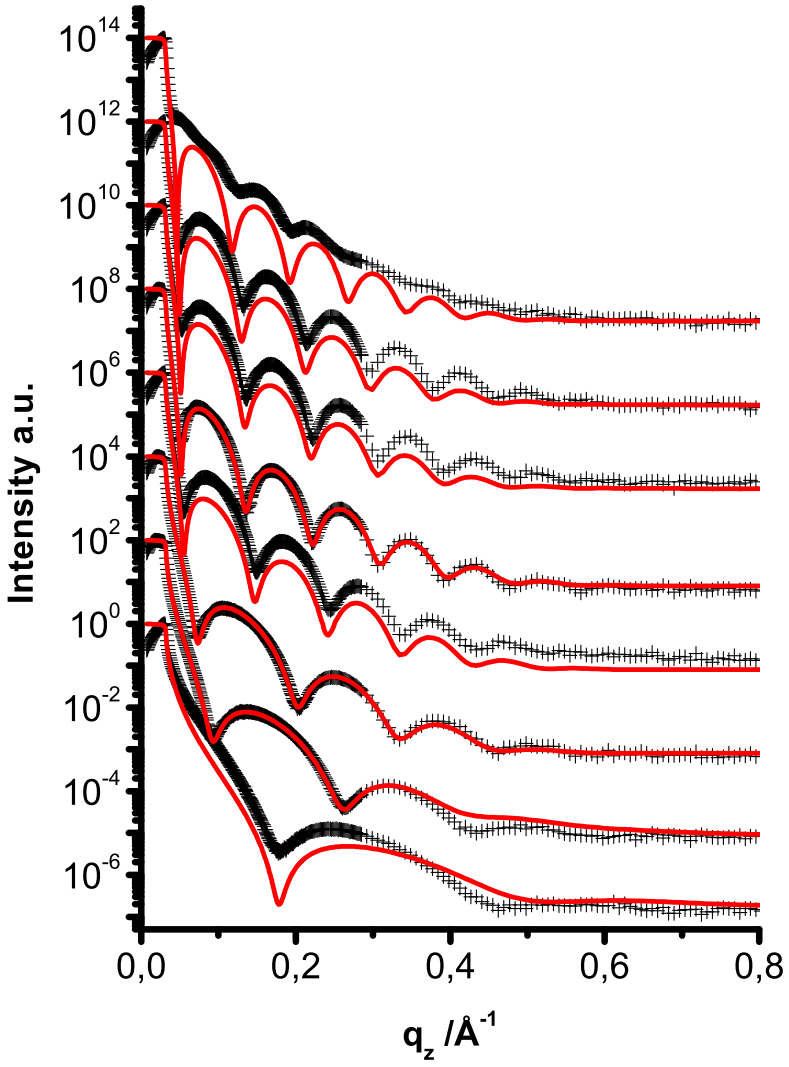

Fig. 3.17.: X-Ray reflectivity curves for the PMMA brush coated wafers, from bottom to top: taken after 65, 120, 180, 300, 420, 545, 825, 1485 min of reaction time (black crosses) with the corresponding fits (red line). All graphs are shifted by a factor of 100 for clarity.

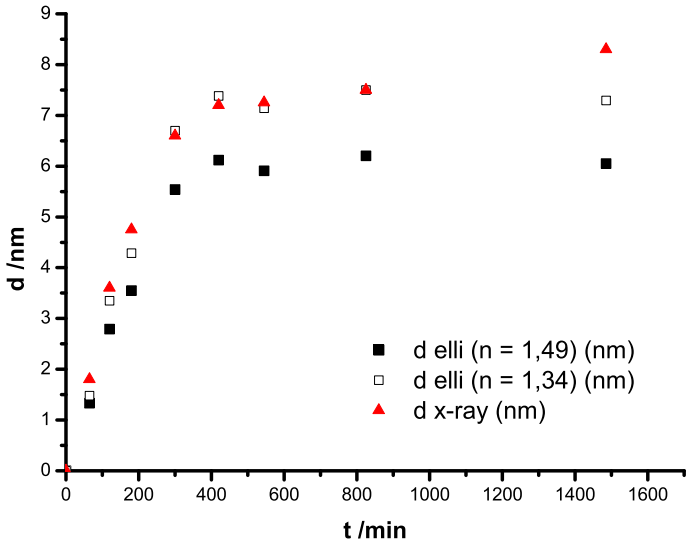

Fig. 3.18.: Comparison of data measured by ellipsometry and x-ray reflectivity; the thickness obtained from x-ray reflectivity is slightly higher than ellipsometry.

used. Thicknesses extracted from the Kiessig fringes in the plot of the x-ray reflectivity data are much more accurate. Therefore modeling the refractive index for the ellipsometric data with the x-ray thickness gives a lower index of 1.34. The new modeled thicknesses deviate now less than 0.3 nm. In the following graphs the corrected ellipsometric thicknesses are used unless otherwise noted.

X-Ray reflectivity measurements contain also the information of the film roughness. Polymer brushes are typically smooth that means the roughness is less or similar than the substrate roughness. In the case for the prepared samples the roughness for the film is in average 3.3 Å and for the substrate 4.2 Å.

Contact angles for two representative PMMA samples shown in table 3.1 differ from the value measured for the starter layer. However, contact angles for initiator and PMMA brushes from the literature [73] are in the same range.

The ellipsometric thickness and the molecular weight are plotted vs. time in the figure 3.19. With time the molecular weight and the thickness is increasing. After 545 min the growth is leveling off. The maximum thickness of 6.5

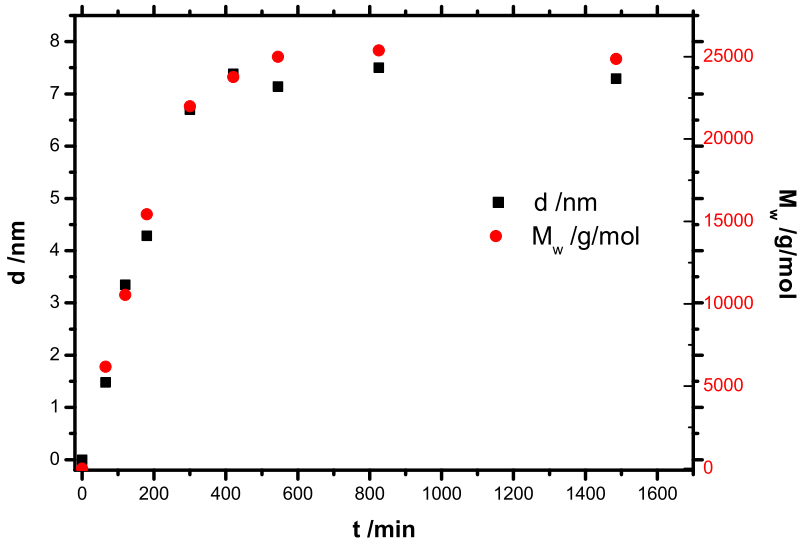

Fig. 3.19.: Thickness d (left y-axis) and the molecular weight M_w (right y-axis) as a function of reaction time. The values for the thickness were measured by ellipsometry and calculated with a refractive index of 1.34 for the PMMA layer.

nm and the corresponding molecular weight M_n = 21554 g/mol fit to typical literature values [74] of PMMA brushes prepared in conventional solvents. Using equation 3.1 the grafting density was calculated. At all times the grafting density is almost equal to the average 0.36 $\Gamma/\mu mol/m^2$ (see fig 3.20). This implies a growth of dense polymer brushes and in consequence the increase in brush thickness should scale linear with molecular weight [75,76].

$$\Gamma = \frac{N_A d \rho}{M_w} \tag{3.1}$$

To show the linear growth of the polymer brush the thickness measured by ellipsometry is plotted as a function of the molecular weight M_w (Figure 3.21). From the linear fit the growth rate is determined as 4590 g/mol per nm.

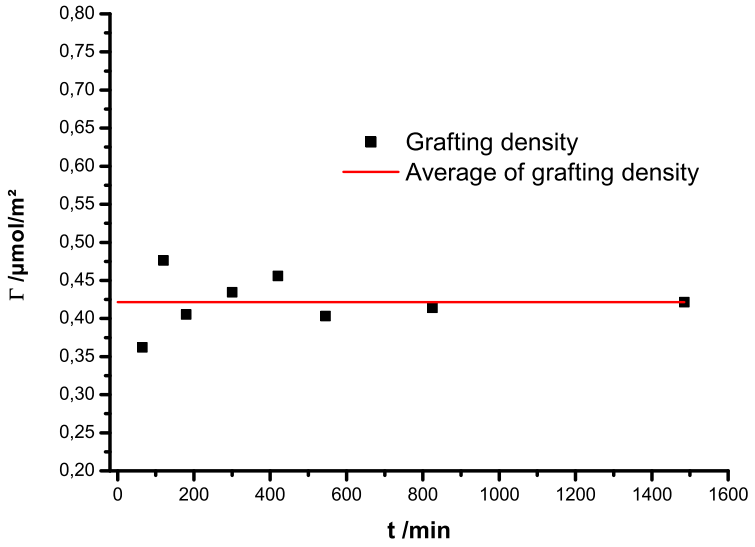

Fig. 3.20.: Calculated grafting density as function of reaction time. Equation 3.1 was used to calculate the grafting density. The red line is the average of the grafting density.

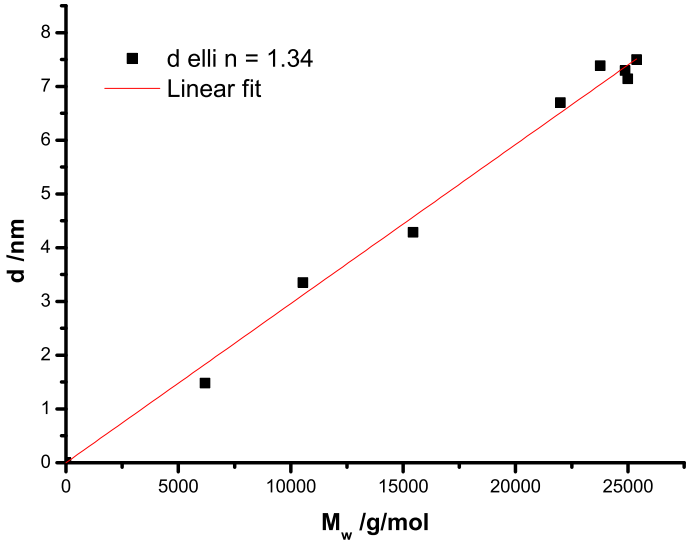

Fig. 3.21.: Molecular weight dependence of the brush layer thickness. The values for the thickness was measured by ellipsometry and for the model calculation the corrected refractive index of n = 1.34 was used. The solid line shows a linear fit.

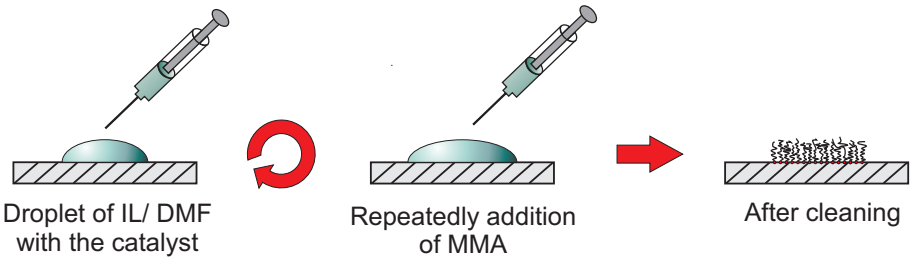

Fig. 3.22.: Process of applying droplets to the substrate for pattering with polymer brushes.

3.4. [Bmim][PF_6] Droplets as Microreactors

As a proof of principle droplets of the room temperature ionic liquid [Bmim][PF_6] were used. The drops act as microreactors to facilitate the formation of polymer brushes in a confined geometry. First the solution of the catalyst consisting of CuBr and PMDETA in a mixture of IL and DMF is prepared. DMF is added to reduce the viscosity and facilitates the placement of a droplet on the substrate surface. In scheme 3.22 the procedure is illustrated. Via an Eppendorf pipette a 2 μL catalyst/IL/DMF drop is put onto a functionalized silicon wafer. After a period of 15 min 1 μL MMA is given to the IL drop. After thorough cleaning the surface was analyzed using an imaging ellipsometer. In the area were the droplet covered the substrate a polymer brush layer was formed. The diameter of this area is around 4 mm and a layer thickness of about 5 nm was found. Figure 3.23 left shows a height map of the edge of the brush region. Furthermore 1 μL MMA was given to the droplet after approximately 20 min. After 3 times adding MMA the brush thickness went up to 13 nm in average illustrated by figure 3.23 right. The result shows that the concept of using a non volatile droplet as a reactor for performing reactions is working. In this case the limitation is given by the evaporation time of the monomer MMA which is between 90 to 120 s for the described system. However, the living character of the controlled radical polymerization gives the possibility to reinitiate the reaction and the brush thickness increases when monomer is added again to the [Bmim][PF_6] droplet.
of the

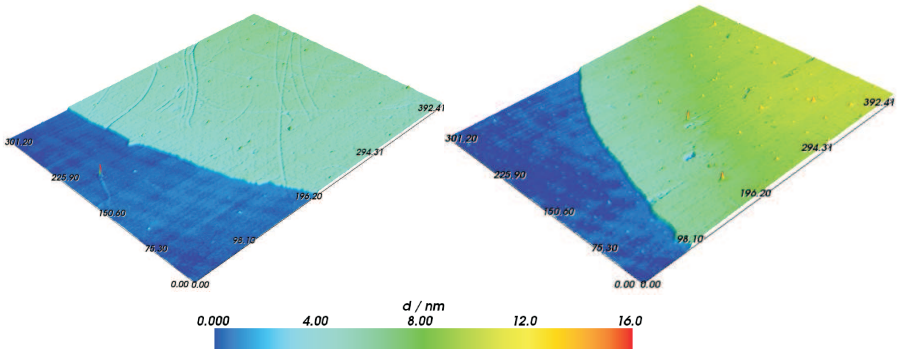

Fig. 3.23.: The images show a height map measured with imaging ellipsometry. Left: edge of the polymer brush covered region. Right: edge of the polymer brush covered region after 2 times addition of MMA to the micro droplet. The x-y dimension is 400 x 300 μm^2.

3.5. Evaporation of Solvent Mixtures from a [Bmim][PF_6] Drop

Obviously the limitation of the brush growth is the evaporation of the monomer methyl methacrylate (MMA). A pure 1 μL droplet of MMA evaporates within seconds. The next chapter addresses this problem by explaining the theory of droplet evaporation and showing experiments on evaporation of solvent mixtures namely dimethylformamide and methyl methacrylate from an ionic liquid drop to clarify the timescale and rate of evaporation.

3.5.1. Theory of the Evaporation of Sessile Drops

The evaporation process of liquid sessile droplets is fundamental in nature. Due to the curvature of the drop the vapor pressure is higher than that of a flat, planar film [11]. This is caused by the Laplace pressure and can be quantitatively described by the Kelvin equation:

$$RT \ln \frac{P_0^K}{P_0} = \nu V_m \left(\frac{1}{R_1} + \frac{1}{R_2} \right) \tag{3.2}$$

P_0 is the vapor pressure of a flat liquid film and P_0^K of the corresponding curved liquid drop. V_m is the molar volume, R_1 and R_2 describe the radius of

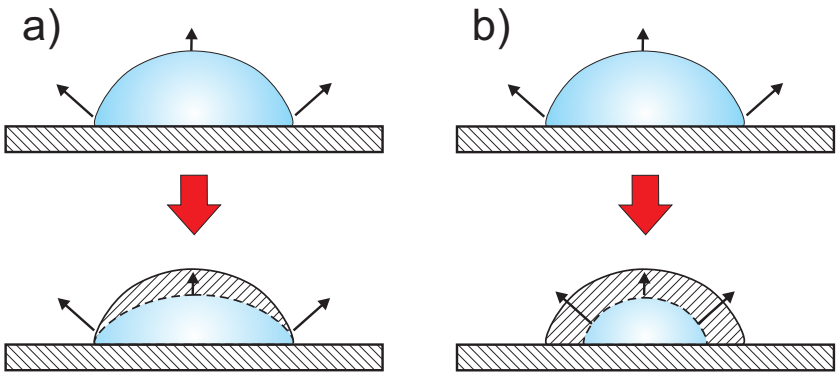

Fig. 3.24.: The figure illustrates the two cases of evaporation modes. a) During evaporation the contact radius stays constant: Constant contact radius b) During evaporation the contact angle stays constant: Constant contact angle

the droplet. Therefore, curved liquid surfaces like drops will evaporate most likely. Basically, two modes of evaporation are identified [77], first evaporation with constant contact radius (CCR) and second evaporation with constant contact angle (CCA). In the constant contact radius mode the rim of the drop is pinned while the contact area stays constant the contact angle decreases with time (illustrated in fig. 3.24 a)). In opposite, it is characteristic for the constant contact angle mode that the contact area shrinks while the contact angle stays constant (illustrated in fig. 3.24 b)). All evaporation processes can be assigned to either one of the modes (CCR or CCA) described above or to a combination of both (CCR and CCA). In principle two processes are involved in the phase transition from the liquid to the vapor state. The liquid molecules have to diffuse from the drop surface to the surrounding air. Furthermore the molecules flow from the inside of the drop to the liquid-air interface [78]. An evaporation law is derived for the constant contact angle mode [77,79]. The volume $V^{2/3}$ decreases linearly with time. For the constant contact radius mode an evaporation law can not be formulated in a closed form. However, a linear approximation is suitable for contact angles smaller than 90° [80]. This means that the volume almost decreases linearly with time.

3.5.2. Details of the Evaporation Experiment

To observe the evaporation behavior of sessile droplets a volume of about 0.5 μL was deposited on an hydrophobized silicon substrate. Prior to deposition the liquid mixtures were prepared by weighing the components dimethylformamide (DMF), [Bmim][PF_6], and methyl methacrylate (MMA) to get ratios by volume. Deposition was realized by an automated syringe injection pump. After placing the drop the evaporation is recorded with a camera system consisting of a 2x objective (Mitutoyo Corp., Kawasaki, Japan), a zoom tube (Precise Eye, Navitar Inc., New York), and a digital camera (Basler Vision Technology, Ahrensburg, Germany). The substrate is illuminated from the back with a white light from a cold light source (KL 2500 LCD, Schott, Mainz, Germany) through a diffuser. With the camera a series of images is recorded. A single frame has a resolution of 640 x 480 pixels. In advance the system was calibrated using a micrometer scale to get the μm/pixel ratio. Assuming an axi-symmetric shape of the drop from the profiles the contact radius a and the height h is calculated. The spherical shape of a droplet on a solid surface can be assumed because the contact radius is smaller than its capillary length. Based on this the contact angle Θ (Eq. 3.3) and the volume V (Eq. 3.4) can be calculated, where h is the height, r is the radius:

$$\Theta = arctan(\frac{h}{r}) \tag{3.3}$$

$$V = \frac{\pi h(3r^2 + h^2)}{6} \tag{3.4}$$

3.6. Results on the Evaporation Experiments

To understand the evaporation behavior of liquid mixtures it is needed to see how the single components pure DMF and MMA evaporate. Thereafter the evaporation of the mixtures DMF/MMA, [Bmim][PF_6]/DMF, [Bmim][PF_6]/MMA and [Bmim][PF_6]/DMF/MMA is discussed. For every experiment the characteristic curves are summarized in one figure which is organized as following: First the drop volume is plotted against the time (a). The next graph shows

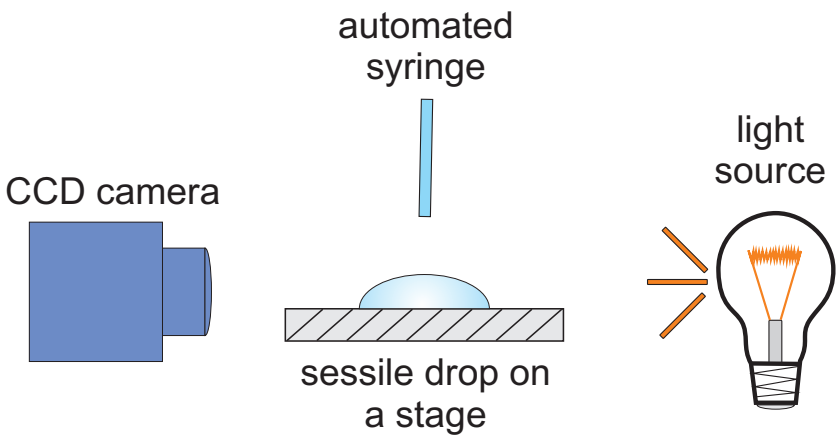

Fig. 3.25.: Setup for the observation of the sessile droplets. Via an automated syringe a droplet around 0.5 μL is deposited on a silicon substrate. A CCD camera monitors the evaporation. In order to get a good contrast the drop is illuminated from the back.

the normalized volume V and $V^{2/3}$ (b). If possible a linear fit is applied. Detailed inside in the evaporation mechanism gives the graph contact angle and radius varying with time (c). At the end the evaporation rate is calculated (d). Generally, these curves needed to be smoothed.

3.6.1. Evaporation of Pure DMF Drops

A DMF drop of a volume of 92 nL (exp. 5) and of 96 nL (exp. 2) evaporates within 900 s (see fig. 3.26). Initially the drop is pinned. However, after 150 - 200 s the contact radius starts to decrease. This means that the evaporation mode switches from constant contact radius to constant contact angle. Therefore, after depinning the evaporation law is close to $V^{2/3} = V_0^{2/3} - A_0 t$. A fit is applied to the volume vs. time curve to get the exponent a for the function 3.5:

$$V = \left(V_0^{1/a} - A_0 t\right)^a \tag{3.5}$$

$$A_0 = \frac{4}{3}\pi \left(\frac{3}{\pi}\right)^{1/3} \frac{DP_0 Mf}{RT\rho\beta^{1/3}} \tag{3.6}$$

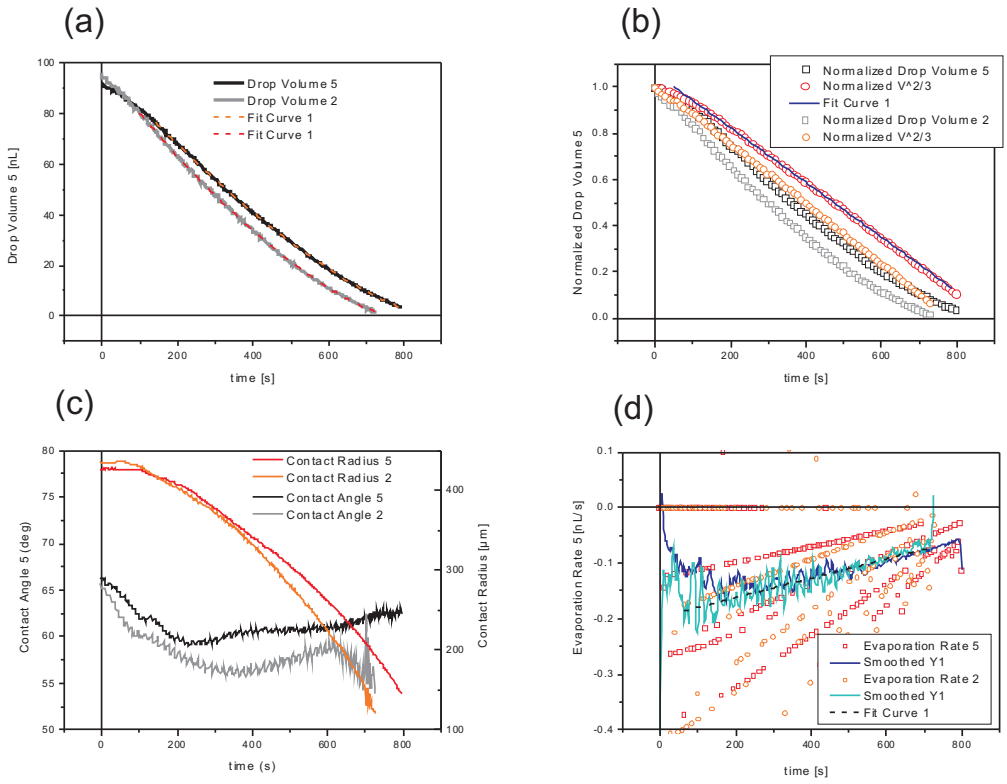

Fig. 3.26.: Results for the evaporation of pure DMF droplets. (a) A droplet of 92 nL or 96 nL takes about 900 s for complete evaporation. (b) Plot of the normalized volume V and $V^{2/3}$. The linear decrease of $V^{2/3}$ with time denotes for evaporation with constant contact angle. (c) After initial pinning the contact radius starts to decrease at 150 - 200 s. Accordingly the contact angle decreases about 5 °and then stays more or less constant for the rest of the evaporation time. (d) The evaporation rate decreases slightly and is in average over time 0.19 nL/s.

Wherein, V_0 is the initial drop volume, D stands for the diffusion coefficient of vapor molecules in the surrounding atmosphere, M is the molar mass, R is the gas constant, T is the temperature, ρ is the liquid density, P_0 is the vapor pressure and β and f are functions of the contact angle Θ, with $\beta = (1 - \cos\Theta)^2(2 + \cos\Theta)$ and $f = 0.00008957 + 0.6333\Theta + 0.116\Theta^2 - 0.08878\Theta^3 + 0.01033\Theta^4$ (Θ is the dimensionless contact angle in radians.). As a result of the fit $a_{(5)}$ = 1.482 and $a_{(2)}$ = 1.448 is obtained which is just marginally different compared to a = 1.5 from theory. Second the fit yields A_0 = 2.38x10^{-10}. Calculation of A_0 by using the material parameters listed in appendix C.1 and estimating the diffusion coefficient of DMF in air to be 6x10^{-6} m^2/s gives a result of A_0 = 2.21x10^{-10}. This is evidence of the good estimation of the diffusion coefficient and in general agreement with the theory. The evaporation rate increases in the beginning until ∼150 s to a rate of around 0.18 nL/s and finally decreases continuously until the evaporation end.

3.6.2. Evaporation of Pure MMA Drops

The evaporation of a MMA drop is much faster compared to pure DMF (see fig. 3.27). A MMA drop of a volume V = 329 nL is evaporated within t = ∼100 s. In this case the evaporation law for constant contact angle $V^{2/3} = V_0^{2/3} - A_0 t$ can be applied. The normalized volume $V^{2/3}$ decreases linear. Again, a fit is applied to the volume vs. time curve to get the exponent a for the function eq. 3.5, which yields in a value of a = 1.641 and A_0 = 3.59×10^{-9}. Once more a is close to the theoretical value of 1.5. In order to calculate A_0 the material parameters (see appendix C.1) and the estimated diffusion coefficient D = 4.3×10^{-6} are used. This is in line with the calculated result of A_0 = 3.51×10^{-6}. The evaporation rate is in the beginning around 4 nL/s and then linearly decreases until the end. Just before the end the rate is still high around 1.5 nL/s.

In conclusion both pure liquids evaporate according to the theory for constant contact angle. Although, DMF shows in the beginning phase the phenomenon of pinning. As expected MMA evaporates about 20 times quicker than DMF.

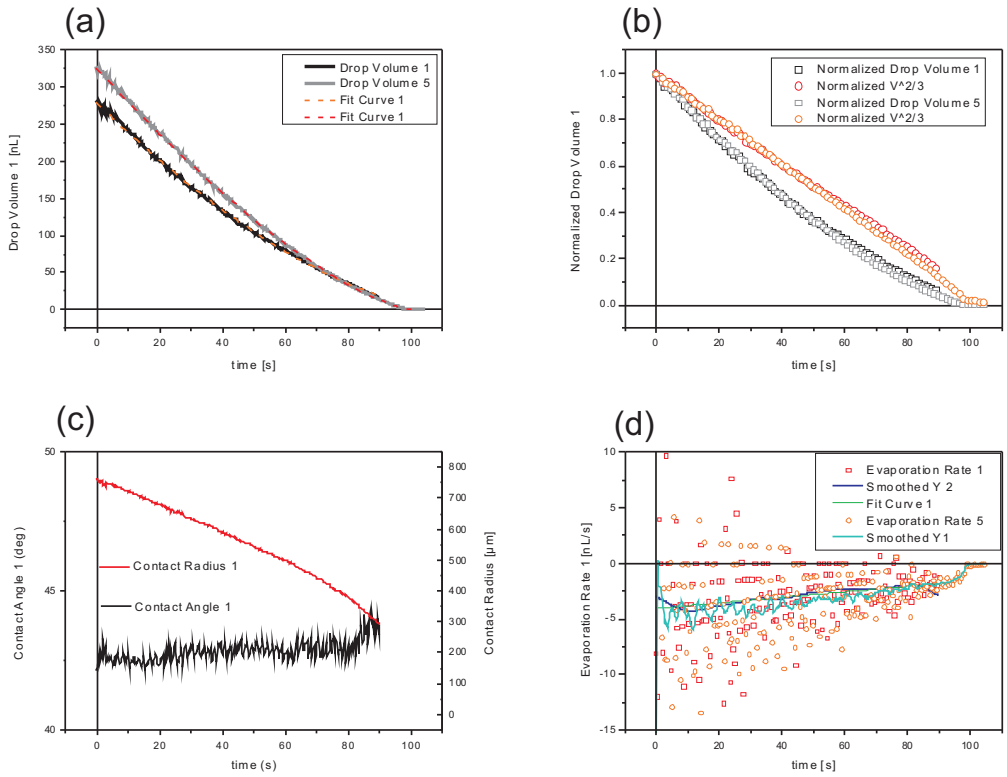

Fig. 3.27.: Results for the evaporation of pure MMA droplets. (a) A droplet of 392 nL or 282 nL takes about 110 s and 100 s for complete evaporation. (b) Plot of the normalized volume V and $V^{2/3}$. The linear decrease of $V^{2/3}$ with time denotes for evaporation with constant contact angle. (c) The contact radius decreases constantly with time. Accordingly the contact angle stays constant at 43 °(d) The evaporation rate of 4 nL/s linearly decreases until the end and is just before the end still at 1.5 nL/s.

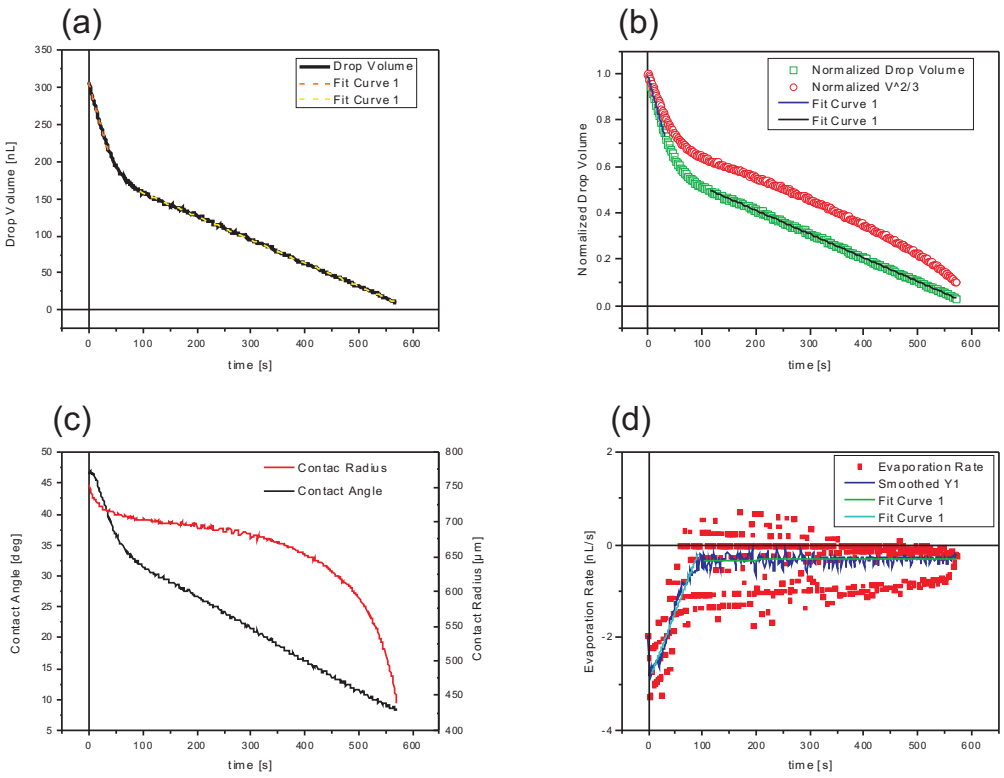

Fig. 3.28.: Results for the evaporation of DMF/MMA 1:1 mixture droplets. (a) There are two stages of evaporation present: first MMA evaporates, which takes about $t_1 = 95$ s and then DMF evaporates within $t_1 = 600$ s. (b) Plot of the normalized volume V and $V^{2/3}$. Both stages of evaporation are of the type that volume V decreases linearly with time. (c) The contact radius and the contact angle decrease constantly with time. Over the whole evaporation time no pinning is observed. (d) The evaporation rate starts at 3 nL/s and linearly decreases until $t = 100$ s, and than stays constant at about 0.32 nL/s.

3.6.3. Evaporation of DMF/MMA Mixture Drops

The result of the mixture DMF/MMA 1:1 is discussed here (see figure 3.28). The volume vs. time curve shows two stages of evaporation. First MMA evaporates quickly within $t_1 = \sim 95$ s from a drop with a starting volume V_0 of 310 nL. Subsequently DMF evaporates within $t_1 = \sim 600$ s. Remarkably both stages follow the evaporation law $V = V_0 - A_0 t$. However, the pure liquids showed linear behavior for $V^{2/3}$. While evaporation of the mixture both the contact angle and contact radius are decreasing all times. There is

no pinning for the whole process observed. In opposition to the pure liquid the contact angle of this mixture decreases significantly from ∼48 °to ∼10 °. The evaporation rate starts at 3 nL/s and linearly decreases until t ∼ 100 s and then remains constant at 0.32 nL/s until the end of evaporation. So the evaporation rate for MMA in the mixture is smaller than that of pure MMA, while DMF in the mixture shows a higher rate than the pure component until the end. This is maybe caused by remaining MMA in the droplet until the end of the evaporation.

3.6.4. Evaporation of [Bmim][PF_6]/MMA Mixture Drops

The evaporation of the mixture [Bmim][PF_6]/MMA 1:1 (see figure 3.29) shows two evaporation stages: Fast evaporation of MMA and a drop of [Bmim][PF_6] remains. After 100 s MMA is almost evaporated from a initial volume V_0 of 360 nL (exp. 7). A second drop with a slightly higher initial volume V_0 = 417 nL (exp. 1) shows rather no difference in evaporation time. Actually the final volume of the drop is approximately 66 % (exp. 7) and 63 % (exp. 1) of the starting volume (3.29 (b)). For a 1:1 mixture by volume it was thought to be 50 %. Possibly this is caused by rapid evaporation of MMA during the deposition process. So until the measurement starts about 15 % is already evaporated. In this specific mixture no above mentioned evaporation law is fully applicable because the contact angle increases and the contact radius decreases over the evaporation time. Coincidental the volume V decreases initially linear. The change of the contact angle can be explained by the change in surface tension γ_L for the [Bmim][PF_6]/MMA mixture while the MMA concentration is reduced [81,82]. This is expressed by the Young's equation:

$$\cos\Theta = \frac{\gamma_S - \gamma_{SL}}{\gamma_L} \tag{3.7}$$

While the surface tension γ of the solid γ_S stays constant, an increase either in the surface tension of the liquid γ_L or the surface tension of the solid liquid interface γ_{SL} leads to an increase in the contact angle (assuming $\Theta \leq 90°$). Evaporation rate starts at around 4.5 nL/s and decreases monotonously until t∼100 s, then remains nearly zero. Thus, the evaporation rate is similar in the

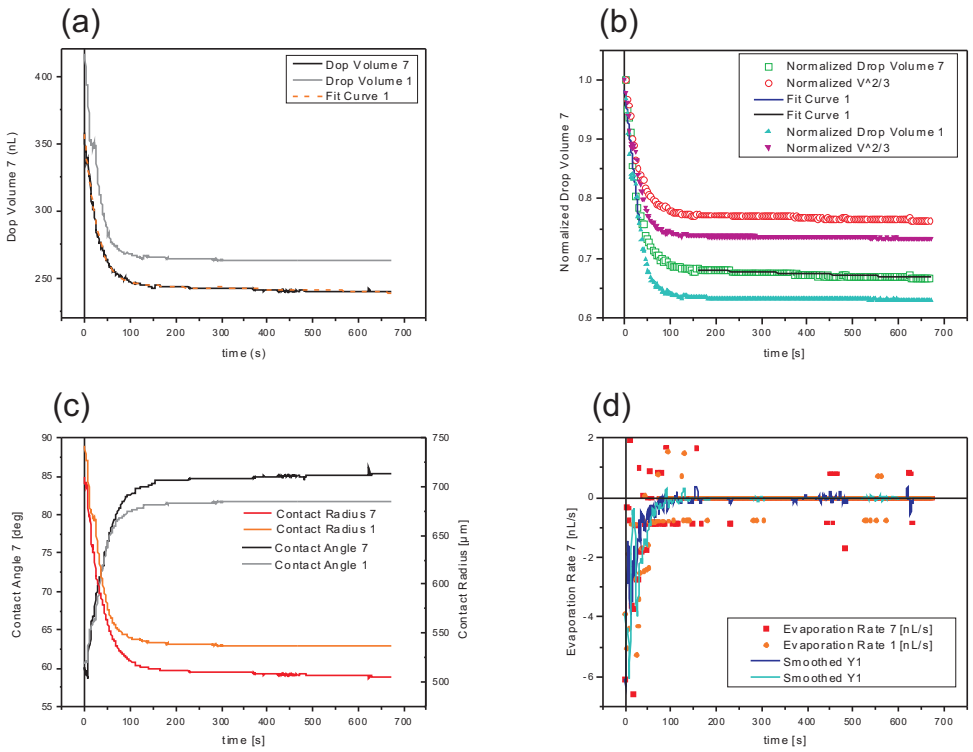

Fig. 3.29.: Results for the evaporation of [Bmim][PF_6]/MMA 1:1 mixture droplets. (a) There are two stages of evaporation present: first MMA evaporates quickly, which takes about t_1 = 100 s for a V = 360 nL droplet and then an ionic liquid drop does not evaporate. (b) Plot of the normalized volume V and $V^{2/3}$. In the beginning of the process the V decreases linearly but then it is leveling off. (c) The contact radius is decreasing and the contact angle increases constantly with time. Over the whole evaporation time no pinning is observed. (d) The evaporation rate starts at 4.5 nL/s and decreases monotonously until t = 100 s, and than remains almost zero.

beginning of the process but then slows down continuously to zero. This can be attributed to the fact when MMA evaporates that the concentration inside of the droplet decreases. Then the diffusion of MMA molecules to the rim of the drop can not be neglected.

3.6.5. Evaporation of [Bmim][PF_6]/DMF Mixture Drops

A drop of [Bmim][PF_6]/DMF mixture (see figure 3.30) with a volume of V_0 = 380 nL evaporates in two stages. First DMF evaporates within t =∼3000 s and second a drop of [Bmim][PF_6] remains. From the normalized volume vs. time plot one sees that the final volume is approximately 50 % of the initial volume. During the first ∼500 s the volume decreases linear with time ($V = V_0 - A_0 t$). However, from the contact angle and radius plot it can be concluded that non of the evaporation laws is applicable.
Initially the liquid mixture is pinned like the pure DMF drop. At around 200 s the drop is depinned and the contact radius decreases monotonously. However, the contact angle decreases first and then slightly increases, decreases again and finally stays constant (figure 3.30). The surface tension γ_L of the mixture [Bmim][PF_6]/DMF gradually increases while DMF evaporates until around 2500 s. This is seen by the increase of the contact angle (see equation 3.7). As the evaporation is finished also the contact angle stays constant. The evaporation rate starts around 0.25 nL/s and decreases monotonously until t∼3000 s and then remains nearly zero. Compared to the pure liquid the evaporation rate is slightly higher but slows down continuously to zero.

3.6.6. Evaporation of [Bmim][PF_6]/DMF/MMA Mixture Drops

The evaporation of a liquid mixture of [Bmim][PF_6]/DMF/MMA is the most complicated case of the tested mixtures and is divided in three stages (see figure 3.31). Until 60 s MMA evaporates fast, followed by the evaporation of DMF which takes about 2000 s. Both slow down to zero at the end at t∼3500 s when only [Bmim][PF_6] remains. The initial drop volume V_0 was 250 nL. Finally the volume is approximately 40 % of the starting volume.

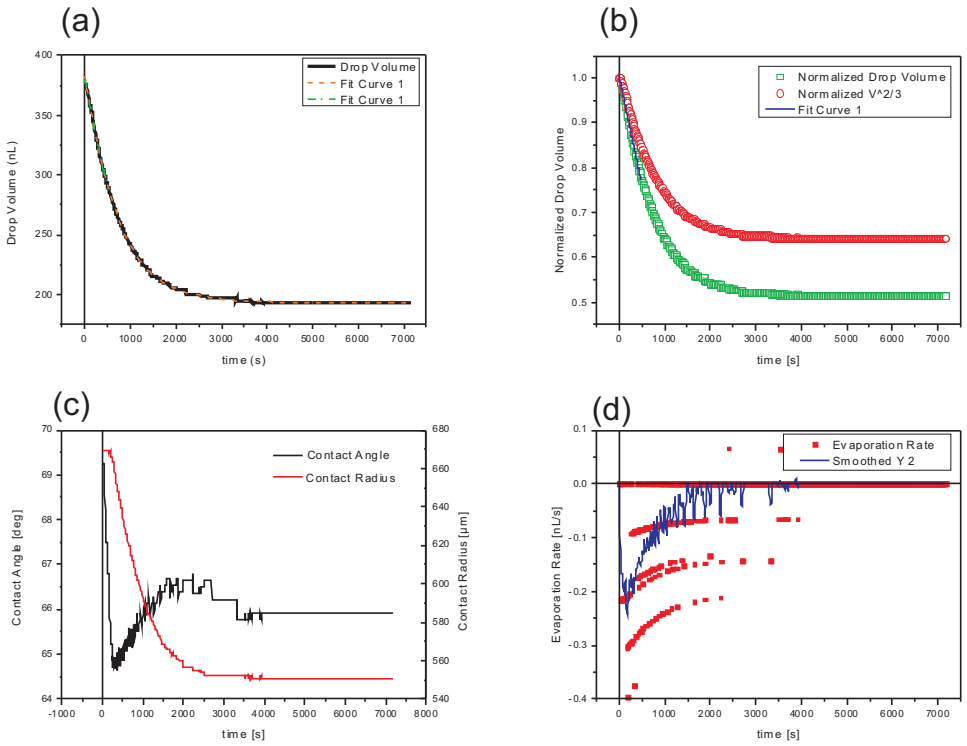

Fig. 3.30.: Results for the evaporation of [Bmim][PF_6]/DMF 1:1 mixture droplets. (a) The evaporation characteristics of the mixture IL/DMF is comparable to the one before (fig. 3.29). However, DMF evaporates much slower. A droplet of V = 380 nL needs to evaporate about 3000 s and then an ionic liquid drop does not evaporate. (b) Plot of the normalized volume V and $V^{2/3}$. In the beginning of the process the V decreases linearly but then it is leveling off. The intermediate regime is much longer compared to the [Bmim][PF_6]/MMA mixture. (c) After inital pinning the contact radius is decreasing. This causes that the contact angle first decrease and then increases slightly with time until 2000 s. (d) The evaporation rate starts at 0.25 nL/s and decreases monotonously until t = 3000 s, and then remains almost zero.

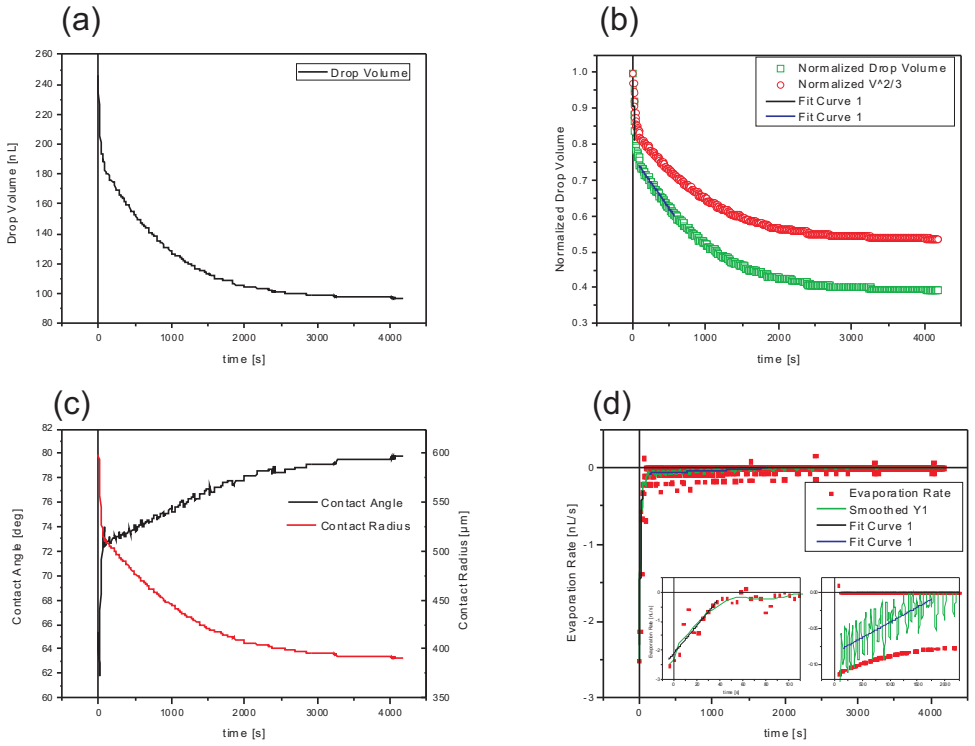

Fig. 3.31.: (a) The evaporation characteristics of the mixture IL/DMF/MMA shows three stages: First MMA evaporates within 60 s, then DMF evaporates until 2000 s and then evaporation slows down to zero. At the end a drop of [Bmim][PF_6] remains. (b) Plot of the normalized volume V and $V^{2/3}$. In the beginning of both processes the V decreases linearly but then it deviates significantly. (c) The contact angle increases over the complete evaporation time. Consequently the contact radius is decreasing. (d) The evaporation rate starts at 2 nL/s and decreases to a rate of 0.1 nL/s after 60 s and further decreases until 2000 s.

However, this was thought to be 33% for a 1:1:1 mixture. The final volume of DMF in the [Bmim][PF_6]/DMF mixture matched the ratio of 50 %. However, the final volume ratio of the [Bmim][PF_6]/MMA mixture was higher than the expected 50%. Therefore, it can be concluded that in this case the fast evaporation of MMA also influences the final volume. During deposition a significant amount of MMA is already evaporated until the actual measurement starts. Almost 6-7 % MMA evaporates before the measurement. Thus, it can be excluded that large amounts of MMA or DMF stay in the remaining [Bmim][PF_6] drop. The first and second stage follow the evaporation law $V = V_0 - A_0 t$. However, later on the evaporation schema clearly deviates from this law. As explained above the surface tension is a function of the concentration of the dissolved component. When either MMA or DMF evaporates their concentration decreases respectively and therefore the surface tension of the remaining drop increases which leads to an increasing contact angle. Both stages of evaporation show that the contact angle increases with time. Consequently the contact radius is also decreasing. One can distinguish between the two stages from the slope of the function contact angle /radius vs. time.

3.6.7. Summary and Conclusion

In summary, the experiments on evaporation of liquid mixtures from an ionic liquid drop can be divided into three stages. First one component evaporates quickly without significant reduction in evaporation rate compared to the pure liquid. Then the evaporation slows down because molecules are diffusing from the inside of the drop to the surface. Finally, a drop of pure ionic liquid remains.
The intermediated regime is for MMA ($\sim$60 s) about 40 times shorter than for DMF ($\sim$2500 s). This has consequences for the concept of ionic liquid microreactors. Monomers with a high vapor pressure are only usable within limitations. For μL droplets monomer can be sequentially added to the microreactor. This leads to a sufficient brush growth. However, in inkjet devices the droplet volume is going down into the sub nL regime. Thus, here most likely it is not possible to maintain a suitable monomer content inside the

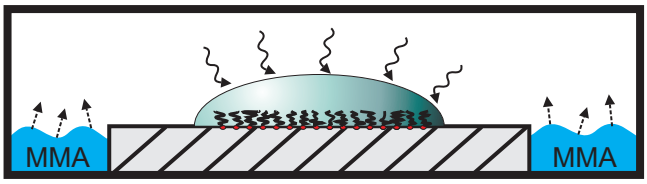

Fig. 3.32.: PMMA brush synthesis inside of a [Bmim][PF_6] drop. MMA evaporates into the closed volume and condensates in the ionic liquid drop where the ATRP reaction proceeds.

droplet, because most of the monomer will be evaporated before the drop settles on the surface and the rest will be gone before any reaction conversion appears. In the outlook (see 3.6.8) a new concept is described to overcome the difficulties.

3.6.8. Outlook

From the experiments shown in this chapter a new concept arose. All experiments done in this chapter are performed in an open system. However, by controlling the environment namely the content of MMA in the surrounding medium it might be possible to control also the preparation of the PMMA brush in the droplet. MMA condensates most likely into the [Bmim][PF_6] drop containing the ATRP catalyst. Preliminary results gave evidence on this concept. A [Bmim][PF_6] drop with the catalytic system described in section 3.4 was placed on a functionalized silicon substrate. This substrate was put in a volume of about 25 cm^2 and surrounded by one mL of MMA (fig. 3.32). The IL drop swelled by several orders of magnitude. As a result was found that the substrate was covered partially by PMMA brushes with an average thickness of 5 nm. For future experiments there are some important points to investigate: (a) the physical behavior of MMA condensation into an IL drop, (b) the brush growth by control of the vapor content (temperature, volume of MMA), (c) the interplay between (a) and (b). For example it might be that the polymer brush layer has a thickness gradient due to diffusion processes.

4. Patterning by “Inkjet Printing”

In the last century there was an increasing demand for easy processes to pattern/ structure surfaces in a controlled way. Different approaches such as soft lithography [83], photolithography [84], templating with block-co-polymers [85] are widely spread. For example photolithography is used to produce submicron sized structures in semiconductor industries. However, the involved processes are long, complex and inefficient with material usage. To overcome these difficulties direct and non-contact patterning from the liquid phase is of high demand to develop a rapid and cost efficient fabrication process. One sophisticated approach is the use of inkjet printing devices [20–22,86]. Nowadays, the potential of inkjet printers is capable of producing graphical printouts in photo quality with ink droplets of 16 μm in diameter.
Two essential parts are involved for the coating with inkjet printing. (i) the inkjet printing device, (ii) formulation and physical understanding of inks/ solutions capable for liquid processing. Precise positioning of the droplets is mandatory for high quality patterning. Therefore the print nozzles are need to be moved precisely with a x/y/z translation stage. Flexible print layouts are realized with assistants of the computer soft- and hardware. This omits the usage of masks or stamps to create complex pattern. The print nozzles have to eject stable drops with reproducible volume and a correct flight angle to hit a predetermined position on the target substrate. Droplet volumes are in the range of a few picoliter to microliter. Therefore the process is very efficient in the usage of material. These requirements are met by piezo-driven drop-on-demand (DoD) printers. In this thesis a commercial DoD inkjet printer from Gesim is used (see section 2.5). It is a state of the art system which is ideal for scientific research because it is robust, flexible in the usage of targets and easy programmable. More specialized systems are capable to produce smaller drops or have a more precise positioning but this costs versatility which is de-

manded in basic research.
Concerning the formulation and physical understanding of the inks/ solutions the following parameters are crucial: Viscosity and surface tension are basically influencing the droplet formation when the drop is ejected from the piezo-driven nozzle. Typically the viscosity should not exceed 5 mPa·s. In a specific range the actuation of the piezo element can be tuned by varying the voltage and pulse widths. So the variety of solutions is expanded to what can be used in DoD devices. The next point is the ink behavior on the substrate. Dependent on the substrate surface (wettability, contact angle, surface energy and roughness) self patterning of the drop may occur due to spreading. Additionally, the drying process effects the film formation. This may lead to non uniform and inhomogeneous coatings.
When droplets of suspensions or solutions are evaporating the so called "Coffee Stain" effect can occur [87, 88]. As precondition the drop must be pinned which is on rough surfaces most likely. Because of this geometry the evaporation rate is at the three phase contact line (TPCL) higher than at the center of the drop. This induces an outwards flow to replenish liquid at the TPCL. Thus, solvated or suspended material is transported to the rim and after complete evaporation a ring-like deposit along the perimeter is left. Typically this is an undesired effect because the film is not homogeneous. By varying the substrate properties [89], the solvent [90], and using solvent mixtures [91] it is possible to suppress the "Coffee Stain" effect.

In this chapter two ways are presented to structure surfaces on the micrometer scale. The first application utilizes the coffee stain effect to get microlenses on a polystyrene surface. In the second application, which does not suffer from the "Coffee Stain" effect, polyelectrolytes are employed to adsorb homogeneously on silicon by electrostatic interactions.

4.1. Restructuring of Polymer Surfaces by Solvent Droplets

*

This section describes the usage of a drop-o-demand inkjet printer (Nano-Plotter© see section 2.5) to restructure polymer surfaces. By depositing solvent droplets small microcavities are formed by several physical effects (see section 4.1) [92] . The flexibility and exact control of the printer facilitates the fabrication of microcavity arrays. The piezoelectrical principle of the pipette produces droplets with a high reproducibility. This leads to cavities with a defined diameter and depth which defines the radius of curvature. Therefore this is applicable to produce microlenses with variable focal lengths. Microlenses are common in nature [93] and are used in a variety of common devices in photonics, optoelectronics [94] and commerical CCD's, LCD projectors or collimators for optical fibers. Fabrication of microlenses is achieved by a wide list of methods [19]. Molding and casting optical materials are very common [95–97].

Microjet devices have also been used for producing microlenses, by depositing polymer solutions [86], as well as UV-curable optical adhesives, forming structures from plano-convex to convex-convex configuration [98, 99]. Yang et al. were able to tune the position and the radius of curvature of similarly deposited lenses by means of electrowetting [100, 101]. The viability of ink-jet etching on soluble polymeric surfaces has been already established by other authors to be applied in the manufacturing of microelectronic devices [102, 103]. Ink-jet restructuring of polymer surfaces for the fabrication of microlens arrays is based on off-shelf materials and low-cost experimental apparatus, is highly flexible, and suitable for mass production.

*This section is based on the following publication: Pericet-Camara, R., Best, A., **Nett, S. K.**, Gutmann, J. S., und Bonaccurso, E., *Opt. Express* **2007**, *15*(15), 9877–9882, Arrays of microlenses with variable focal lengths fabricated by restructuring polymer surfaces with an ink-jet device.

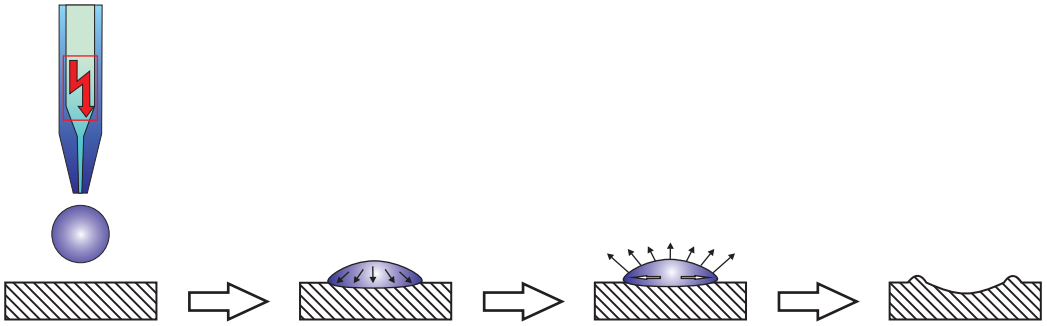

Fig. 4.33.: Schematic drawing of the microwell formation. In the first step a solvent droplet of around 0.4 nL is deposited on the polystyrene surface. The solvent forms a sessile droplet which pushes to the surface by the Laplace pressure. At the same time solvent diffuses into the polymer and dissolves and swells the surface. By the so called "Coffee Stain Effect" dissolved material is transported to the edge of the droplet and precipitates forming an outer rim. After complete evaportion of the solvent a small crater is left.

4.1.1. Microwells with Defined Diameter and Depth

This chapter describes the restructuring of polymer surfaces by depositing solvent droplets with a drop-on-demand inkjet printer. By placing individual droplets of toluene on an extruded polystyrene plate (220 kDa M_w, from Goodfellow Ltd.) a small spherical crater is left after complete evaporation (see figure 4.34). The evaporation takes place within one second. In order to dispense the solvent droplets a Nano-Plotter© (GeSiM GmbH, Germany) is used which is introduced in detail in section 2.5. In the following experiments a "Nanotip" is used i.e. the volume of one droplet is roughly 0.4 nL. The workplate layout is a rectangular matrix of n x n spots with a pitch of 250 μm between every spot. N is the number of rows and columns. First the printing head moves to the spot position and places a toluene droplet on the surface. The droplet settles and several physical effects contribute to form the crater. The bottom of the drop pushes towards the surface caused by the Laplace pressure. As well, the droplet is pinned at the three-phase-line due to the irregularities of the surface, pulling it upwards due to the surface tension. Simultaneously the solvent diffuses into the substrate to a certain depth, swells it, and dissolves part of the polymer. At the three-phase-contact-line the evaporation rate is higher compared to the middle part of the drop [104]. This leads to an outwards flow of the solvent inside the droplet. Thus, the

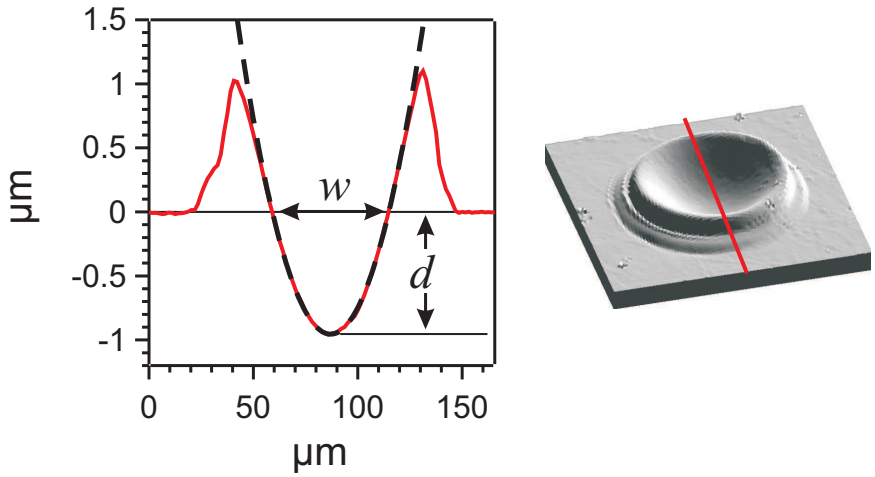

Fig. 4.34.: Profile and 3D-image of a single crater. The image is taken with a white light confocal profilometer (see chapter 2.4). The red line corresponds to the profile. In the profile the depth d and the diameter w are indicated. In order to obtain the radius of curvature R a circle function is fitted to the profile indicated by the dashed line.

solvent transports dissolved polymer to the edge and deposits it there. This phenomenon is known as the coffee-stain effect [87, 88]. In figure 4.34 the topography imaged by white light confocal microscopy (see section 2.4) is represented. A spherical cavity is left with a rim at the edge corresponding to the transported and deposited polymer. From the profile the physical parameters like diameter w, depth d and radius of curvature R are obtained. The radius of curvature R is the radius of the circle function fitted to the profile. Indicated by the dashed line in figure 4.34. A droplet creates a microwell with the average parameters: depth $d = 0.98 \pm 0.1$ μm, diameter $w = 54.6 \pm 6$ μm radius of curvature $R = 0.00124 \pm 0.0001$ μm^{-1}.

The inkjet printer allows to control the amount of droplets of equal volume which are dispensed at the same spot position. By default the nozzle ejects the droplets with 100 Hz i.e. 100 droplets per second. More than one drop at each position merge instantly to one big droplet. Consequently, the characteristics of a crater changes if the number of droplets is increased from 1 to 7 drops (see figure 4.35). The width increases from 145 μm to 184 μm and the depth increases by a factor of 4 from 0.48 μm to 1.97 μm. With an increasing number of droplets the diameter seems to level off. On the other hand the depth increases almost linearly. This is quite easy to understand in the context of the

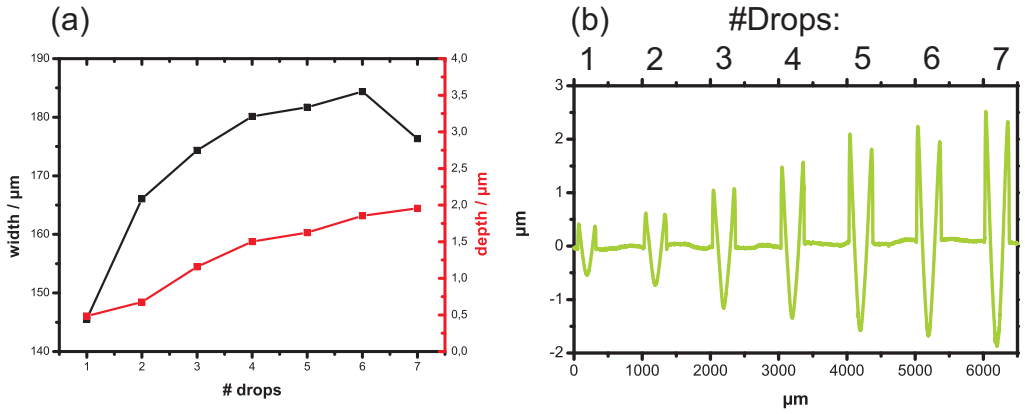

Fig. 4.35.: Width and depth as a function of number of drops. (a) Left axis corresponds to the width of the micro craters. Right axis is the depth of the micro craters. (b) Profile over microvessels with increasing number of drops.

droplet geometry as a spherical cap (see eq. 3.3 and 3.4). The diameter of the toluene drop does not scale linear with the volume and number of droplets. However, bigger volumes support higher material transport to the rim due to the enhanced contact time of the solvent which leads to deeper craters.
If a delay of 2 s between the ejection of two consequent droplets is introduced, then the second drop hits the surface when the first one is already evaporated. In figure 4.36 (a) an array of microvessels imaged by a confocal profilometer is shown. In y-direction the number of droplets is raised by one for each row. In x-direction the number of drops is kept constant. The solid and the dash lines are indicating the corresponding y- (in fig. 4.36 (b)) and x-profiles (in fig. 4.36 (c)). The diameter of around 49 μm is almost constant for all craters. However, the depth increases from 2 μm to about 3 μm. This means that the second droplet fills the existing crater instead of wetting the region around the crater. By the physical effects explained above new polymer is transported to the already existing rim rather from the bottom material than removed from the side. Thus, the depth increases whereas the diameter stays constant. This result is summarized in graph 4.37.

4.1.2. Fabrication of Convex Microlenses

The restructuring process may find application in the fabrication of microlenses. The craters represent plano-concave lenses. However, for most opti-

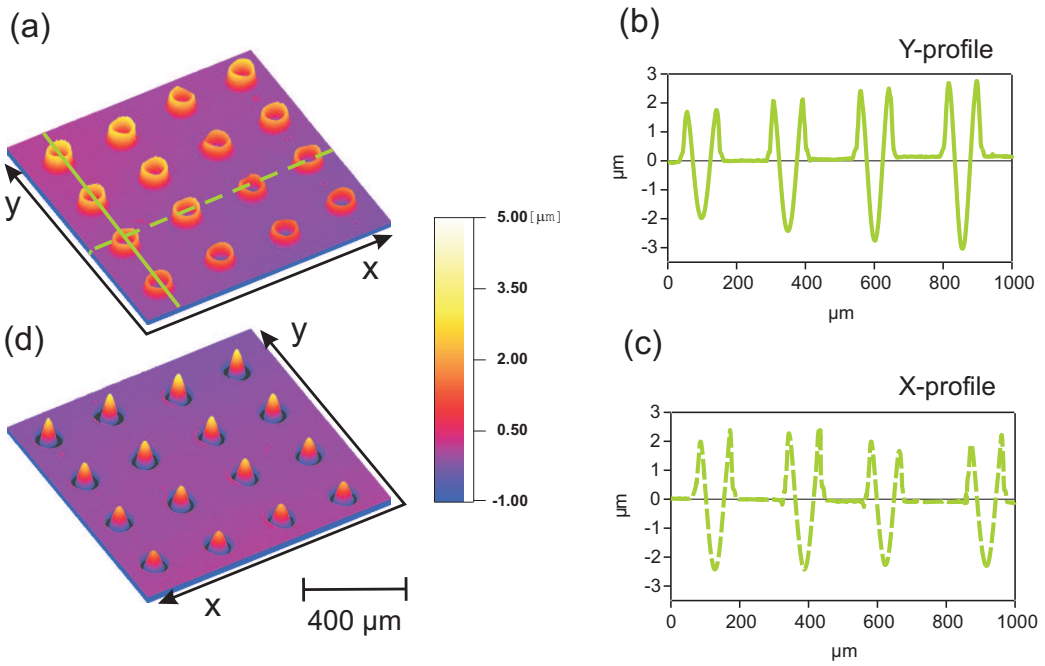

Fig. 4.36.: (a) 4x4 array of microwells. The array of craters was produced by depositing toluene drops on a polystyrene surface. In the direction of the solid line the number of drops is increased by one for each row. The corresponding profile (b) shows that the depth of the craters increases with every single droplet. (c) The dashed profile is taken along the dashed line in (a) and corresponds to craters created by the same number of drops. (d) 3D-structure of the convex microlenses prepared with a silicon elastomer using the microcraters from (a) as a mould.

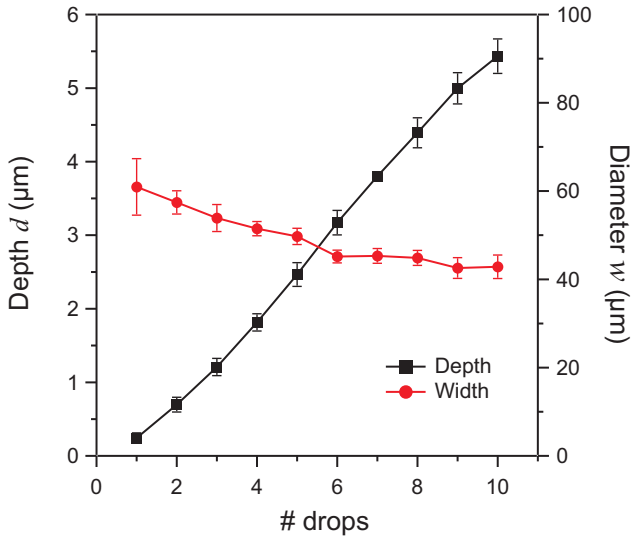

Fig. 4.37.: The graph shows the depth (left axis) and diameter (right axis) as a function of the number of deposited droplets. From one to ten droplets the depth of the craters increases linearly. On the other hand the diameter decreases.

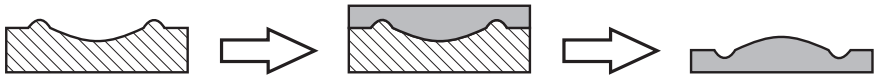

Fig. 4.38.: The arrays of microwells are plan-concave lenses. In order to obtain convex lenses which are much more practical the microwells are used as a mold. A commercial silicon elastomer Sylgard© 184 fills up the craters. After curing the silicon the mold and the replica are separated mechanically.

cal purposes convex lenses are needed. Therefore, the arrays of microwells are used as mould to cast plano-convex microlenses. The process is shown schematically in figure 4.38. An array of lenses (see figure 4.36 (a)) is produced. Then a commercial silicon elastomer (Sylgard© 184 from Dow Corning) is poured on the mould and spreads on the surface at ambient temperature. In an oven at 80 °C the elastomer is cured for 30 min. After that, both elements, the template and the sample, are separated mechanically. The corresponding array of convex lenses is imaged in figure 4.36 (d). Besides the geometrical properties the surface quality is of a special importance. Using a Nanowizard© (JPK Instruments AG, Germany) atomic force microscope in intermittent contact mode individual microlenses are probed. The root mean square roughness and peak-to-peak values of the surface are below 7 nm and 380 nm respectively for all of the studied samples. These values for the surface roughness are comparable to ones obtained employing other techniques [19].

The function of a lens is focussing rays of light. So, the fabricated lenses are tested with an elaborated setup. As explained above one characteristic parameter is the radius of curvature R. By fitting a circle function to the concave one obtains R. With equation 4.1 the focal length is calculated. n is the refractive index of the lens material.

$$\frac{1}{f} = \frac{n-1}{R} \tag{4.1}$$

Stated by the manufacturer n for the silicon is 1.43 at a wavelength of λ = 633 nm. In figure 4.39 (a) the calculated and experimental focal length are plotted as a function of the number of deposited drops. The graph shows that the theoretical focal length decreases with increasing number of droplets up to approximately seven drops, where the values of the focal length level off to a plateau around f = 0.21 mm. Now these values will be compared to

the experimental focal length. Characterization of the optical properties are achieved by a laser scanning confocal microscopy. A LSM 510 module and an Axiovert 200 M inverted microscope (Carl Zeiss AG, Germany) are employed. The technique is similar to the one used by Gu *et al.* [105]. The system consists of a HeNe-Laser with λ = 543.5 nm for the transmission scan. While scanning, the light of the laser transmits the lenses, bundled to the focal point and collected with a photomultiplier. In this manner cross-sectional scans are obtained. In figure 4.39 (b) the X-Z plane is imaged. The focal point can be identified at the position of the highest intensity. A profile in z-direction is extracted from this intensity map. For every lens one maximum is found and by fitting a gauss function to the profile the focal length is extracted (see fig. 4.39 (c)). This experimental value is also plotted against the number of deposited droplets. The graph shows that the calculated focal length and the "real" experimental focal length agree well except for a slight offset. From the experimental focal length the refractive index is determined to be n_{exp} = 1.38 $\pm$ 0.04 at λ = 543.5 nm. Besides the dependency on the wavelength this difference is maybe attributed to the a variation in the mixing ratio of the base and curing agent of Sylgard© 184 which yield a dissimilar value compared to the stated one from the manufacturer.

Besides the fabrication of microlenses more elaborated pattern are possible to make. This can be achieved with the flexible control of the inkjet printer. One needs to design a prototype and the printer can place the droplets on the programmed positions. The limitation in x-y resolution is not set by the motor movement which is 10 μm but by the wetting behavior of the liquid. If polystyrene is the substrate and toluene is the solvent for restructuring then the minimum structure size will be 49 μm.

4.1.3. Fabrication of "The MPIP Logo"

As an example to create customized patterns the logo of the Max Planck Institute for Polymer Research is used as template (see fig 4.40). The template is divided in three parts: a square to define the outer contour of the logo, the three filled circles of different diameter and the lines which are connecting the filled circles. All parts will be fabricated by placing toluene droplets with

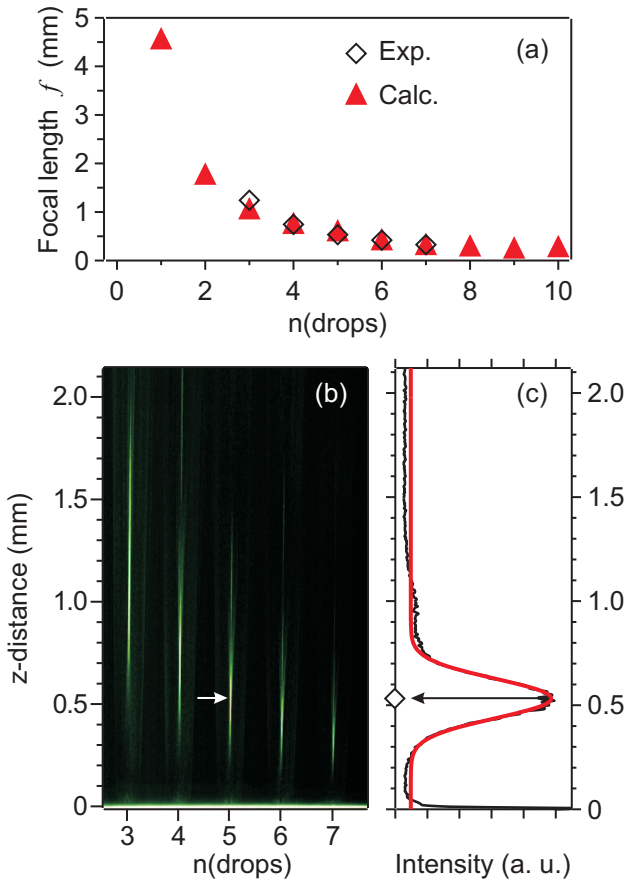

Fig. 4.39.: (a) Focal lengths f of an array of microlenses plotted as a function of the number of deposited drops. Red triangles are the calculated values (eq. 4.1) and the empty diamonds correspond to the experimental data. (b) Scan image in the X-Z plane of a convex microlens array by confocal measurement. The vertical green lines are the transmitted laser beams. The reflection scan image has been merged with the transmission one, and can be distinguished at the bottom of the picture as a bright green horizontal line. (c) Intensity profile along the Z-axis of a transmitted laser beam through a microlens obtained with 4 deposited droplets. This beam is pointed at (b) by the white arrow at its experimental focal point. The black line corresponds to the experimental data and the red one is fitted by a Gaussian function. The Z-value at the maximum determines the focal length of the microlens.

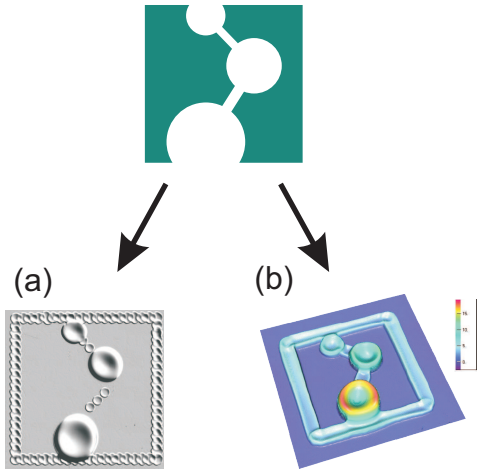

Fig. 4.40.: "The MPIP-Logo" as an example for micropatterning: a) First approach: the Logo just fabricated by restructuring with individual droplets of different volume. The long lines are made by single droplets. The big circles are made by depositing of 25:80:180 droplets. b) Second approach: the lines are made by a continuous flow of solvent while the pipette is move along. The big craters are prepared in the same way like in (a).

the drop-on-demand nozzle on a poly(styrene) plate. For the quadratic frame and the connecting lines single droplets are placed with a little overlap to each other. A three dimensional image obtained from the confocal profilometer of the restructured logo is seen in figure 4.40 (a). Every spot position is represented by a small crater. It is not optimal that the time to move the nozzle between two spots is so long because the drops evaporate. The filled circles are fabricated by placing an appropriate number of droplets at once. From top to down the diameter of the circles is increasing. The ratio is 1:1.5:2 (top to down). This ratio is hold for the fabricated craters by placing 25:80:180 droplets at 100 Hz.

Additionally, the Nano-Plotter© offers the possibility to operate the pipette in a constant flow mode (see section 2.5) i.e. the nozzle moves while droplets are ejected with the set frequency. Figure 4.40 (b) shows the surface profile of the MPIP logo where the quadratic frame and the connecting lines are made using the constant flow mode. With that optimization channels are formed instead of lines consisting of individual craters. Therefore, the restructuring process can also be applied to liquid geometries other than spherical droplets.

4.2. Polyelectrolyte Multilayer Structures

Polyelectrolytes are macromolecules which consist of ionic repeating units. This specific feature is used to modify surfaces [15]. Due to electrostatic interactions a charged polyelectrolyte dissolved in water adsorbs on an oppositely charged interface and a charge overcompensation occurs which is proven by Zeta-potential measurements [106]. The next oppositely charged polyelectrolyte forms the second layer, resulting in one bilayer. Consecutive repeating of the process leads to defined and uniform multilayer structures. This procedure is called layer-by-layer self assembly (LbL) (see figure 4.41) and was introduced by Decher et al. 1991 [15, 107]. The thickness of these multilayers can be tuned on the nanometer length scale by simply increasing the number of bilayers. Additionally, the process is influenced by the used type of polyelectrolyte/ salt [108], temperature [109], adsorption time, control of pH [110], concentration and amount of added ionic salt [111, 112].

There are a wide variety of applications [113] for using LbL self assembly of

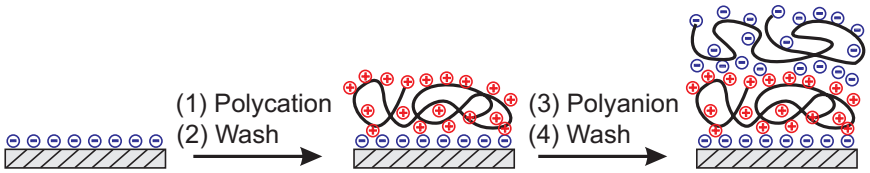

Fig. 4.41.: Schema of the Layer-by-Layer self assembly of the consecutive adsorption of polycations and polyanions.

polyelectrolytes. This includes optoelectronic devices with conjugated polyelectrolytes [114, 115], superhydrophobic surfaces [116], controlled release of DNA [117], ionpermselective films which switches the permeability for ions by changing the pH [118], membranes with polyelectrolyte multilayer gates to tune the penetrability by swelling and deswelling of the multilayers [119]. This process is not limited to planar surfaces, also spherical particles or colloids were coated by a shell of polyelectrolyte multilayers [120]. It is even possible to remove the core to get a hollow microcapsules [121].

Mostly, the multilayers are fabricated by stepwise dip coating procedure. This means that the negative charged substrate (e.g. silcon, glass) is dipped in the aqueous solutions on after the other: (1) polycation, (2) water, (3) polyanion,

(4) water. Each step requires an exposure time in the range of 20 to 60 min to remain in the respective solution. Modifications of the fabrication process were introduced for a faster build up of the individual layers e.g. the polymer solutions were applied to the substrate through spin coating [122] and spray coating [123–125]. Izquierdo et al. showed that the film quality of spray coated multilayers is equal or superior to ones which are dip coated although the adsorption time is noticeable shortened to about 60 s.
For many applications a structured coating of the substrate is needed e.g. electronic structures [126]. Several methods have been applied to pattern polyelectrolyte multilayers: (i) the surface is modified prior to the LbL self assembly so that PE adsorb selectively [127,128], (ii) the substrate is partially wetted by microfluidics [129], (iii) PEM films are patterned selectively after the LbL preparation was finished [130,131] through e.g. local etching [132], photoreactive multilayers [133] or stamping [134]. In this chapter inkjet printing as a direct patterning method of PEM is introduced to create 3D structures like lines, piles and rings. So far inkjet printing has been used to print water on PEM as developing agent and consecutive removal of the non cross linked regions wetted by the water [132]. Here, a fully automated process was developed to integrate all required steps to build up a LbL system. The polyelectrolytes poly(allylamine hydrochloride) (PAH, M_w = 70,000 g/mol) (fig. 4.42(a)) and poly(styrene sulfonate) (PSS, M_w = 70,000 g/mol) (fig. 4.42(b)) were used to build up the multilayer structures on silicon. This multilayer system was particulary interesting for these experiments because of the uniform and regular

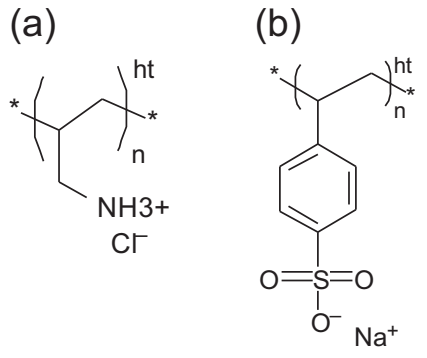

Fig. 4.42.: Chemical structures of (a) poly(allylamine hydrochloride) PAH and (b) poly(styrene sulfonate) PSS

arrangement of the cationic (PAH) and anionic (PSS) polymers.

4.2.1. General Process of Producing PEM Structures

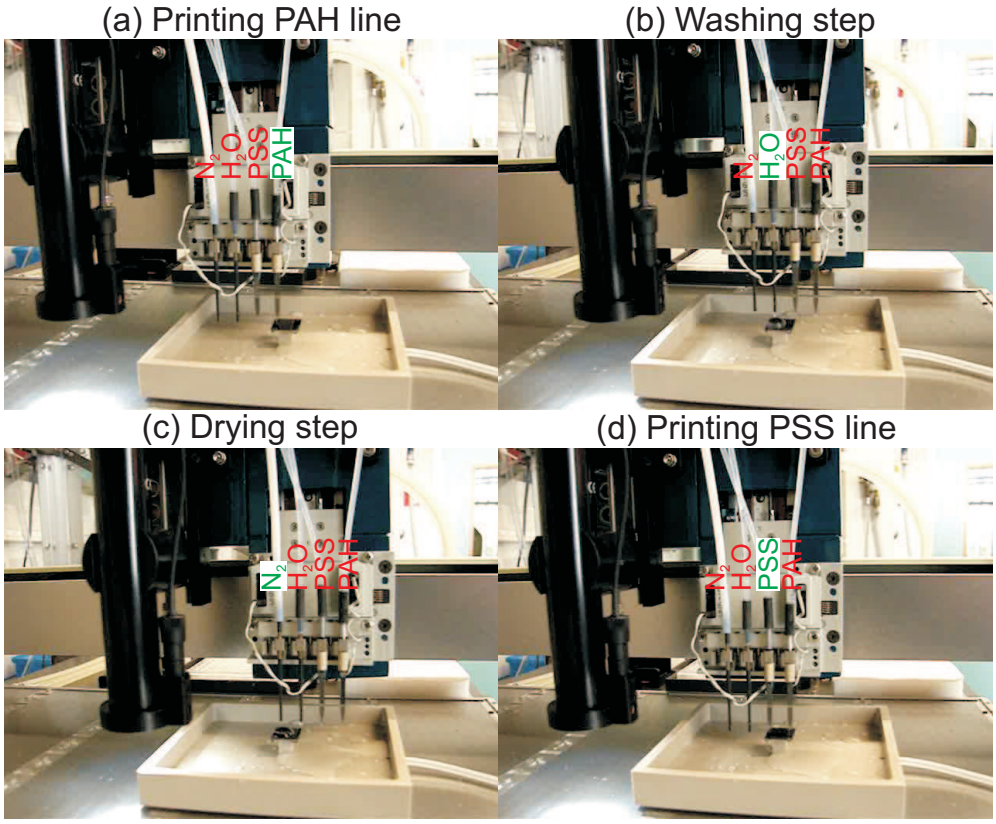

Fig. 4.43.: Automated procedure to print PEM structures using the Nano-Plotter©. The four mounted nozzles have the following function (enabled tip is marked green): (a) Printing of PAH solution using the first Nanotip, (b) Washing step with water, (c) Drying step with pressurized nitrogen, (d) Printing of PSS solution using the second Nanotip. The silicon substrate is mounted in the middle of the sample holder and is surrounded by a trough.

As described above LbL multilayers are fabricated by repeated immersion of a substrate in the polyelectrolyte solution always followed by a washing step until the desired number of PAH/PSS bilayers are deposited. This procedure is adapted to create 3-dimensional structures using the Nano-Plotter© (see section 2.5). Therefore a fully automated print process was developed (see fig. 4.43). The print head can hold up to four print nozzles at once. One nozzle, in this case a Nanotip, was used for PAH solution, another nozzle,

a Nanotip again, was used for PSS solution. The third nozzle, a passive tip, basically a rigid tube, was used to flush water over the substrate. The fourth available nozzle, also a passive tip, was used to dry the sample afterwards. The Nanotips and the first passive tip were connected to a syringe pump via a teflon tube. This configuration allowed to load the Nanotips with the polyelectrolyte solutions and pump several hunderd μL of MilliQ water over the substrate. The last passive nozzle was connected to pressurized nitrogen. An external valve activated the nitrogen stream and this stream dried the sample surface prior to the start of the next cycle. All components were controlled by the Nano-Plotter© software (confer to appendix: B).
The line structure is made by a continuous drop positioning (described in section 2.5). Each droplet had a volume of about 0.1 nL with a radius of 25-30 μm checked by video microscopy directly before the printing process. The ejecting frequency was 100 Hz or 100 drops per second. The tip is moved with a velocity of 5 mm/s. This means that a 5 mm line is printed within 1 s consisting of 100 droplets. The high positioning accuracy of the print head assured that the desired print positions can be reached precisely by every chosen tip i.e. the droplets of different tips can superpose each other exactly.
The substrate, a silicon wafer, was glued on the center of a sample holder, made of brass, which was surrounded by a trough to collect up the wash water. To reduce the evaporation rate of the aqueous solution the sample stage is cooled by an external chilling circulator to a temperature of 10 °C at the sample surface.

4.2.2. Printing PEM Line Structures

The quality of the first printed PAH line is of importance for the pattern of the multilayer structure. The surface charge is only overcompensated in the wetted region where this polycation adsorbs. In the following PSS adsorbs only on the area of the first layer. Usually, hydrophilic silicon as a substrate is incorporated in the LbL process. However, hydrophilic silicon has a contact angle close to 0 °. Therefore hydrophilic silicon substrates have the disadvantage that the aqueous solution of PAH spreads wide and undefined so that

the outer edges of the patterns were significantly deformed. Apart from the irregular edges, the line width also varied largely (see fig. 4.44). According

Fig. 4.44.: A 20-bilayer PEM line was plotted directly on the surface of a Si substrate that was freshly cleaned by the Piranha solution (see experimental section 7.9). The picture was taken with a light microscope under bright field.

to the literature, the positively charged molecules PAH are assumed to take flat configuration on the silicon surface due to the strong electrostatic interaction. However, the molecules are not able to fully cover the entire surface, instead they leave quite a few defects that are filled in the successive assembly steps. Therefore the surface, especially at the edge of the plotting, is highly inhomogeneous. Thus, to overcome this difficulty a less hydrophilic and more homogeneous surface is preferred before the plotting starts.
The contact angle of the silicon substrate is increased by immersion of the whole substrate in a PAH/$CaCl_2$ solution for 5 to 10 min and then rinsed with a large amount of water, followed by immersing in PSS/$CaCl_2$ solution for the same duration and rinsed again with water and finally dried in a N_2 stream. It turned out that $CaCl_2$ used as electrolyte for the first two bilayers gave the best result for the subsequent printing of PAH/PSS in NaCl solution. The terminated surface is negatively charged PSS and the contact angle was measured to be $27 \pm 3^\circ$ instead of close to 0°. On top of the polyelectrolyte (bilayer) coated silicon the first layer of PAH was printed using one Nanotip loaded with PAH/NaCl (see figure 4.45 (a)). The liquid film was incubated for a fixed time to let the polyelectrolyte molecules adsorb on the surface. Afterwards, the substrate was flushed with water (fig. 4.45 (b)) and dried with pressurized N_2 (fig. 4.45 (c)). Then the polyanion was plotted using the tip loaded with PSS/NaCl (c = 0.5 mol/L) at the same position where PAH solution was applied before (fig. 4.45 (d)). The formation of one bilayer (BL)

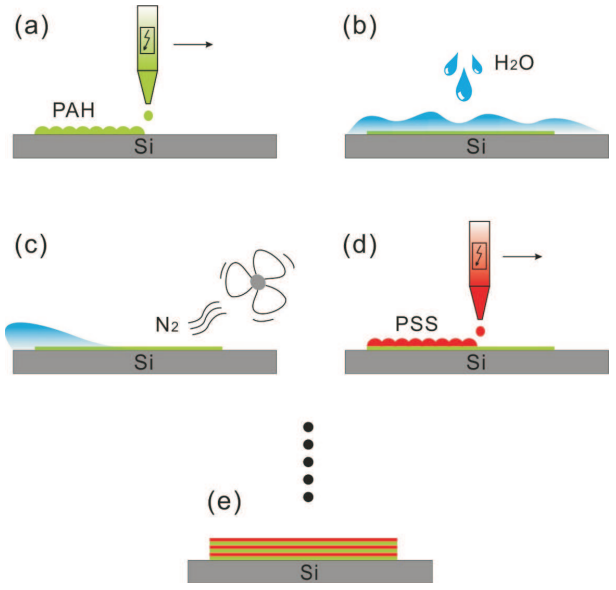

Fig. 4.45.: Sketch of the fabrication process of the polyelectrolyte multilayer patterns: (a) inkjet plot with PAH (b) rinse with distilled water (c) dry the surface under N_2 flow (d) continue to plot with PSS (e) the final polyelectrolyte multilayers.

is finished with the rinsing and drying step. Such a deposition process can be repeated until the desired numbers of BL's have been fabricated. If more than one structure is printed consecutively then the PE solution is placed at all positions before the sample is washed. A line is formed by merging 100 droplets to one elongated drop of a total volume of 10 to 40 nL. Immediately after depositioning of the PE solution evaporation takes place. If the solution dries completely before the substrate is washed with water, then the resulting film is inhomogenous. A series of six lines were prepared with a total number of 20 BLs (c(NaCl) = 1 mol/L). A line profile over the first four lines that were dried (1st to 4th in figure 4.46) shows a not reproducible film formation. The shape has defects and is not flat. In contrast the 5th and 6th line (fig. 4.46) are quite homogenous and the thickness of 70 nm and 65 nm scales with 3 nm per BL which was found in previous studies [135] for the classical LbL process by x-ray reflectivity using a salt concentration of 1 mol/L. In this case the liquid did not evaporate completely and had a contact time of 3 to 6 s. So it can be concluded that it is important to keep a minimum adsorption time which is limited by the total evaporation time of the solvent. In order to reduce the evaporation rate the sample stage is cooled to 10°C .

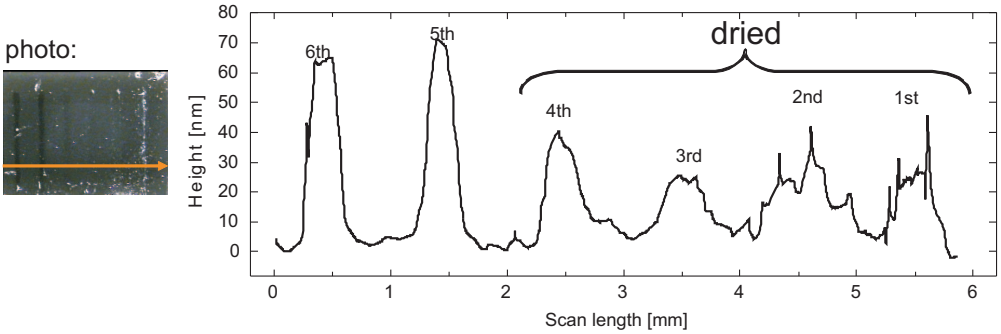

Fig. 4.46.: Six 20-bilayer PEM lines were plotted next to each other with a distance of 1 mm. First the PAH solution was plotted for all lines at once. Then the substrate was cleaned with water and dried. Afterwards, PSS was deposited for all lines and so on until 20 BLs are formed. The line indicated as 1st was printed as the first line followed by the 2nd, 3rd,....

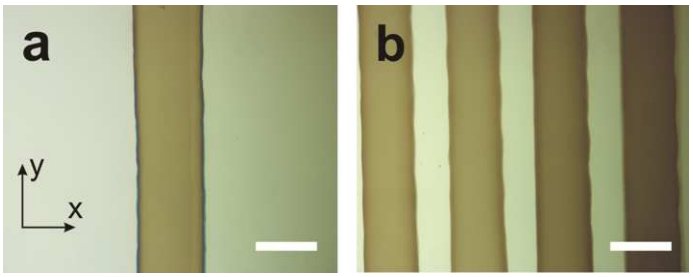

Fig. 4.47.: Example of PEM patterns printed on silicon modified with one bilayer PAH/PSS: (a) a single line (b) line array. The scale bars are 200 μm.

However, adsorption time was kept < 20 s because depinning was assumed to start afterwards. A line of PAH/PSS multilayer film (20-bilayers) is shown in fig.4.47(a). The complete line is 5 mm long and the light microscope picture shows a part of it. The edges of the line are straight and the waviness of each edge along y-direction of the whole line section in fig.4.47(a) is estimated to be not more than 6 μm. The black curve in fig.4.48(a) describes the continuous change in line width at all positions along the y-direction in fig.4.47(a). The histogram shows the frequency counts of all values of line width obtained and the Gauss fitting indicates the line width scattering around 230 ± 3 μm. The distribution of the line width obtained above, with a small standard deviation of about 1.31 %, can also be used to assess the stability in performance of the plotting technique. The surface profile of the PEM lines was measured using the white light confocal optical profilometer μSurf© (NanoFocus AG, Germany). A typical profile of the cross section area of an array of PEM lines

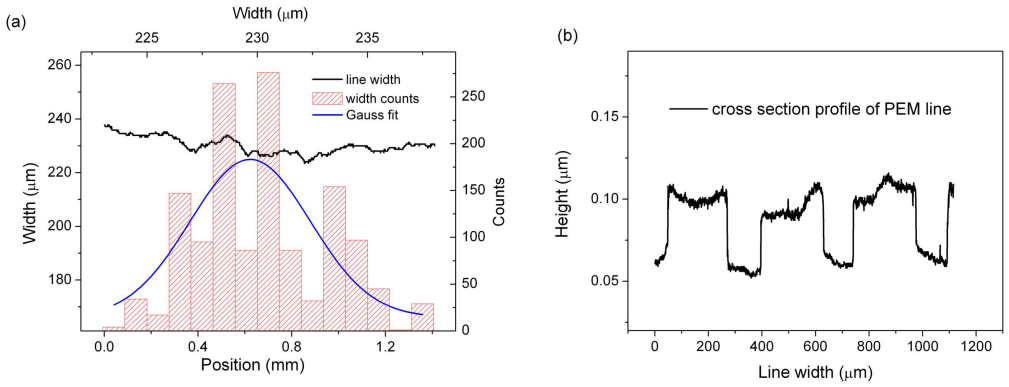

Fig. 4.48.: Statistics of the PEM line shown in figure 4.47(a): (a) the black curve shows the width of the PEM line along the y-direction (fig. 4.47(a)). The values were obtained by measuring the width between the two edges of the line at each pair of pixels (aligned in x-direction) on the digital graph. The histogram counts all the width values with increment of 1 μm and a Gauss fit indicates the line width centers at around 230 μm; (b) the profile of the line array (Fig. 4.47(b)) along the x-direction across the width of the PEM lines.

in fig. 4.47(b) is shown by the black curve in fig. 4.48(b). The PEM films in this case have 20 bilayers. The profile is taken along x-direction at an arbitrary position. The profile shows that the average height values of the array of lines are within 30 to 45 nm. Especially, looking only at the six sharp edges of the three lines, they have the height value from left to right 44 and 44 nm, 35 and 39 nm, 43 and 44 nm, respectively. The height values of the edges are quite uniform in pair. However, between the edges, the film thickness is smaller, normally around 35 nm, and the profile shows ups and downs. The maximum height difference can be up to 10-15 nm. Meanwhile, the base line in between the PEM films also shows inclination with a comparable scale up to 10 nm. Taking into account of the changes in the base line, the real fluctuation of the PEM line surface is believed to be not more than 10 nm and the thickness in the middle part of a 20-bilayer PEM line is estimated 30-35 nm.
The profile obtained by optical profilometer indicates a surface waviness of around 3 nm. According to the results of atomic force microscopy (AFM) measurement, the surface roughness R(rms) varies from 1 nm to 4 nm (excluding features like edges or overlaps and disregarding different number of layers), which is consistent with optical profilometer. Therefore, the method of optical profilometer is very convenient and sufficient enough in providing

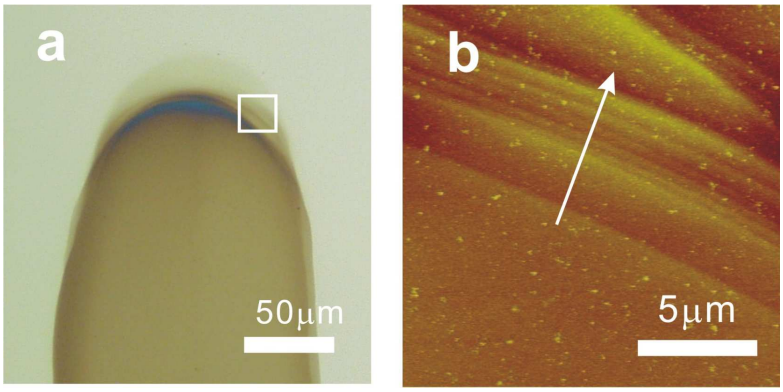

Fig. 4.49.: Light microscope picture of one end of a 20-bilayer PEM line; (b) a zoom-in scan of the area within the white box marked in (a), the arrow indicates steps of single layer of polyelectrolyte film.

general information of the surface profiles. At the edge by the end of the 20-bilayer PEM lines, steps of polyelectrolyte layers (fig. 4.49(a)) were observed, which are not very well superposed with each other. AFM was used to investigate the surface structures at the edge of the film. The steps of multilayer are clearly visible in fig. 4.49(b). Along the direction of the white arrow, the number of layers decreases and the thickness of the multilayer film gets smaller. Statistics of the height difference between neighboring steps are made: the step height (assumed as the thickness of a single layer of polyelectrolyte film) is 0.79 ± 0.15 nm, the standard deviation about 19% of the average. With the average height 0.79 nm for a single layer, a 20-bilayer PEM line has the total thickness of 31.6 nm. This value is in accordance with observation using white light optical profilometer. The single step heights scattered between 0.6 and 1.1 nm; therefore, the total thickness of a 20-bilayer PEM could vary from 24 to 44 nm. The specific results might be affected by operation conditions like local temperature, humidity, time of adsorption, viscosity and evaporation of the polyelectrolyte solution, salt concentrations, etc.

4.2.3. Chessboard Structures

The plotting of a chessboard PEM pattern is simply superposing two line arrays shown in fig. 4.47(b) atop each other with a rotation of 90 degrees. A typical light microscope picture of a chessboard PEM pattern is shown in fig.

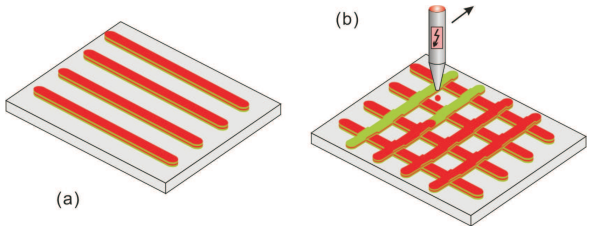

Fig. 4.50.: Sketch showing the process of making a polyelectrolyte multilayer pattern: (a) the line array and (b) the completed chessboard.

4.51(a). The area of beige color is the silicon substrate. The brown area is the PEM line arrays (20-bilayers) and the light-blue squares (40-bilayers) are the superposed crossings of the line arrays plotted in perpendicular directions. The multilayers form certain optical band-pass that reflect light with some wavelengths extremely stronger than the rest, acting as a filter, thus causing the multilayer films of different thicknesses to show different colors. Figure 4.51(b) is the three dimensional topography obtained with the white light optical profilometer. The three crossings on the left hand side of the figure show very unsmooth surfaces. This is actually an artifact. The surfaces at the three crossings are much less jagged as shown in the picture, but were dried before rinsing and got cracked. The layers near to the surface were destroyed and air could get in. The fragments of the films together with the air filled volume inside the film act as numerous tiny reflecting mirrors and can scatter light very strong. The light intensity obtained here is much higher than a normal film surface and therefore, the automatic analysis creates a surface with exaggerated cragged look.

The topography at the corner of a crossing was imaged by AFM (fig. 4.51(c)). The four quadrants are clearly distinguishable from each other in heights. Some parts of the edges show not well overlapped layers. However, it is almost not possible to tell along which direction the 20-bilayer line was plotted first. The profile along the red line in fig. 4.51(c) is shown in fig. 4.51(d). The three steps are clear and the edges are sharp, with very uniform step heights of about 30 nm. Thus, although the complete plotting of such a 5×5 chessboard (10 lines in total) took around two hours, the PEM film as well as the plotting conditions were stable with time.

A further step in making chessboard PEM patterns leads to a variation in

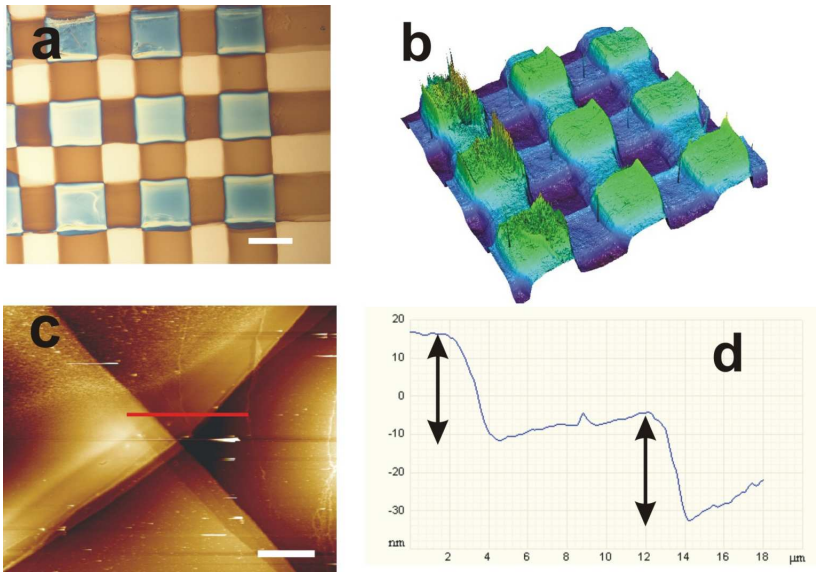

Fig. 4.51.: Characterization of chessboard pattern: (a) light microscope picture under bright field - scale bar is 200 μm (b) three dimensional topography obtained by white light profilometer NanoFocus (c) graph obtained on the borders of a crossing using atomic force microscope - scale bar is 10 μm (d) sectional profile along the red line in picture (c), the two double headed arrows showing the step height of 20 PAH/PSS bilayers is around 30 nm.

the number of overlapping layers, i.e. the film thicknesses. The chessboards with gradient in film thickness and colors are shown in fig.4.52. The sample on the upper half was prepared with polyelectrolyte solutions containing 0.5 mol/L NaCl, same as all the examples shown up to now. It shows the color of 10, 20, 30, and 40 PAH/PSS bilayers, respectively. The beige, brown, dark blue, and light blue colors can easily be correlated to the corresponding film thicknesses. The lower half of fig.4.52 is a sample that was prepared with polyelectrolyte solutions containing only 0.2 mol/L NaCl. In this case, colors of 10, 20, 30, 40, 45, 55, 65, and 75 bilayers are collectively shown. Indicated by the color of the films, one can easily find 45 bilayers prepared with 0.2 mol/L NaCl containing solutions has almost the same thickness as 30 bilayers prepared with 0.5 mol/L NaCl containing solutions. The thickness of 40 bilayers built with 0.5 mol/L NaCl solutions lies in between 55 and 65 bilayers built with 0.2 mol/L NaCl solutions. A simple estimation is made: for films built with polyelectrolyte solutions containing 0.5 and 0.2 mol/L NaCl, the resulting film thickness of same number of layers is round 1.5:1. The gradient

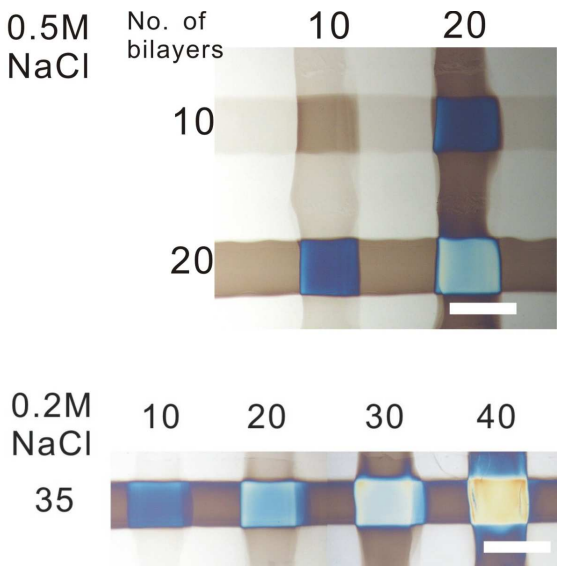

Fig. 4.52.: Light microscope (bright field) pictures: gradient of colors in a chessboard pattern with different layers and thicknesses. The NaCl concentration is 0.5 M (mol/L) for the upper sample and 0.2 M for the lower one. Scale bars are 200 μm.

colors provide a fast approach that can be used to evaluate the effect of salt concentrations on film thicknesses. The sample on the lower half of fig.4.52 shows a yellow colored crossing of 75 bilayers on the right hand side. For the sample prepared using 0.5 mol/L NaCl containing solutions, the yellow color appears at about 50-55 bilayers (not shown here). Continuous plotting with more polyelectrolyte layers in these experimental conditions leads to destruction of the PEM layers close to the surface by fast drying. One possible reason is the following: the elevated height of the PEM causes newly plotted solution no longer stable on top of the PEM, but to flow aside down to the silicon substrate. The liquid remaining on top of the PEM gets thinner and evaporates faster, thus it dries and cracks before rinsing with distilled water. Therefore, reducing the adsorption time can keep the PEM surface in good shape, however, also result in polyelectrolyte layers of smaller thicknesses.

4.2.4. Piles and Rings

There are a lot of more options to design PEM patterns due to the fact that a PE specifically adsorbs on the oppositely charged PE. Beside the chessboard, three additional designs were probed: (i) piles, (ii) hairline, and (iii)

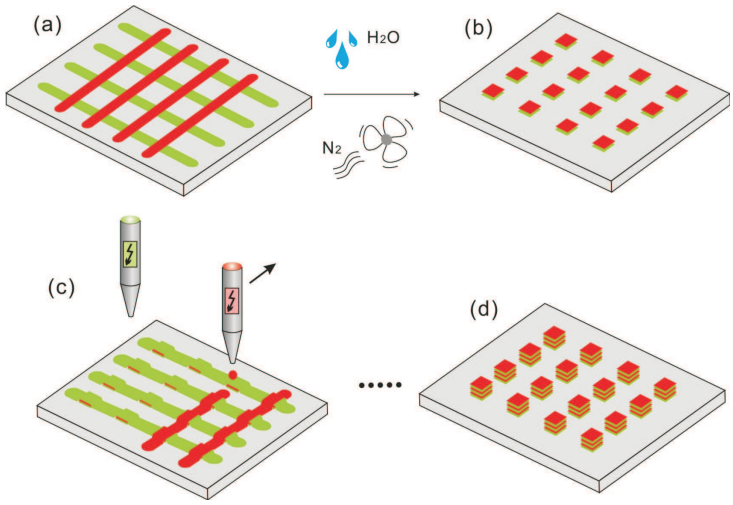

Fig. 4.53.: Sketch of the process of making a polyelectrolyte multilayer array of dots or piles: (a) plot a PAH/PSS cross pattern (b) rinse un-overlapped parts away with distilled water and dry under N_2 flow (c) repeat to make a PAH/PSS cross pattern (d) after a desired number of rounds, an array of PEM films patches is formed.

ring. In order to get piles of bilayers, PAH and PSS are plotted alternatively in 90 degrees with respect to each other. First a line of PAH is printed on the substrate. PAH adsorbs on the wetted region. Then PSS is printed perpendicular to the PAH line (fig. 4.53(a)). PSS just adsorbs on the PAH coated parts of the sample. After the washing and drying step an array of dots remains fig. 4.53(b)). Repeating cycles lead to a pile of PAH/PSS bilayers (fig. 4.53(c)+(d)). An almost rectangular stack of bilayers is formed with a side length of 240×200 μm (fig. 4.54). In figure 4.54 PAH was printed horizontally and PSS was printed vertically. The disadvantage in this design is that from the beginning of the LbL formation the adsorbed PAH line on the substrate remains and is uncontrolled contaminated by some polymer molecules during the further washing steps. Finally, this PAH line resulted in one-third of the complete thickness of the pile structure. The next design option is that PAH and PSS are printed in the same direction, but an offset perpendicular to the line direction is introduced. So that just part of the printed lines are overlapping. This should result in an hairline which has a significant smaller width than a line structure discussed previously (fig. 4.48). The experiment shows two line structures, a basic structure (fig. 4.55) with a width of about 220 μm and a fine line structure with an average width of 20 μm. However,

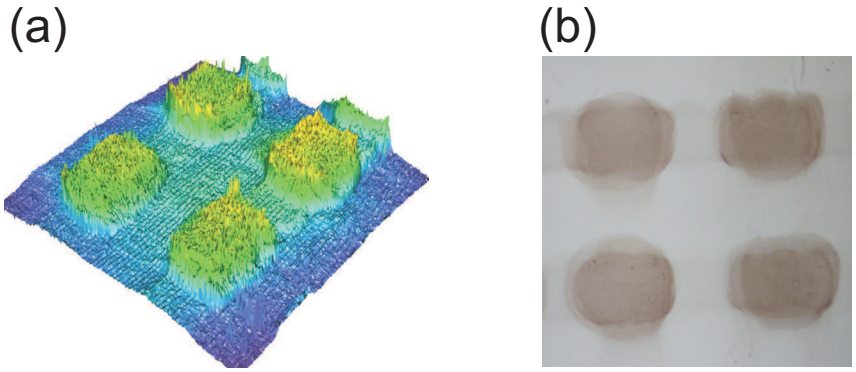

Fig. 4.54.: (a) Confocal microscope image of four piles created by 20 BL formation. The side length is 240×200 μm and the height of the piles is 45 nm. (b) Brightfield microscopy image of a similar 2×2 array. PAH was printed horizontally and PSS was printed vertically.

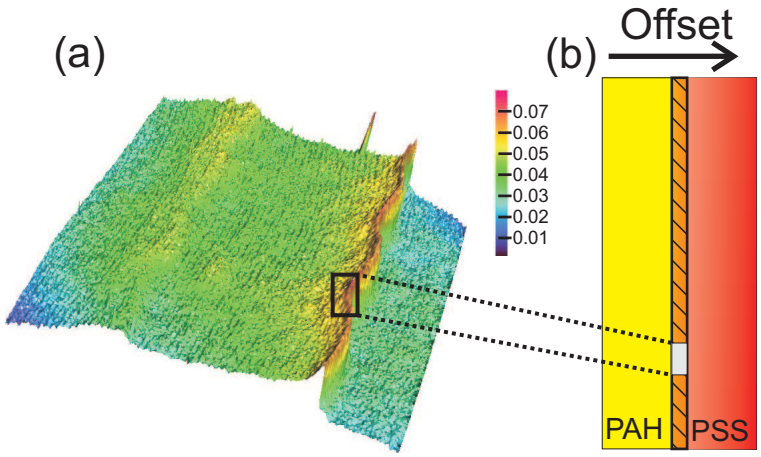

Fig. 4.55.: (a) 3D image of a line structure where PAH and PSS solution were plotted with an offset perpendicular to the line direction. (b) Sketch of the printing position of the PE lines. The PSS line is shifted by an offset of 200 μm to the left. Theoretically the PEMs are just formed in the overlap region. Due to wetting and contamination effects PEM are build up on the entire PAH region. However, the edge of the PEM line shows a sharp hairline with an average width of 20 μm.

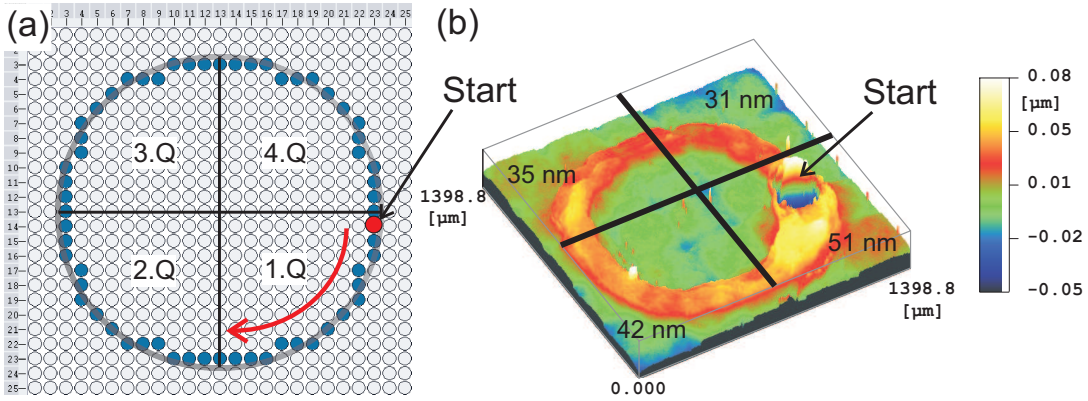

Fig. 4.56.: (a) Programmed drop positions on a raster marked as blue points. (b) 3D image of the printed PEM ring structure measured by optical confocal microscopy. The position where the print process started is marked. For every quadrant the average thickness of the 20 BLs is given.

the thickness (d = 23 nm) of the wide line is half of the expected thickness for 20 BLs, while the overlapping hairline fulfills the expectations of 47 nm thickness. There are two possible contributions to the build up of the wide line. Preferably, the PSS solution wets the positively charged area of the substrate i.e. the drops of PSS run on the PAH surface. During the washing steps the neighboring areas are contaminated in a similar way as discussed for the line in between the pile structures. A more elaborated design is a circular ring structure. The Nano-Plotter© does not have the possibility to draw a circle in a continuous movement used in the line structure. Bresenham reported an algorithm that determines which points in a n-dimensional raster should be plotted in order to form a close approximation to a straight line between two given points [136]. Based on that work the algorithm was modified to plot a circle on a n-dimensional raster [137]. This algorithm is incorporated to print a PEM pattern in a ring structure (fig. 4.56(a)). From the start position, marked in fig. 4.56, the print head moves step by step to every position clockwise on the 21×21 matrix with a pitch of 200 μm and the drops of the PE solution are placed accordingly. This procedure is much longer compared to the printing of a line (5 mm/s). In total it took 40 s for printing one layer consisting of 84 drop positions. Directly after the printing of one PE solution the substrate is washed i.e. the adsorption time for the molecules changed gradually from

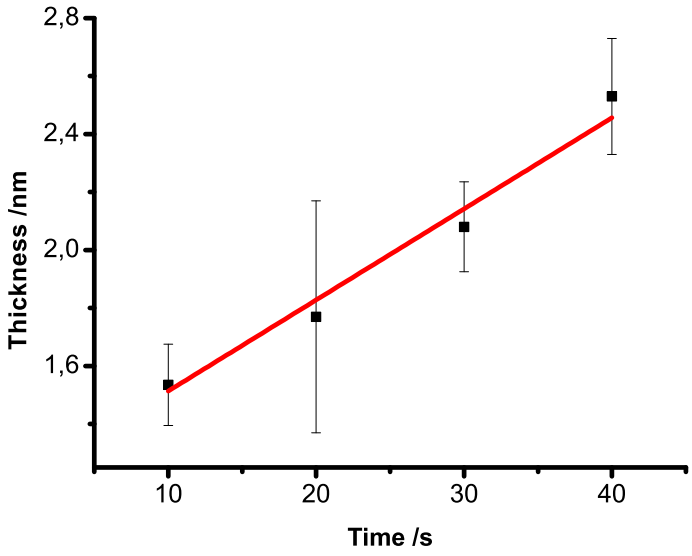

Fig. 4.57.: The graph shows the correlation of the adsorption time in seconds with the bilayer thickness in nm.

the start point (40 s) to the end point (1 s). The resulting ring structure had a radius of 465 $\pm$ 20 μm and a thickness gradient along the printing direction (fig. 4.56 (b)). For every quadrant the average thickness is determined; 1. quadrant: 51 $\pm$ 4 nm, 2. quadrant: 42 $\pm$ 3 nm, 3. quadrant: 35 $\pm$ 8 nm, and 4. quadrant: 31 $\pm$ 3 nm. The thicknesses per bilayer were calculated from these averaged values. For simplification the longest time of adsorption was chosen for every quadrant (40, 30, 20, 10 s). The correlation of thickness per bilayer vs. the longest time of adsorption is found to be almost linear neglecting the error bars (fig. 4.57). It can be concluded from the ring structure design that the thickness of the bilayer increases with adsorption time. This trend is in agreement with the literature [124].

In section 5.2 the LbL coating of nanomechanical cantilever sensors and the NCS response on exposure to humidity are demonstrated.

5. Application of Nanomechanical Cantilever Sensors

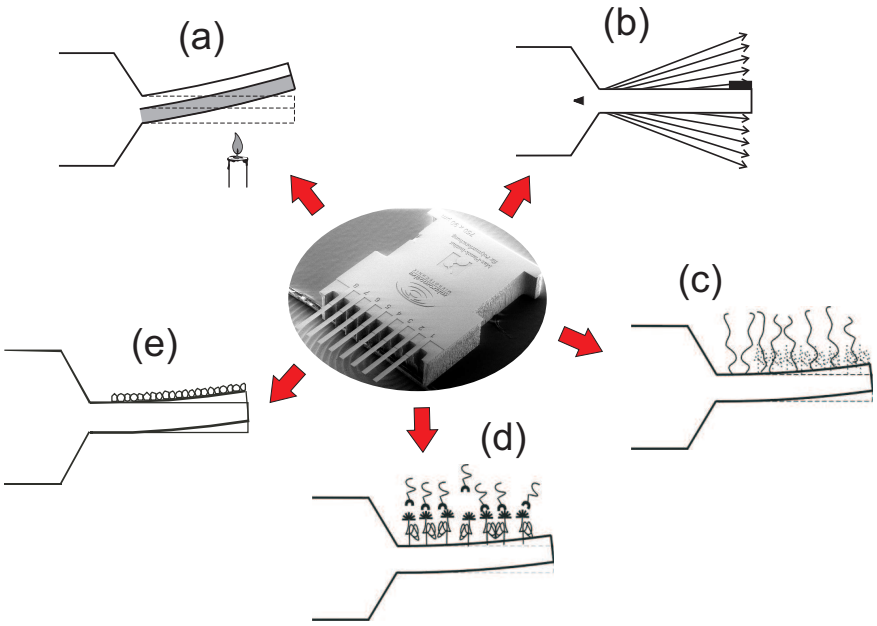

Fig. 5.58.: Applications of nanomechanical cantilever sensors. In the middle SEM image of a nanomechanical cantilever array OCTOSENSIS. The silicon microarray consists of eight rectangular cantilevers, with a length of 750 μm, width of 90 μm and thickness of 1, 2 or 5 μm arranged at a pitch of 250 μm. (a) Calorimetric detection (b) Dynamical mass detection (c) Static detection of conformational changes of polymer brushes (d) Detection of molecular recognition (e) Detection of adsorption processes.

Nanomechanical cantilevers are mechanical sensors based on a thin lever which is fixed at one end [24, 138–140]. The cantilever acts as a transducer to respond on tiny changes in surface properties which leads to differences in surface stress at opposite sides of the nanomechanical cantilever and in consequence to a bending (figure 5.58). In this thesis the bending is detected with

the beam deflection principle (see section 2.6). A sensing device consists of the cantilever functionalized with a functional coating which reacts on an external stimuli. Using an array of cantilevers offers the possibility to integrate functionalized and reference cantilevers into one sample, in order to compensate for thermal drift and unspecific absorption.
Nanomechanical Cantilever Sensors (NCS) were used for material characterization of thin films [24] and detection of molecules [141]. Owing to their low spring constant, tiny changes in the swelling of a polymer or changes in surface properties of thin films deposited onto NCS can be monitored [57, 135, 142]. Furthermore, thermally induced effects can be investigated using bimaterial cantilevers such as calorimetry [143, 144], photothermal spectroscopy [145] and micromechanical thermogravimetric analysis [146]. NCS can be readily operated in liquids enabling biotechnological investigations [141] as well as the characterization of polymeric systems in solvents or gases [57,147].

In this thesis two applications to utilize NCS are presented. In the first part thermal responsive polymer layers are prepared on cantilever arrays and the response of the NCS bending as a function of the temperature is discussed. The second part shows the rapid fabrication of a humidity sensor based on polyelectroylte multilayers with inkjet printing.

5.1. Response Characteristics of Thermal Responsive Polymers using Nanomechancial Cantilever Sensors

*

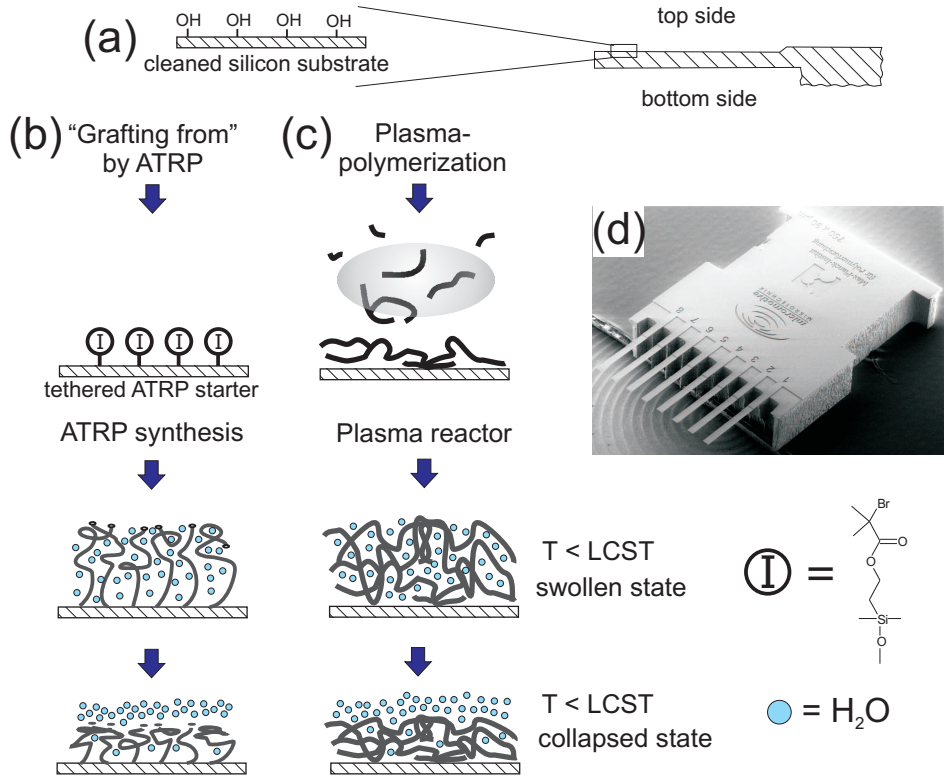

Fig. 5.59.: (a) Cleaned silicon substrate: zoom in and (b) schematic of the deposition procedure for the PNIPAM polymer brush layer and (c) a sketch of the plasma polymerization process on the nanomechanical cantilever surface. Heating induces a coil to globule transition that expels water from the polymer film. In a hydrophilic state, the polymer brush configuration has relatively parallel chains extending into the fluid. In the hydrophobic state, these chains, however, collapse onto themselves. The plasma deposited polymers have a more random configuration including cross linking between the chains. (d) Scanning electron microscopy image of a nanomechanical cantilever sensor array that was used.

5.1.1. Introduction

Stimuli responsive polymers are promising materials for functional surfaces and interfaces covering a wide range of applications from medicine [148] to nanotechnology [149, 150]. Many different response characteristics in these materials are known, for instance, response to pH [147], magnetic field [151] or to temperature [152] changes. Thermally responsive brushes can be used to actuate micromechanical elements and have been used to move nanometer sized objects [153]. Poly(N-isopropylacrylamide) (PNIPAM), poly(N,N-diethylacrylamide) (PDEA), poly(methyl vinyl ether), poly(N-vinylcaprolactam) and synthetic poly(pentapeptide) e.g. (poly(GVGVP) - V for L-valine, G for glycine, and P for L-proline) serve as some of the most commonly known temperature sensitive polymers. PNIPAM is one of the most prominent materials that are currently under investigation as a model system for a thermally responsive polymer. PNIPAM is characterized by its lower critical solution temperature (LCST) of about 32°C at which the material changes its solubility characteristics. Below the LCST, the polymer is solvated in water corresponding to a random coil structure of the polymer chain. Around LCST, however, the intermolecular interactions become favored, and the polymer is dehydrated. As a consequence the polymer chains change their conformation to a dense globular structure. This thermally induced structural phase transition is reversible [154]. For a dissolved stimuli responsive material, the LCST is determined by measuring the cloud point in the solution (turbidimetry). Alternative techniques include static and dynamic light scattering which provide more details about the radius of gyration and the hydrodynamic radius of structures that exist below and above LCST. More insight into the dynamics of the phase transition can be obtained by laser induced temperature jump (T-jump) experiments [155]. However, most of the latter techniques cannot be used routinely to study stimuli responsive materials that are grafted to surfaces. In particular, in the presence of a confinement, e.g., by a hard wall, the polymer chains respond differently owing to a change of interaction to the

*This section is based on the following publication: Bradley, C., Jalili, N., **Nett, S.K.**, Chu, L., Förch, R., Gutmann, J. S., und Berger, R., *Macromolecular Chemistry and Physics* **2009**, *submitted*, Response Characteristics of Thermal Responsive Polymers using Nanomechancial Cantilever Sensors.

next polymer chain neighbors. Typically, thermally responsive surfaces are studied by contact angle measurements [156]. This technique revealed a significant increase in water contact angle of a PNIPAM brush layers at 32°C . Quartz crystal microbalance studies of the coil-to-globule transition in thermosensitive PNIPAM brushes have shown that structural changes take place at a temperature range of 15 - 50°C . In particular, dehydration of the PNIPAM brush layer was observed below and above the LCST [157]. Complementary methods are required to separate temperature induced effects, e.g., thickness, mass, wettability or pressure changes inside thin thermally responsive polymer films.

This section reports on the preparation of thermally responsive polymer coatings on NCS along with the setup utilized to control the temperature for NCS measurements. Exemplarily two different types of thermally responsive polymer systems were investigated; namely, (i) Poly(N-isopropylacrylamide) (PNIPAM, LCST of 32 °C), and (ii) a polymer prepared by a plasma polymerization process of N,N-diethylacrylamide (ppDEA) having a LCST of 38 - 41°C [158].

5.1.2. PNIPAM Brush Layer

Investigations into the reponse of PNIPAM brush layers were performed using NCS array chips that supported 3 cantilevers with a 7 nm thick PNIPAM coating (P1, P2 and P3) and 3 uncoated cantilevers as references (R1, R2 and R3) (Figure 5.59(b)). The fluidic cell was filled with Millipore water while the temperature of the fluidic cell was kept at a constant temperature of 23°C , i.e., slightly above room temperature, by controlling the electrical current in the heating foil and monitoring the temperature via the Pt100 sensor. The entire setup was kept at that temperature for 10 minutes to allow thermal stabilization. Typically a constant deflection (drift < 0.02 nm/s at 23°C) of all NCS was observed independent of the surface coating. The fluidic cell was then heated at a linear temperature ramp of 3°C /min up to a maximum temperature of 50°C . Meanwhile, the deflection data of the three reference NCS (R1 - R3) and the three PNIPAM coated NCS (P1 - P3) were recorded. Upon heating, the averaged deflection of the PNIPAM coated NCS first decreased,

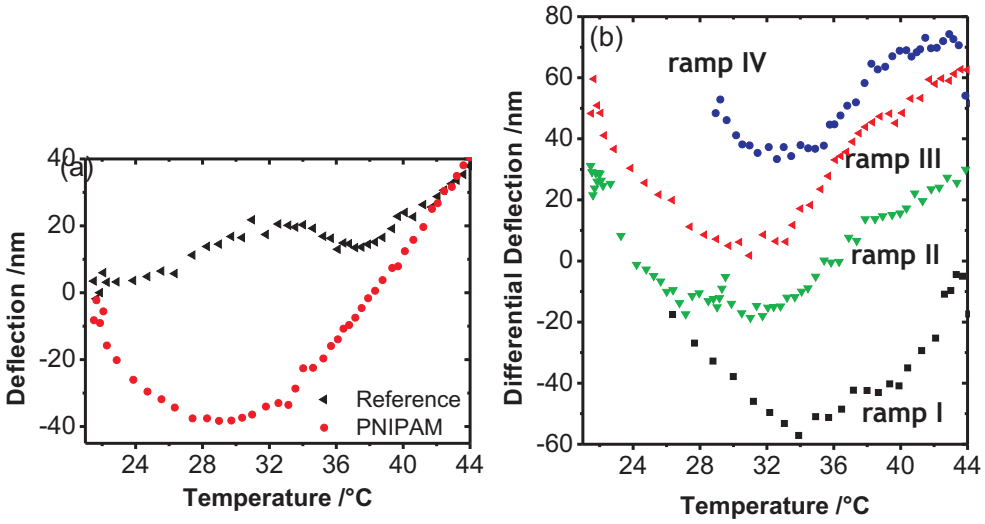

Fig. 5.60.: (a) Average measured deflections of the reference (filled black triangles) and PNIPAM functionalized NCS (red circle) upon heating. (b) Differential deflection between PNIPAM and reference NCS sensors for four subsequent heating ramps.

reaching a minimum deflection value of -40 nm at approx. 29°C . This deflection corresponds to a bending of the NCS towards the PNIPAM coated side. Further heating resulted in an increasing deflection reaching 16 nm at 40°C (Figure 5.60(a), red circle). The reference NCS sensors did not show a clear minimum deflection value. At a temperature of 40°C , a deflection of 23 nm was reached comparable to that of the PNIPAM coated NCS of Figure 5.60(a) (filled black triangles). This deflection change of the reference NCS is attributed to the expansion of the fluidic cell leading to a change in position and/or tilt of the NCS chip. The latter contribution of the fluidic cell upon heating can be compensated by subtracting the reference NCS from the PNIPAM coated signals (see Figure 5.60(b)).

The heating ramp was then repeated four times using the same samples to reproduce and check reversibility of the response of the PNIPAM brush coated NCS (Figure 5.60(b)). In all ramps, we found a clear minimum between 29 - 34°C of the differential deflection. This temperature range is in agreement with the expected lower critical solution temperature of PNIPAM, i.e. 32°C as determined by cloud point measurements [154].

Discussion

The effect of the LCST occurs when it becomes thermodynamically more favorable to break the H-bonding between the water molecules and the polymer chains and to form predominately H-bonding between the carbonyl group (C=O) and the amine groups (N-H) of the PNIPAM polymer. This leads to continuous dehydration, although still below LCST, and a collapse of the polymer film. The dehydration of the PNIPAM layer is associated with a decrease in volume of the PNIPAM layer. As the PNIPAM chains are entangled [159,160], the decrease in volume results in a reduced pressure inside the PNIPAM layer causing the cantilever to bend towards the PNIPAM layer side (temperature $< 30°$C in Figure 5.60). Upon further heating the fluidic cell towards LCST, the water inside the PNIPAM layer is expelled almost completely, thereby the deflection towards the PNIPAM side is expected to saturate. Heating above the LCST leads to a collapse of the PNIPAM and a denser film is formed. Tagit and co-authors have reported an elastic modulus for dry PNIPAM micro-gel spheres in water below the volume phase transition temperature (VPTT) of 1.8 $\pm$ 0.2 MPa. Above the VPTT in water, the elastic modulus of the spheres increases by an order of magnitude to 12.8 $\pm$ 3.6 MPa [161]. Thus, upon dehydration the cross-linked particles became stiffer. Kujawa and co-authors determined the temperature dependence of the expansion coefficient of PNIPAM in water giving values of 0.76×10^{-3} K^{-1} (at 10°C) and 1.28×10^{-3} K^{-1} (at 50°C) [162]. Assuming these values for the PNIPAM brush layer used here as a coarse approximation, the temperature induced deflection d of the NCS can be calculated associated to the bimaterial effect by

$$d = \frac{3L^2}{4} \frac{(t_{Si} + t_{po}) \cdot \Delta\alpha \cdot \Delta T}{\frac{7}{4}(t_{Si} + t_{po})^2 - 2t_{Si}t_{po} + \left(\frac{E_{Si}t_{Si}^3}{E_{po}t_{po}}\right) + \left(\frac{E_{po}t_{po}^3}{E_{Si}t_{Si}}\right)} \tag{5.1}$$

where $\Delta\alpha$ corresponds to the difference in the expansion coefficient of silicon and the polymer layer ($\Delta\alpha_{Si} - \Delta\alpha_{po}$). L is the cantilever length, t_{Si}, t_{po} are the thickness, E_{Si}, E_{po} the Young's modulus of the silicon cantilever and the polymer, respectively [163]. Ellipsometry revealed a dry film thickness of

7 nm which corresponds to a film thickness of $d_{water,22°C} = 45.5$ nm (< LCST) and of$d_{water,34°C} = 21$ nm (> LCST) [164]. Using these values, a deflection was calculated of 0.2 nm per °C at temperatures below LCST. Above LCST, a deflection was obtained of 0.9 nm per °C . Fitting a line to the measured temperature deflection data above 32°C of figure 5.60(b) revealed significant higher slopes (3.3 nm/°C - 4.8 nm/°C). Thus, the bimaterial effect is not the dominating factor above LCST which leads to a deflection of the NCS. One potential further contribution would be that the PNIPAM chains collapse into a non-equilibrium state that can slowly relax in time or upon further heating. Alternatively, the pressure inside the collapsed film might be released by polymer chains that untangle owing to the mechanical stress of the bent NCS. Such unentanglements were assumed also by Ruths and co-authors who have observed a decrease in repulsive force of a polymer brush layer in surface force apparatus measurements in time [160]. To find out if unentanglement plays a significant role in these measurements, a thermally responsive polymer layer was investigated in the following section that is cross-linked and thus unable to exhibit unentanglement.

5.1.3. Plasma Deposited Polymer (ppDEA)

For reference measurements of a thermally responsive coating were made that was deposited using plasma polymerization. This system was found to have a LCST ranging from 38 - 41°C as determined by contact angle measurements [158]. In contrast to the polymers that are end-grafted to the NCS surface, plasma deposited polymers are composed of interlinked chains that are probably bonded to the substrate at several sites on the network (Figure 5.59(c)). A 187 nm thick film was deposited on a 3.53 μm thick cantilevers sensor. Then, the NCS chip was placed in the fluidic cell and heated at a similar rate as used for the PNIPAM brush layer (heating rate 3°C / min) previously. The ppDEA showed a similar response to that of the PNIPAM coated NCS, i.e. a deflection towards the polymer coating at temperatures < LCST. At higher temperature, the deflection was reversed, i.e., away from the polymer coating (fig. 5.61 (a)). Repeating the heating cycle a 2nd and 3rd time revealed qualitatively similar responses. Repetitive heating/ cool-

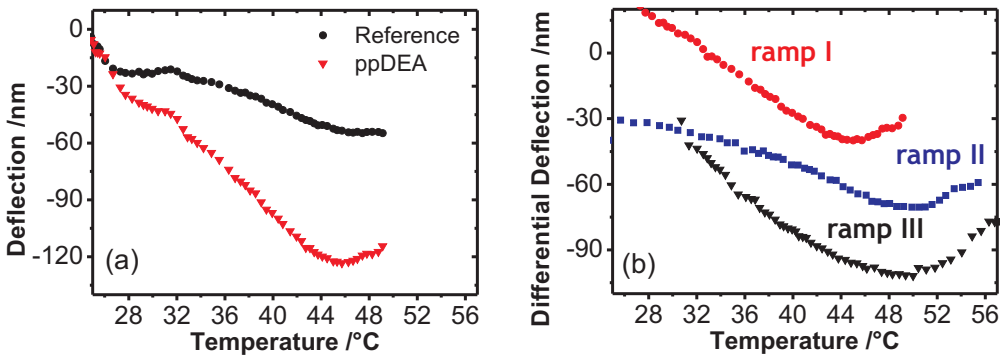

Fig. 5.61.: (a) Average measured deflections of the reference and ppDEA functionalized NCS upon heating. (b) Differential deflection between ppDEA and reference NCS sensors for three subsequent heating ramps.

ing cycles resulted in a decrease in the measured deflection signal which is attributed to washing away some of the polymer material from the surface due to less covalent binding between the ppDEA and the SiOx surface. This effect is typical for plasma deposited layers that were deposited directly to a Si substrate and could be avoided by using self-assembled monolayers (SAM) of dodecanethiol on gold. Upon deposition of the plasma polymer on such a surface the carbon-carbon-bonds of the dodecanthiol layer are broken and chains deposited from the plasma are linked to the dangling bonds [165]. Measurements on Au and SAM coated NCS revealed a significant deflection of the cantilever of -103.5 nm/°C $\pm$ 10 nm/°C owing to the bimaterial effect between the Au coating and the Si. This deflection magnitude superimposed every other effect of the thermally sensitive polymer film as discussed above. Based on equation 5.1 the bimaterial induced deflection was determined upon heating of the Si cantilever coated with pp(DEA) corresponding to 0.002 nm/°C for temperature below the LCST and 0.031 nm/°C for temperatures above the LCST. For this calculation the elastic modulus E for plasma deposited NIPAM was assumed to be similar to the one of pp(DEA). In the literature [166] E_{ppDEA} is reported to be 0.185 MPa at 25°C and 1.592 MPa at 37°C . However, a linear fit of the differential deflection above the LCST revealed a slope of 2.3 to 4.5 nm/°C which is again significantly higher than the deflection determined from the bimaterial effect. Since in cross linked polymers unen-

tanglement is hampered it can be concluded that the deflection of the NCS above LCST can be mainly associated to relaxation processes of the polymer films.

5.1.4. Surface Stress

To obtain values independent on the used NCS parameters the change in surface stress $\Delta\sigma$ was calculated according to Stoney's formula with the approximation made by Atkinson [167]

$$\Delta\sigma = \frac{E_{Si} t_s^3 \Delta x}{3l^2 t_c^2 \left(1 + \frac{t_s}{t_c}\right)(1-\nu)} \tag{5.2}$$

E_{Si} is the elastic modulus of silicon ($E_{Si} = 1.7\times10^{11}$ N/m^2),ν is the Poison ratio ($\nu = 0.24$), t_s is the thickness of the cantilever, t_c is the thickness of the coating, l is the length of the cantilever and x the deflection of the cantilever. However, the thickness of the thermally responsive coating is dependent on the temperature. Therefore, the minima were selected in the measured differential deflection for comparison of PNIPAM brush and ppDEA layers. At this temperature it is assume that the polymer layers are almost completely collapsed. For the PNIPAM brush layer, a surface stress change was obtained of 2.57×10^5 N/m^2 $\pm$ 8.8×10^4 N/m^2 (average deflection x = 41.7 nm $\pm$ 14.3 nm and t_c = 21 nm film thickness). For the plasma polymer, Chu et al. reported only minor decrease in thickness of about 9 nm for a 163 nm swollen pp(DEA) layer [158]. Thus, the differential surface stress change for the ppDEA was determined to be 8.1×10^5 N/m^2 $\pm$ 3.7×10^5 N/m^2 (average differential deflection x = 43.5 nm $\pm$ 20.0 nm and t_c = 187 nm film thickness) being 3 times larger in magnitude compared to the PNIPAM brush layer.

5.1.5. Determination of LCST

These measurements do not show a sharp transition at the LCST. For an estimation of the LCST, the minimum was determined of the differential deflection by fitting a polynomial in the temperature range of 28°C and 35°C (PNIPAM) and 42°C and 53°C for (ppDEA). The mean values of all minima

correspond to 31.9 $\pm$ 1.7°C (PNIPAM) and 47.7°C $\pm$ 1.9°C (ppDEA). The measured LCST of PNIPAM grafted to the NMC surface is thus very close to the LCST found for the bulk polymer.

5.1.6. Summary and Conclusion

Nanomechanical cantilever sensors (NCS) were used to investigate the thermal response of a 7 nm thick PNIPAM polymer brush and a 187 nm thick ppDEA layer made from a plasma polymerization process of N,N-diethylacrylamide. In particular, an experimental procedure was developed to cover one side of a NCS with a covalently bound thermally responsive polymer brush layer. The NCS deflection showed two different regimes: At temperatures $<$ LCST the deflection was dominated by dehydration, and at temperatures $>$ LCST the NMC responds mainly to slow relaxation processes of the collapsed polymer layers. Such a relaxation was found for the PNIPAM polymer brush layer as well as for the interlinked ppDEA film. For all temperatures investigated, the bimaterial effect is only a minor contribution to the measured NCS deflection. It was found that the minima in the differential deflection of NCS are in agreement with the LCST of the selected polymer, respectively. Finally, the thermally induced transduction of a bending to a cantilever was found to be higher for the cross linked plasma polymers. The applied NCS method has advantages in terms of running a continuous temperature ramp at different speed, e.g. 0.1°C /min - 10°C /min. Therefore, information about the LCST of ultra thin thermal responsive polymer films can be obtained rather quickly. The heating rate is currently limited by the temperature control system and not by the response times of NCS in liquids which are typically in the milliseconds regime [26]. Thus, data can be obtained continuously and limitations arising from stepwise temperature measurements, e.g., by ellipsometry or contact angle method do not exist. Furthermore, the NCS method can be readily used in a wide temperature range even close to the boiling point of water. In addition, only small areas (μm^2) which are covered by the thermal responsive polymer are required to obtain valuable information on thermally responsive polymers. Consequently, the size of the reactor and the amount of materials that is used for the synthesis

can be reduced significantly.

5.2. Humidity Sensor Based on Polyelectrolyte Multilayers

As another potential application for nanomechanical cantilever sensors (NCS) is the use of polyelectrolyte multilayers for functional coating to build up a humidity sensor demonstrated. Based on the results shown in section 4.2 polyelectrolytes are exclusive materials to form homogeneous and stable films using inkjet printing. Single sided coating is achieved by this procedure which is important to get a surface stress to induce cantilever bending.
Previous experiments from Yu et al. [168] build a humidity sensor from PEM. In this study the humidity was monitored as a function of absorbance of the PEM film. Another humidity sensor reported by Lv et al. [169] was created from conjugated polyelectrolytes which change their impedance upon the surrounding humidity.
The approach in this chapter employs the same PEM system $(PAH/PSS)_n$ described in section 4.2. PAH and PSS offer several advantages in comparison to conjugated polyelectrolytes. They do not require complex synthesis steps. Therefore, they are easily accessible and relatively cheap. For PAH/PSS multilayers is reported that the film swells upon exposure to water vapor [111, 170]. Wong et al. found an increase in thickness by a factor of 1.5 from 3% to 99% humidity for a 116Å PAH/PSS film consisting of 5 bilayers. Also, they reported a dependency on the covering layer. PSS as a toplayer shows a significant higher swelling ratio compared to a PAH toplayer. Losche et al. demonstrated with neutron reflectivity that the water uptake is greater than or equal to 40% of the volume of the films at 100% humidity [111]. Additionally the E-modulus of PEM films decreases with increasing water uptake [171]. These physical properties are ideal for sensing applications with NCS. The nanomechanical cantilever acts as transducer to detect the swelling ratio of a PEM with high precision and time resolution [26].
In this section inkjet printing is discussed to prepare PEM films for quick and selective single sided coating of the cantilevers. The resulting cantilever ar-

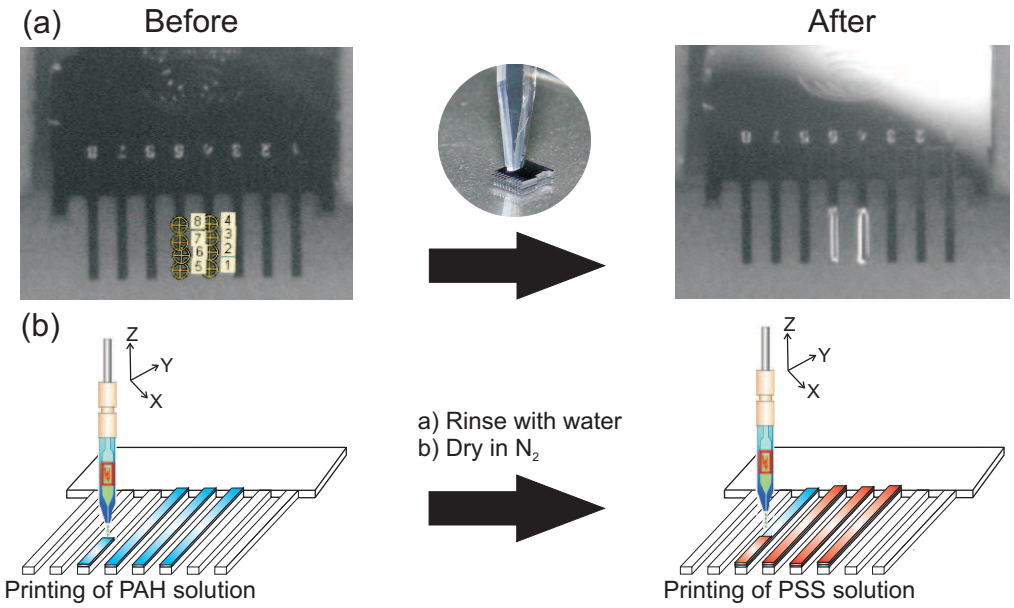

Fig. 5.62.: Inkjet printing of PE solution on individual cantilevers. (a) Before spot printing: On cantilever C4 and C5 four drop positions are marked manually indicated by the yellow crosshairs. After spot printing: The cantilevers are covered with liquid completely. (b) Sketch of the LbL process. First PAH is printed on the cantilevers. After washing and drying PSS is printed.

ray was exposed to water vapor and the deflection signal and the resonance frequency shift were recorded.

5.2.1. Coating of Individual Cantilevers with PEM

The NCS chips used for this study had a width of 90 μm, a pitch of 250 μm, a length of 500 μm and a thickness of 3.6 μm. The first resonance frequency was 19837 $\pm$ 37 Hz with a calculated spring constant of 1.40 $\pm$ 0.01 N/m (see section 2.6). In order to coat the cantilevers in a LbL process, first four drops of PAH solution were plotted by video assisted drop positioning onto the top-side of NCS within five seconds (fig. 5.62 (a)). Then, the next NCS was addressed and coated (fig. 5.62 (b)). After rinsing for 15 seconds with water, the NCS array was dried in a stream of nitrogen. Then, the next oppositely charged polyelectrolyte PSS was plotted on the NCS (fig. 5.62 (b)). In contrast to silicon wafers the NCS array is very fragile. Therefore, the print process was modified so that the washing step and drying step were done

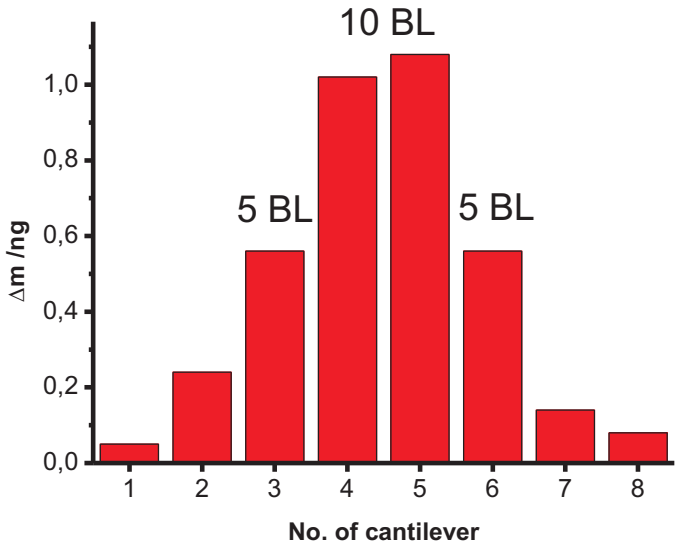

Fig. 5.63.: Mass change of individual cantilevers after coating with PEM. Cantilever C4 and C5 are coated with 10 BLs of PAH/PSS and C3 and C6 are coated with 5 BLs.

manually in order not to break the cantilevers. The chip was glued onto a special holder [50] to assure that the NCS chip stays at the same position for the whole procedure. Cantilevers C3 to C6 were coated with 5 BLs and cantilevers C4 and C5 were coated with another 5 BLs subsequently resulting in 10 BLs in total. A salt concentration of 0.1 mol/L NaCl was chosen.
The quality of the process was monitored by measuring the shift of the resonance frequency due to the increased mass. The shifts in resonance frequency for humidity dependence were detected with the second resonance mode at initially 123.4 $\pm$ 0.1 kHz, which is more effective at higher angles of light reflection. For calculation equation 2.27 was used.
Since the ratio between 5 and 10 BLs is a factor of 2, this is reflected nicely in the mass increase of 0.55 ng and 1.08 ng for 5 and 10 BLs coated cantilevers respectively (see diagram 5.63). Furthermore the change in mass is for both 10 BL and 5 BL cantilevers in well agreement. The cantilevers which have not been covered with PE solution show an average mass increase of 0.13 $\pm$ 0.08 ng. This can be explained by undefined adsorption of molecules during the washing step. In the subsequent experiments it is shown that the reference cantilevers do not respond on exposure to water vapor. So, the undefined

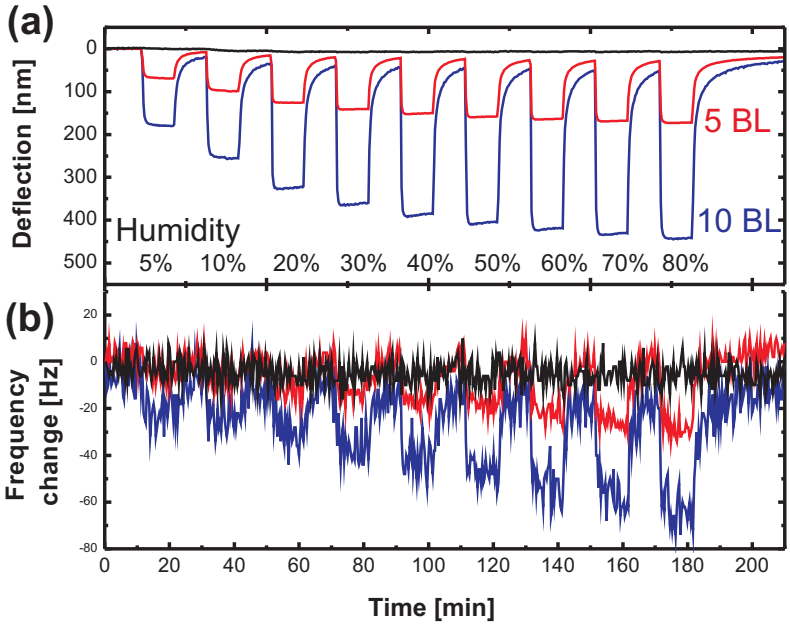

Fig. 5.64.: (a) Deflection response and (b) frequency change as a function of the time on humidity change from 5 to 80 %.

adsorption occurs on both the bottom and the top side which results in equal surface stress and consequently no bending is observed.

5.2.2. NCS Response to Humidity

In order to see if the PEM coated NCS is practicable as humidity sensor the environmental cell was connected to a gas flow system (see appendix C.2). With this system it is possible to provide a constant flow of nitrogen (0.5 mL/min) containing a defined amount of water vapor. The humidity was set to a certain value to equilibrate for 10 min and then it was switched to dry nitrogen for another 10 min. This was done for a series of 5, 10, 20, 30, 40, 50, 60, 70 and 80% humidity. The response on the cantilever was measured by the beam deflection principle. Simultaneously, the resonance frequency was monitored to analyze the mass increase due to the diffusion of water molecules into the polymer film.

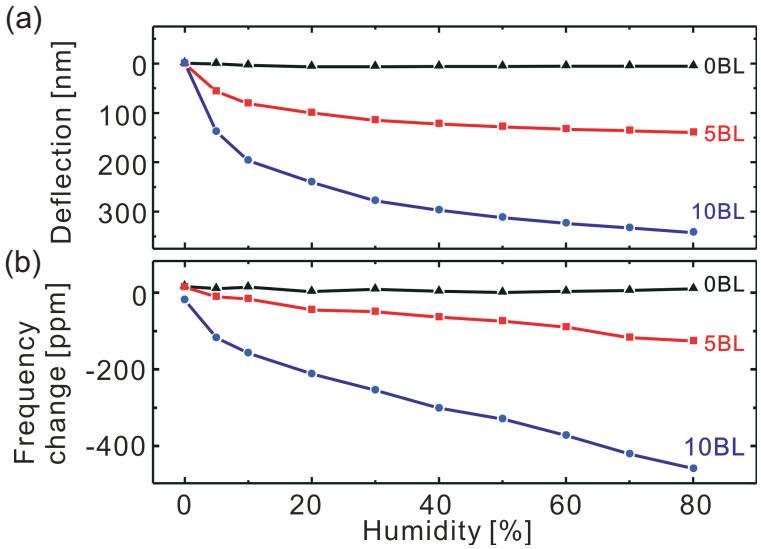

Fig. 5.65.: (a) Averaged deflection response and (b) frequency change as a function of the humidity.

The graph 5.64 displays the experimental results in the deflection response and the resonance frequency shift upon the humidity change. For the PEM coated cantilevers the deflection shows a steplike increase when the humidity is set to the next higher value i.e. the cantilevers bend away from the coated side. When polyelectrolyte multilayers are exposed to water vapor then the water diffuses into the polymer network and consequently swells it. The surface stress results into a positive bending away from the coating. The response takes around 21 s. While the humidity stays constant for 10 min the deflection does not change more than 5 nm. When the gas flow is changed to nitrogen, then the reversal process is observed. The nitrogen stream dries the PEM and the cantilever moves back in the direction of its initial position. However, this process is much slower and is supposed to be finished after 10 min, whereas the initial deflection value is not reached exactly, but the value is always below 19% of the respective saturated deflection. In dry nitrogen the water diffuses from inside the film into the gas phase and the cantilever relaxes back. Due to the high polarity of the water molecules the adsorption and diffusion into the polymer network is preferred in comparison to the diffusion out of the film into the dry nitrogen. Therefore the relaxation process is slowed down.

The reference cantilevers do bend a maximum of 6 nm for the whole experiment which is negligible compared to the maximum of 442 nm for 10 BLs in 80% humidity. Generally the result is an evidence of an optimal single-sided coating, since the swelling of PEM on both sides of the cantilevers would cancel each other out and consequently the surface stress would be equal on both sides of the cantilever.
The measurement of the resonance frequency shift is very noisy (see figure 5.64 (b)). Therefore the resonance frequency shift could be determined in humid environment by averaging the resonance frequency shifts in the time period where constant deflection was recorded (see fig. 5.65 (b)). For comparison the same presentation was chosen for the deflection data (see fig. 5.65 (a)). The dynamic measurements show a mass increase upon exposure to water vapor. This is consistent with the theory of swelling and the higher the humidity the higher is the corresponding mass change.
In 80% humidity 0.35 ng $\pm$ 0.04 ng and 0.20 ng $\pm$ 0.02 ng water diffuses into the polymer film consisting of 10 BLs and 5 BLs respectively (fig. 5.66). This is a relative mass uptake in average of 35% $\pm$ 2% which is in accordance to the reported mass uptake of 40% in 100% humidity [111]. The deflection of the NCS after exposure to humidity increased with increasing humidity. Remarkably the bending of the 10 BLs is more pronounced, by a factor of 2.6 for all set humidities, in comparison to the bending of the 5 BLs. In order to present the deflection data independent from the cantilever geometry the surface stress was calculated according to Stoney's equation [172]:

$$\sigma = \frac{Eh^2}{3L^2(1-\nu)} \cdot |\delta| \tag{5.3}$$

Herein σ is the surface stress, E is the Young's modulus for Si (E_{Si} = 170 GPa), L is the effective length of cantilevers (L = 500 μm), ν is the Poisson's ratio of Si (ν_{Si} = 0.23), h is the thickness of the cantilevers (h = 3.6 μm), and $|\delta|$ is the absolute deflection at the end of the cantilever. From this presentation can be concluded that thicker PEM leads to more surface stress changes than thinner PEM since the difference of the ratio between the averaged deflection is 2.6 and the averaged mass difference is 1.77 between five and ten bilayer on NCS after swelling (fig. 5.66). The characteristics of the deflec-

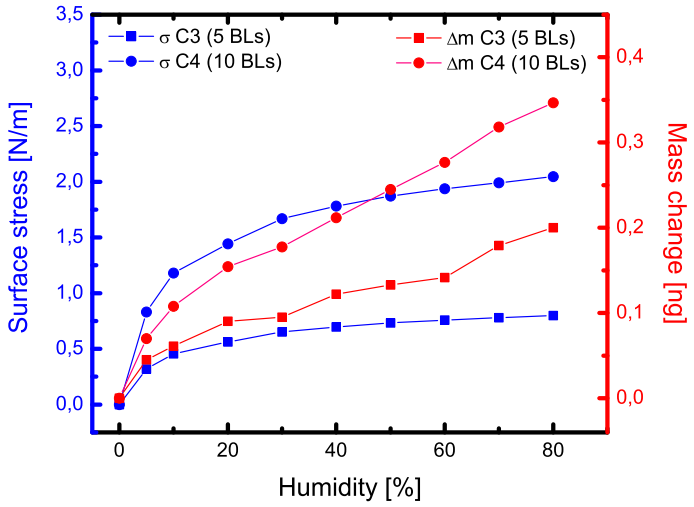

Fig. 5.66.: Left axis (blue): surface stress for the cantilevers C3 (5 BLs) and C4 (10 BLs) as a function of the humidity calculated with Stoney's equation. Right axis (red): mass change for these cantilevers as a function of the humidity.

tion curve and the mass change curve are different upon increasing humidity. Both increase continuously but from about 10% humidity the deflection levels off while the mass increases almost linearly. The elastic property of the film changes with higher water content i.e. the Young's modulus decreases with increasing humidity [171, 173]. Basically, the polymer layer is softened because water decreases the interactions between the polymerchains and a lower force is needed to deform macroscopically the swollen polyelectrolyte multilayer structure.

Summary and Conclusion

The fabrication of functional coatings based on the LbL process is a quick and robust method to get a nanomechanical cantilever sensor system. Here, it took about 120 s to prepare 1 BL of PAH/PSS on 4 cantilevers. It was proven that the inkjet printing resulted in a selective single sided coating of the cantilever with high reproducibility. For this procedure a few nL of PE solution were sufficient to prepare the sample. A clear response in deflection and mass change was observed on exposure to a defined humidity. The response was within

21 s and changes of 10% humidity were detected sensitively. The deflection signal of 10 BLs was 2.6 times higher compared to 5 BLs while the mass increased by a factor of 1.77 between 5 to 10 BLs. This was attributed to a higher stiffness of the the thinner polyelectrolyte multilayers. Furthermore, the films became softer when the surrounding humidity was higher. The Young's modulus of the film could be calculated using the bimaterial formula (see eq. 5.1). However, an exact expansion coefficient for the here reported PAH/PSS system is not readily available. For further studies of the Young' modulus the expansion coefficient needs to be determined using complementary methods e.g. in situ ellipsometry or x-ray reflectivity.

6. μ-GISAXS for Nanomechanical Cantilever Analysis

6.1. Introduction to μ-GISAXS

Generally GISAXS (section 2.3) is a versatile method to study the structural properties of thin films. Since it requires high intensity flux of photons synchrotron sources are needed, especially for the investigation of polymeric samples. For example the ESRF (European Synchrotron Radiation Facility, Grenoble France), CHESS (Cornell High Synchrotron Source, Ithaca USA) or HASYLAB (Hamburger Synchrotron Labor, Hamburg Germany) offer beamlines to study thin films in grazing incidence geometry. In recent years these beamlines got upgrades to have focused x-ray beams [45, 174].
Early μ-GISAXS experiments were performed by S.V. Roth et.al. [175, 176]. They investigated films of self assembled gold clusters placed on top of 40 nm poly(styrene) with an one-dimensional gradient in cluster height. With the use of a 5 μm x-ray beam in grazing incidence geometry slices were measured in the direction of the gradient, so that it was possible to get the cluster height, structure and morphology as a function of the beam position. Additionally, the microbeam setup gave an increase of two orders of magnitude in spatial resolution compared to conventional GISAXS experiments [177]. Müller-Buschbaum, et al. probed local defects in polymer blend films [178] at the ID13 beamline (ESRF, Grenoble). With a x-ray beam of 0.9 μm diameter microcracks were locally resolved.
The beamline BW4 in Hamburg at the HASYLAB upgraded also their setup [44] to focus the x-ray beam (see section 2.3.1). A set of beryllium lenses as an additional optical element focuses the beam which has originally a dimen-

sion of 400 x 400 μm^2 down to a size of 65 x 35 μm^2 or 30 x 17 μm^2 (Vertical x horizontal) depending on the number of lenses.
In the experiments explained above the microsized beam was mainly used to locally resolve structural properties on large samples. However, the small beam size also allows to study samples with a limited size (see figure 6.67). The prominent micro fabricated objects like microelectromechanical systems (MEMS) [17] are now accessible to x-ray studies in order to determine surface coatings and structures. In chapter 5 nanomechanical cantilever sensors are introduced as an application to detect the lower critical solution temperature of poly(N-Isopropylacrylamide) and as a humidity sensor based on PAH/PSS polyelectrolyte multilayers. The system is build of a microcantilever which is covered single sided with a polymer brush. The used silicon microarrays (OCTOSENSIS from Micromotive, Germany) consist of eight rectangular cantilevers with a length of 750 μm, width of 90 μm and thickness of 1, 2 or 5 μm arranged at a pitch of 250 μm (see figure 5.58). So the geometric width of the cantilever is three times bigger than the horizontal beam size. Therefore one should be able to apply x-ray scattering in reflection geometry to the microcantilever array. In previous studies, Wolkenhauer et al. [179], showed that the single cantilevers of the array could be addressed separately. The intensity of the material dependent Yoneda peak was utilized to distinguish between gold and polymer coated cantilevers.
The quality of the sensing system is depending on the properties of the coating. Therefore the analysis of the layer coating is crucial. This chapter presents the results on the new developed method of μ-reflectivity and μ-GISAXS measurements performed at the beamline BW4 at the HASYLAB. Two systems are investigated in detail: (i) PMMA brushes on NCS (ii) PEM line structure containing gold-nanoparticles.

6.2. Construction of μ-Reflectivity Curves

Experimentally reflectivity curves are obtained by measuring the specular intensity for a series of angles α_i in the range 0.1 to 1.8 °. At the synchrotron beamline BW4 (2.3.1) a 2D-CCD detector records the scattered intensity. This

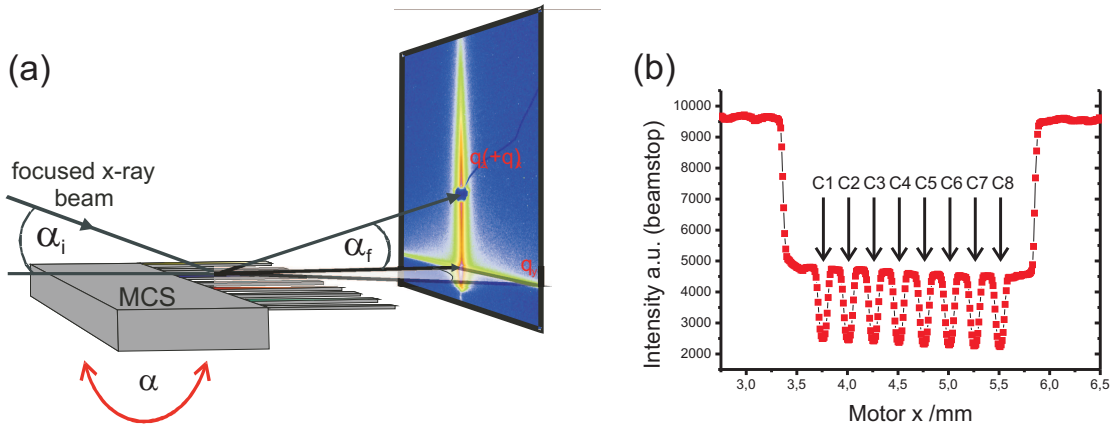

Fig. 6.67.: (a) Schematic drawing of the scattering geometry on a nanomechanical cantilever array. (b) Intensity taken from the primary beamstop while scanning a nanomechanical cantilever arry in x direction at an incident angle of 0.7°. The individual cantilevers C1 to C8 block the intensity.

means for every angle exists one detector image which has to be evaluated for the specular intensity. The detector area is geometrically limiting the highest incident angle α_i to 1.8 °. Several steps have to be accomplished for the evaluation which is automated by a analysis script written in the programming language Python (see appendix B.6) [180,181]. Hence the individual steps are explained in detail.

In order to use the optimum of the dynamic detector range the whole angular range will be divided in smaller sections with increasing acquisition time. The effective photon intensity is recorded by an ionic chamber located in front of the sample. This is saved for the whole angular range α_1 - α_n in one data file. Then, the analysis script reads in the data file and sequentially the detector images are accessed. Each image is normalized to the effective photon intensity. Afterwards, a detector scan is performed i.e. a vertical slice is cut at $\Psi = 0$ or $q_y = 0$. Figure 6.68 illustrates the cuts for a few selected angles. Finally, the specular intensity can be determined in two ways: a) A Gaussian profile is fitted at the α_i / q_z position of the specular peak. The amplitude corresponds to the specular intensity. b) An interval around the maximum of the specular peak is summed up. Thereafter, the angle α_i and the corresponding Gaussian amplitude and specular intensity is written to the data file. These steps are performed for all angular ranges.

Especially close to the critical angle the intensity is very high and even with the usage of an absorber the acquisition time is very low. This may lead to errors counting the correct photon intensity in the ionization chamber. Thus, normalization of this angular range is often wrong. Therefore the specular intensity has to be corrected manually for this angle regime to fit the following angles.

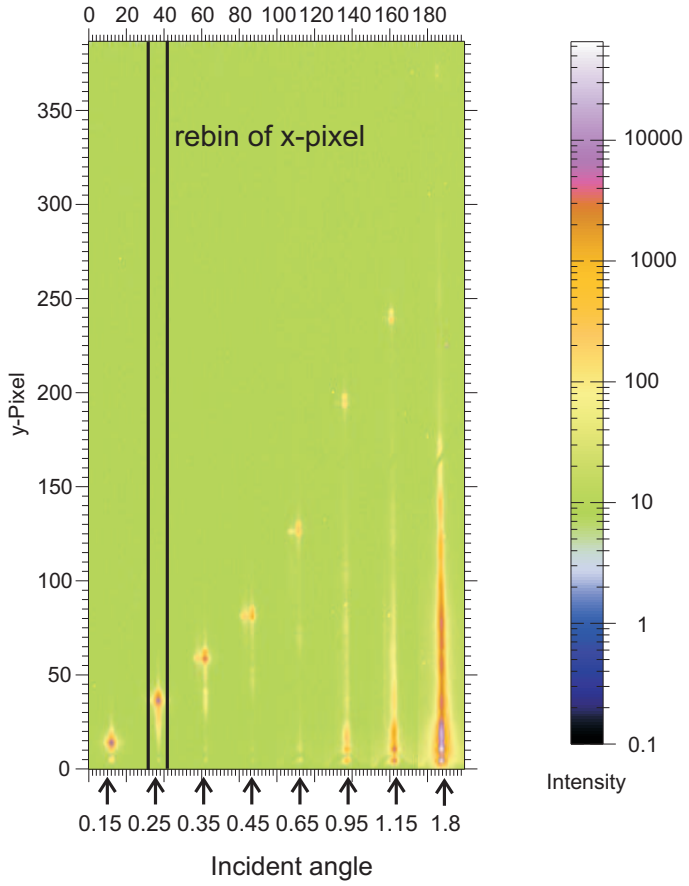

Fig. 6.68.: For a series of incidence angles α_i the cut of the detector image in q_z-direction is shown. To get the specular intensity for every angle the pixels were summed up in q_y direction and the intesity of the specular peak is either fitted by a Gauss-function or the sum a box wih maximum 20 pixels is summed up.

In summary the reflectivity curve is obtained by the following steps:

- Normalization of the 2D-detector image
- Cut of a vertical slice at $q_z = 0$

- Rebin of this cut (In general called "Detector Scan")
- a) Fit of a Gaussian function to the specular peak
- b) Sum up of the intensity in an interval around the specular peak
- Writing a data file with the angle α_i as x axis and the intensity a) and b) as y axis
- Transition from the angle α_i to the wave vector q_z
- Analysis of the reflectivity curve: a) Fit with the Parrat formalism b) Determination of Δq_z for the Kiessig fringes

Analysis is done by applying a fit with the Parrat formalism and calculation of the differential between the minma of the Kiessig fringes. The thickness is then $d = \Delta q_z / 2\pi$

6.3. Poly(methyl methacrylate) Brushes on Nanomechanical Cantilever Sensors

In order to check the quality of the analysis method an experienced synthesis procedure of PMMA brush was chosen [57, 142]. A microcantilever array was partially coated with PMMA brushes according to the following steps (see experimental 7.3, 7.4, and 7.6): First, the complete backside of the chip was coated with a gold layer by evaporation. In order to have covered and uncovered PMMA cantilevers the topside of the cantilever array was coated partially with gold. In the next step the free silicon surface was functionalized with ATRP initiator. The PMMA brush was grafted from the functionalized surface using atom transfer radical polymerization. In the end the gold layer was removed with aqueous KI/I_2 solution. The NCS used in this study had a length of 500 μm, a width of 90 μm and a thickness of 2 μm. From the synthesis of the probed NCS array a bulk polymer was obtained having a molecular

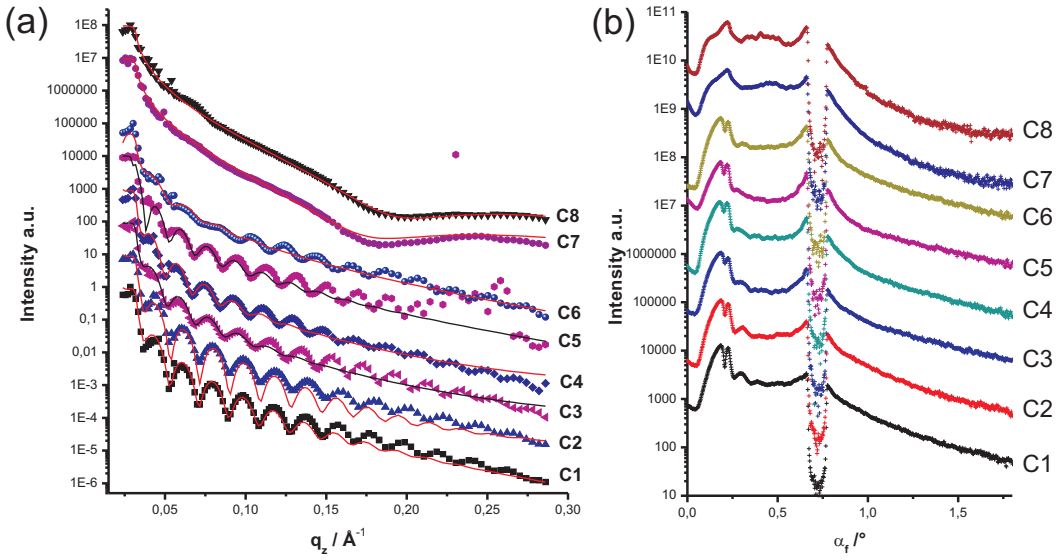

Fig. 6.69.: (a)μ-Reflectivity curves obtained for one NCS array bearing cantilever C1 to C8. A clear pattern is observed for all cantilevers. The red solid line indicates the fits using the Parratt formalism. (b) Detector scan of a static μ-GISAXS measurement at an incident angle $\alpha_i = 0.7°$. For cantilever C1 to C6 the material dependent Yoneda peak is split into two distinct peaks. All curves are shifted by a factor of 100 for clarity.

weight M_n of 80618 g/mol and a polydispersity index D of 1.25. The such prepared samples were taken to the beamline BW4 at the HASYLAB to conduct μ-reflectivity and μ-GISAXS experiments.

After alignment of the chip the x-position of the single cantilevers is determined by a scan in x-direction at an incident angle of 0.7° while recording the intensity on the primary beamstop (see fig. 6.67 (b)). A cantilever blocks the primary beam and this reduces the intensity significantly. The distance between the intensity minima is 250 μm which is exactly the pitch of the cantilevers. Thus, this arrangement is suitable to identify the x-positions. At these positions μ-reflectivity measurements were performed according to the procedure described in section 6.2. The resulting curves are presented in 6.69 (a).

Qualitatively, it can be distinguished between the cantilevers C1 to C5, the cantilever C6 and and the last two cantilevers C7 to C8. The reflectivity curves

for C1 to C5 show a very similar Kiessig fringes pattern. Analysis of the pattern gives brush thicknesses between 329 to 352 Å (see table 6.1). The fitted results for the roughness are around 20 Å which is much higher than the substrate roughness of 3 Å.
Cantilever C6 does not have the same Kiessig fringe pattern. In the q range from 0.05 $Å^{-1}$ to 0.1 $Å^{-1}$ there is almost no pattern. This cantilever is located between the former gold covered cantilevers (C7 and C8) and non gold covered cantilevers (C1 to C5). When the shadow mask is not adjusted correctly, then some gold is also evaporated onto the neighboring cantilever, in this case C6. This observation is similar to the one made by Wolkenauer et al. [179]. The cantilevers C7 and C8 have a layer of around 16 Å to 18 Å on top of the substrate which is most likely silicon oxide and some contaminations of the masking procedure.
A key parameter for polymer brushes is the grafting density which gives a number of polymer chains grafted to a surface. Using equation 3.1 results in an average grafting density Γ of 0.5 μmol/m^2 (see table 6.1). This indicates a dense PMMA brush.
The corresponding ellipsometric data were obtained by measuring the cantilevers at an incidence angle of AOI = 50° and a wavelength of λ = 403 nm. Silicon has a wavelength dependent transparency. At the laser wavelength λ = 632 nm (EP^3 device, Nanofilm) the beam enters the material up to 3 μm i.e. the beam penetrates through the whole cantilever which has a thickness of 2 μm. When the wavelength is reduced to the lowest available wavelength λ = 403 nm of the additional xenon lamp, the beam enters the material less than 0.5 μm. The thickness values are in average 26 Å higher than the values measured by the μ-reflectivity which is a deviation of ∼7% of the total thickness (see table 6.1).
Additionally, static μ-GISAXS measurements were performed at an incidence angle of 0.7°. From the CCD images detector scans at $q_y = 0$ are taken (fig. 6.69 (b)). The material dependent Yoneda peak for C1 to C6 splits into two distinct peaks at 0.185° caused by the polymer brush and 0.22° caused by the silicon substrate. This proofs that the probed NCS C1 to C6 are coated by a polymer brush while C7 and C8 are not covered by a polymer layer.
Remarkably, in the angular regime between the Yoneda peak and the spec-

Table 6.1.: Data of the μ-reflectivity measurements and ellipsometric measurements for the cantilever (NC) C1 to C8. Here is d_{xray} the brush thickness measured by x-ray reflectivity, σ the roughness, Γ the grafting density, d_{corr} the distance between the correlated layer interfaces and d_{elli} the thickness obtained by ellipsometry.

NC	d /Å	σ /Å	Γ /μmol/m^2	d_{corr} /Å	d_{elli} /Å
C1	329	16	0,49	380	360
C2	332	22	0,49	380	360
C3	345	20	0,51	334	361
C4	352	20	0,52	402	374
C5	345	18	0,51	–	393
C6	300	23	0,44	477	312
C7	18	4	–	–	27
C8	16	5	–	–	30

ular peak a pattern is observed. The maxima are Bragg reflexes caused by correlation of the substrate/sample interface and the sample/air interface i.e. that the microscopic roughness on the substrate is replicated by the polymer layer at a distance d [182, 183]. Analysis of the Bragg reflexes results in a distance between the correlated interfaces d_{corr} (see table 6.1) which is similar to the film thickness d. Due to the overlay of specular scattered intensity with the diffuse scattered intensity caused by the correlated roughness, the decay in intensity can not be modeled anymore by the simple Parratt formalism. Therefore, the obtained roughness values σ can not be taken into account and the result of the reflectivity experiments is restricted to the determination of the layer thickness.

Summary and Conclusion

From the μ-reflectivity and ellipsometry experiments can be concluded that both methods are suitable to determine the film thickness in principle. The resulting polymer brush thicknesses of 329 to 352 Å obtained by x-ray are similar to the ellipsometric data of 360 to 393 Å which is a deviation of ∼7% in average. In order to get complementary results for perpendicular structures (normal to the sample surface) μ-GISAXS was conducted. However, the interfaces show the effect of correlated roughness which hinders the precise determination of the sample roughness. From the Yoneda peak position is

concluded that a polymer layer is present in the probed system.
It was identified by μ-reflectivity that the intermediate cantilever C6 is not coated homogeneously which is not clearly detectable by ellipsometry. Therefore, using a NCS as a sensor device, the obtained deflection data of an intermediate cantilever have to be treated with care due to possible artifacts.

6.4. Polyelectrolyte Multilayer Stripes

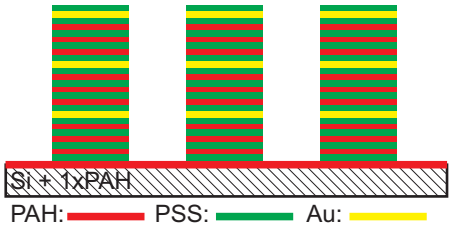

Fig. 6.70.: Schematic cross-section of three multilayer line structures. The lines are prepared by inkjet printing in a LbL technique on a silicon substrate which is fully covered by one PAH layer. First one line of PSS is printed followed by 3 PSS/PAH bilayers depositioned onto this line. Then one bilayer of gold nanoparticles/ PSS is added. This is repeated three times.

The second probed sample is a polyelectrolyte multilayer line structure prepared by inkjet printing. The multilayer system was modified to incorporate gold nanoparticles in the film. These gold nanoparticles carrying a positive charge are thought to be imbedded into the negatively charged polyelectrolyte layer of PSS. The diameter of the spherical particles was 4.1 ± 1.6 nm determined by scanning electron microscopy. Therefore the process was modified as follows (fig. 6.70): First three bilayer PAH/PSS were printed according to the procedure in chapter 4.2.1. Then a line with gold nanoparticles solution was printed followed by a PSS layer. This was repeated three times to get in total 12 bilayers.
Several experiments showed that the printed solution of gold nanoparticles spreads over the substrate if the optimized procedure for the substrate preparation described in chapter 4.2.1 was used. In this case the silicon substrate was covered with one bilayer PAH/PSS. When the terminating layer was switched from PSS to PAH, the printed gold nanoparticle solution kept the shape of the line.
The line structure was prepared on a silicon wafer of 1.5×1.5 cm^2 and had a line width of 220 μm. Such a line is suitable to be investigated with a microfocused x-ray beam (beam size: 17×35 μm^2) at the beamline BW4 at the HASYLAB. The wafer was aligned with the line structure parallel to the beam direction. In order to find the correct x-position of the line several μ-GISAXS images were taken at an incidence angle of $\alpha_i = 0.55°$ while scanning the wafer

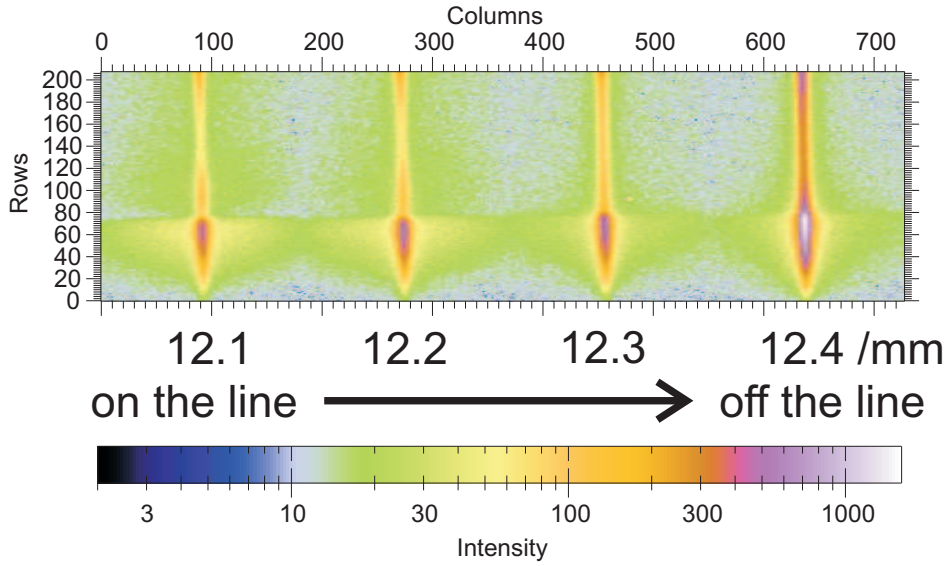

Fig. 6.71.: μ-GISAXS measurements taken at different x-positions. The scattering of the polymer film in the q_y and the q_z plane is more distinct than the scattering of the bare silicon. Therefore the intensity at the Yoneda peak is reduced. From left to right the beam is moved from the line structure to bare silicon. Therefore the pattern changes to bare silicon.

in x-direction. The correct x-position was found by analyzing the CCD peak pattern (see fig. 6.71). When the beam is directly on the line structure, then the scattering in q_y and q_z is more pronounced compared to bare silicon.
The prepared line structure is analyzed with μ-reflectivity and μ-GISAXS. Figure 6.72 (a) shows the reflectivity curve. From the difference in the minima Δq_z of the Kiessig pattern the layer thickness is calculated to be 155 ± 5 Å. The detector scan of the μ-GISAXS measurement at the incidence angle of $\alpha_i = 0.7°$ show an additional peak in the angular regime between the Yoneda and the specular peak which is most likely caused by correlated roughness 6.72 (b). Thus, the determination of the film roughness is not feasible. However, the oscillation of the reflectivity curve is not damped strongly which leads to the assumption that the roughness is less than 15 Å. A correlation distance d_{corr} of 123 Å was found.
The CCD image of the μ-GISAXS measurement already shows a significant scattering in the q_y plane (see fig. 6.71 left). In order to resolve lateral structures an out of plane scan is taken from the CCD image (see fig. 6.73). The curve shows a shoulder in the middle q-regime and in the high q-regime. A

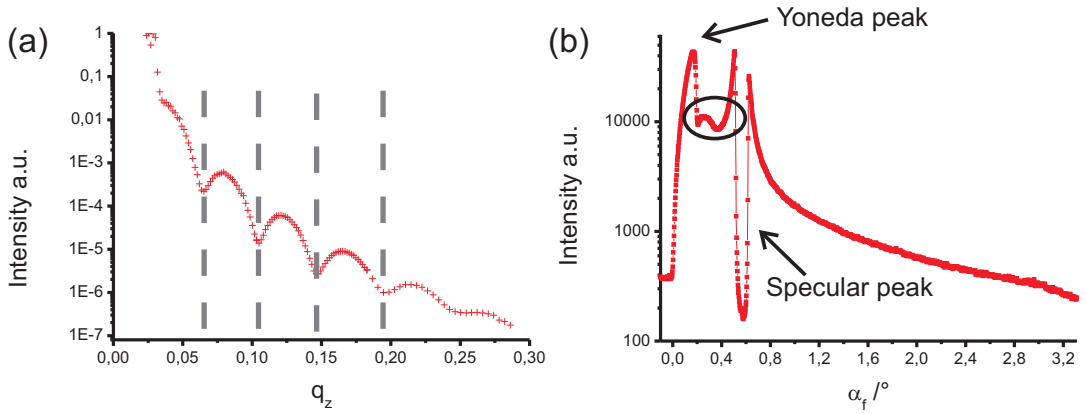

Fig. 6.72.: (a) Reflectivity of a PEM line structure with d = 155 Å. (b) Detector scan (q_z) for the same PEM line. The encircled peak is due to correlated roughness with d_{corr} = 123 Å.

closer analysis is done with a Unified Fit Model [184–186] to reveal structural features on multiple levels. It combines Guinier exponential and structurally limited power-law regimes. This model was introduced to fit small angle x-ray scattering data in transmission geometry. Lenz et al. recently showed that the Unified Fit Model can also be applied to the experimental data obtained from grazing incidence small angle x-ray scattering [187].
Two structural levels are identified by applying the Unified Fit Model to the out of plane scan. Level 1 indicates a power low factor of 4 which is associated to spherical particles with low anisotropy. The particles have a radius of gyration of R_g = 25 Å, which is in accordance to the given diameter of 41 Å. A low correlation exists between the particles with a mean distance to the next neighboring particles of 68 Å. The second structural level can be attributed to a polymer shell which surrounds the gold particle with a R_g = 117 nm- The power low factor is greater than 3 which predicts still a spherical structure with a less steady form. Thus, clusters of the gold particles can be excluded most likely.

Summary and Conclusion

Polyelectrolyte multilayers were successfully prepared with gold nanoparticles (d = 5 nm) incorporated. The inkjet process was modified to additionally

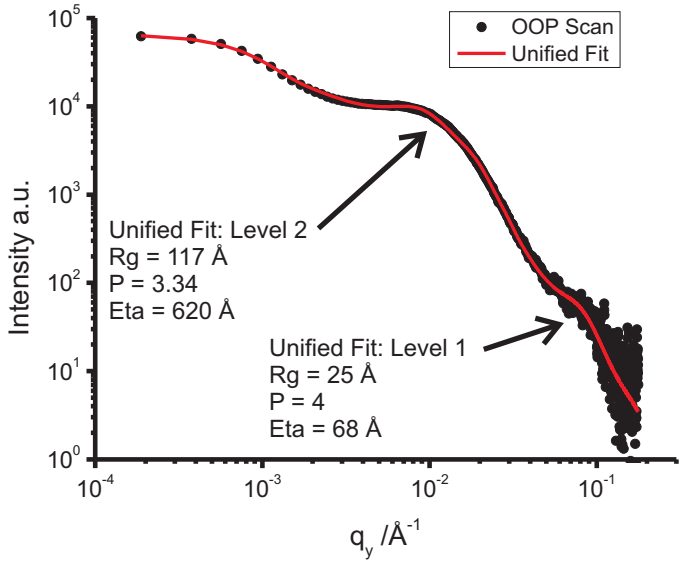

Fig. 6.73.: Out of plane Scan of a PEM line structure containing positive charged gold particle. The obtain curve is fitted by a unified fit model.

print the nanoparticle solution onto the line structure. In order to monitor the quality of the fabrication X-ray scattering was used. It was shown that the μ-sized x-ray beam is applicable to the 220 μm wide lines. From the scattering data a film thickness of 155 Å was revealed. It was possible to identify the gold nanoparticles as spherical structures with a radius of gyration of R_g = 25 Å which are most likely not clustered and surrounded with a polymer-shell.

7. Experimental

7.1. Materials

- Methyl methacylate (MMA) (Acros, 99%) was purified by passing through an alumina column and distilled under reduced pressure from CaH_2, and stored under argon at -20°C .
- Anisole (Aldrich, 99%)
- CuBr (Aldrich, 98%) was purified by boiling in mixture of 1:1 (by volume) Millipore water/ acid acetic and subsequently filtered off. The precipitate was rinsed with water, ethanol, and finally with diethyl ether and dried in a vacuum oven for 24 h.
- CuCl was synthesized according to the procedure described in the literature [188].
- $CuBr_2$ (Aldrich, 99%) was used without further purification.
- N, N, N', N', N''-pentamerhyldiethylenetrieamine (PMEDTA) (Aldrich, 99%) was purified by destillation under reduced pressure.
- Ethyl 2-bromoisobutyrate (2-EiBBr) (Aldrich, 98%) was used without further cleaning.
- Toluene was distilled from sodium under Argon atmosphere.
- Triethylamine was distilled from CaH_2 and stored under Argon atmosphere.
- The starter (**1**), 3-(2-bromoisobutyryl)propyl)dimethyl chlorosilane was synthesized following the procedure described in the literature [74] and

purified by distillation under reduced pressure. In order to prevent its degradation by moisture, the starter (**1**) was stored under an argon atmosphere over silica gel in a desiccator.

- Ethyl 2-chloropropionate (2-ECP) (Aldrich, 97 %) was used without further purification.
- N-isopropylacrylamide (NIPAM) (Acros, 99 %) was recrystallized from 4:1 hexan, toluene.
- 1-Methylimidazole (Acros, 99%) was distilled from KOH.
- 1-Chlorobutane is washed with H_2SO_4 and afterwards distilled from P_2O_5.
- Silicon wafers were purchased from Simat, Germany. The cleaning procedures are described in detail later.
- Poly(allylamine hydrochloride) (PAH, $M_w = 70000$ g/mol)and poyl(styrene sulfonate) (PSS, M_w = 70000 g/mol) were purchased from Aldrich and used without further purification.
- All other reagents were used as received. Solvents were at least HPLC grade.

7.2. Synthesis of [Bmim][PF6]

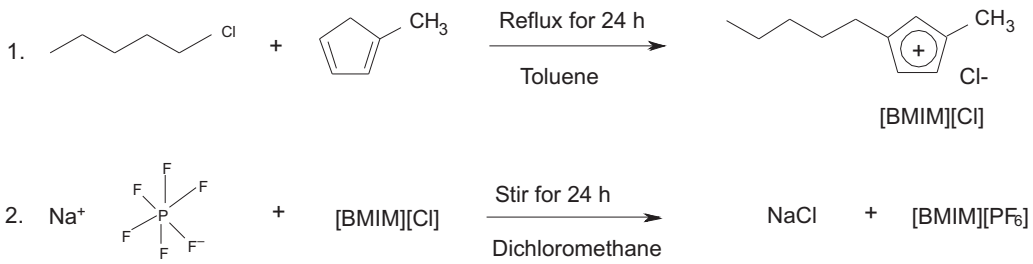

Fig. 7.74.: Synthesis of [Bmim][PF_6]

The reaction was carried out in anaerobic atmosphere of argon. In the first step 1-butyl-3-methylimidazolium chloride ([Bmim]Cl) was synthesized [189]. Add 1-chlorobutane (1.38 mol, 0.144 L) to 1-methylimidazole (1.25 mol) which was dissolved in toluene at 0°C . The solution was heated to 110 °C and was refluxed for 24 hours. The toluene was decanted and the residue was recrystallized from acetonitrile. For further purification the solid was repeatedly recrystallized from ethylacetate until white crystals were obtained.
The second step yielded 1-butyl-3-methylimidazolium hexafluorophosphate ([Bmim][PF_6]). $NaPF_6$ (0.32 mol) was added to a solution of [BMIM]Cl (0.29 mol) in dichloromethane and stirred for 24 hours. The originated suspension was decanted and washed with small portions of water until the precipitation of AgCl stopped when $AgNO_3$ solution was added to the aqueous phase. The organic phase was washed another two times with water to assure the removal of chloride. In vacuum the solvent was removed and the residue stirred with activated charcoal for 12 hours. By passing over a aluminum column the charcoal was removed. Subsequently the ionic liquid [Bmim][PF_6] was dried at 100 °C in vacuum for 24 h.
Characterization:
^{1}H NMR [189] ($CDCl_3$, 250 MHz): δ (ppm) = 8.68 (1H, s, NCHN), 7.25 (1H, m, CH3NCHCHN), 7.10 (1H, m, CH3NCHCHN), 4.16 (2H, t, J=7.4 Hz, NCH2-(CH2)2CH3), 3.94 (3H, s, NCH3), 1.86 (2H, m, NCH2CH2CH2CH3), 1.36 (2H, m, N(CH2)2CH2CH3), 0.95 (3H, t, J=7.3 Hz, N(CH2)3CH3)

7.3. Masking of Cantilever Arrays

In order to restrict the synthesis of polymer brushes to selective cantilever surfaces, it was deposited a blocking gold layer via thermal evaporation deposition rate 0.1 nm s^{-1} on the entire backside of the cantilever array and on half of its topside by masking the other half using a shadow mask [142] (fig. 7.75). The blocking layer restricted the functionalization of the cantilevers with an ATRP starter (see section 7.4) to nongold covered surfaces. In the next step the functionalized parts were “grafted from” with polymer brushes.

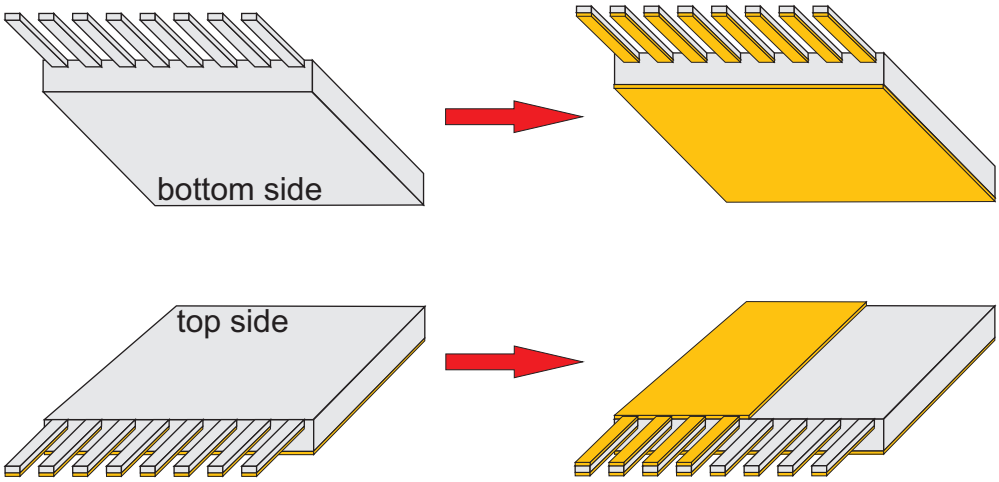

Fig. 7.75.: Process of applying a gold mask. The complete bottom side is covered with gold by thermal evaporation. Just half of the top side is coated with the gold layer using a shadow mask.

The gold layer can be removed by immersion of the gold covered chip for 30 s in a solution of KI/ I_2 (4:1). The solution was prepared of 1 g KI and 0.25 g I_2 in 40 mL water.

7.4. Immobilization of the ATRP-Initiator

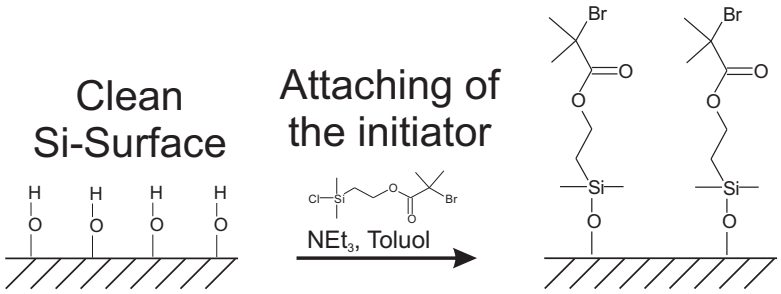

Fig. 7.76.: Attaching of the surface initiator for the ATRP synthesis

In order to prepare the silicon surface (either wafer pieces or micro cantilever) for the starter immobilization and to assure controlled hydration state of the silicon oxide layer on top, a base cleaning was performed. Silicon wafers and/or NMC-chips were immersed in a mixture of NH_3 (4 mL, 25%), H_2O_2 (4 mL, 35%) and Millipore water (50 mL) at 80 to 85 °C , for 20 min. Af-

terwards, the silicon surface was rinsed with copious amounts of Millipore water and dried with a N_2 flow.
The freshly prepared silicon wafers/ micro cantilever arrays were immersed in a solution of dry toluene (50 mL), triethylamine (400 μL, c = 50 mmolL^{-1}) and 3-((2-bromoisobutyryl)propyl)-dimethylchlorosilane (200 μL, c = 25 mmolL^{-1}). The solution was stirred for $\sim$20 h. Then, the silicon objects were placed in a soxhlet apparatus and extracted with dichloromethane for 1 h.

7.5. Synthesis of PMMA Brushes in [Bmim][PF_6]

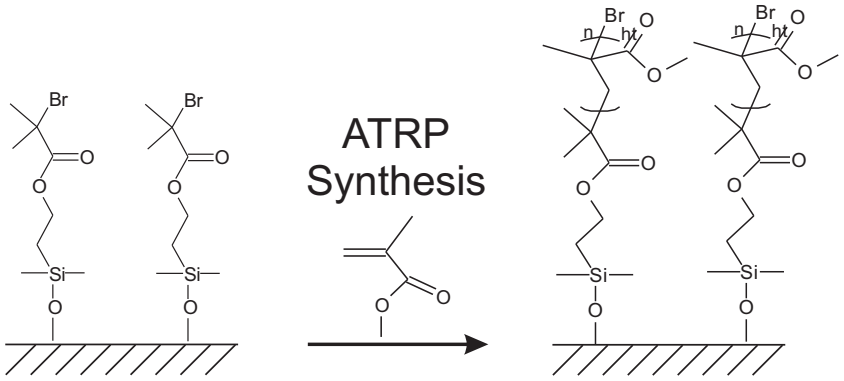

Fig. 7.77.: Synthesis of PMMA brush with atom transfer polymerization (ATRP). For details of the used solvent and catalyst see text: 7.5, 7.6, 3.2.

CuBr (7.3 mg; 0.05 mmol) and $CuBr_2$ (94 mg; 0.42 mmol) were filled into a modified Schlenk tube [**?**] under an argon atmosphere. Then the freshly functionalized wafer-pieces were placed into the tube, a solution of MMA (10 mL, 0.093 mol) in [Bmim][PF_6] (20 mL) and the ligand PMDETA (99 μL, 0.47 mmol) were added and the mixture was stirred for 10 min. After addition of 2-EiBBr (69 μL; 0.47 mmol), the Schlenk tube was sealed and oxygen was removed by three freeze-pump-thaw cycles.
Then the reaction container was transferred into a glove box, samples were taken from the wafers and the reaction solution after appropriate time intervals. The wafer-pieces were rinsed with plenty of THF and subsequently extracted with dichloromethane in a soxhlet apparatus overnight. PMMA

was precipitated twice in methanol or hexane (depending on the molecular weight) and directly analyzed by GPC.
Characterization:
^{1}H NMR [142] ($CDCl_3$, 250 MHz): δ (ppm) = 3.58 (s, 1H, -O-CH_3), 0.72 - 1.67 (m, 5H, -CH_2-C-CH_3, Backbone).

7.6. Synthesis of PMMA Brushes in Anisole

For the grafting from ATRP reaction an elaborated setup was used because the volume change of the liquid during the freeze-pump-thaw cycle would break the cantilevers. Therefore a the reaction was carried out under reduced pressure, in a set-up consisting of an adapted Schlenk tube connected to a Schlenk flask (see figure 7.78). The adapted Schlenk tube was modified, thus both the special holder for the microcantilever arrays and a silicon wafer are fitting inside. The starterfunctionalized silicon pieces mounted in the special holder have been introduced in an adapted Schlenk tube. The reaction mixture was added into the Schlenk flask, with the mixing ratio: CuBr (52 mg, 0.36 mmol), anisole (19.4 mL) (previously deaerated by bubbling argon for 1.5 h), PMDETA (77 μL, 0.36 mmol), and MMA (19.6 mL, 0.18 mol), and stirred until a homogenous green solution was obtained. After adding the 2-Ethyl 2-bromoisobutyrate (2-EiBBr) (52 μL, 0.35 mmol), the sacrificial initiator, the reaction mixture was carefully degassed by several freeze-thawing cycles. Subsequently, the reaction solution was decanted into the adapted Schlenk tube by just rotating the Schlenk flask up side down. The reaction was carried out at 35°C under reduced pressure for 23 h, after which the microcantilever holder was removed from the reaction mixture, and rinsed with dichloromethane and then transferred to a soxhlet apparatus for 12 h extraction with dichloromethane to assure the complete removal of the free polymer. The bulk polymer was obtained by adding a morcoporous ionic exchange resin DOWEX MSC. After 10 min stirring the solution is filtered over a alumina column to remove the residual copper complex. The polymer was precipitated twice in methanol and finally dried under vacuum. Characteri-

zation wa done with GPC and NMR.

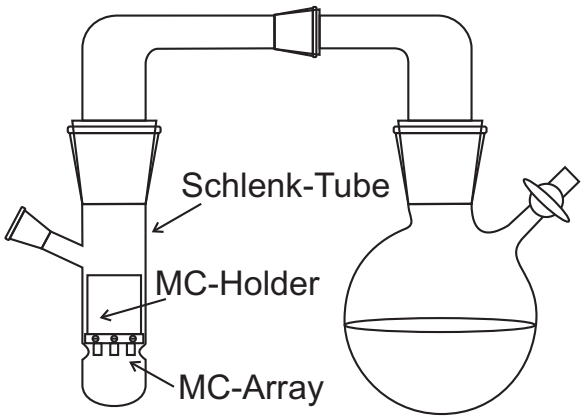

Fig. 7.78.: Schlenk like setup for polymer brush synthesis on microcantilever arrays. The cantilevers are very fragile and consequently the oxygen can not be removed from the reaction solution with freeze-pump-thaw cycles while the microcantilevers are in the solution bath. Therefore the solution was prepared in an extra Schlenk flask (right) and then transferred via a connecting tube to the Schlenk tube equipped with the microcantilever array holder. (figure from [?])

7.7. Synthesis of PNIPAM Brushes in Water/ DMF

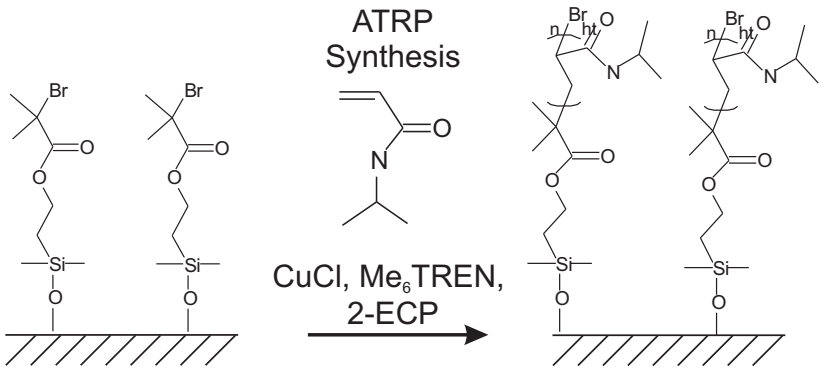

Fig. 7.79.: Synthesis of PNIPAM brush with atom transfer polymerization (ATRP).

Analogous to the steps described in the pervious part 7.6 the ATRP reaction for grafting PNIPAM brushes was performed. In a modified Schlenk-like setup [?] (see figure 7.78) the initial functionalized silicon wafer and NMC

chip were placed in the Schlenk tube and the reaction solution was prepared in DMF/H2O (1:1, V = 28 mL) containing the monomer NIPAM (m = 2.72 g), the ATRP catalyst CuCl (m = 9.5 mg), the ligand Me_6TREN (V = 27,9 μL) and sacrificial initiator ethyl 2-chloropropionate (XXXX). After 1 h reaction time the NMC-chip was rinsed consecutively with Millipore water, methanol and dichloromethane. The bulk polymer is obtained by dialysis (MWCO = 2000 Dalton, Spectrum Laboratories) and subsequent dehydration in vacuum.

Characterization:
^{1}H NMR [190] ($CDCl_3$, 250 MHz): δ (ppm) = 4.00 (s, 1H, -CH-N-), 3.63 (s, 1H, -NH-), 2.13-1.37 (m, 3H, -CH_2-CH-, Backbone), 1.13 (s, 6H, -CH_3).

7.8. Plasma Deposition of ppDEA

Plasma deposition of ppDEA: Deposition of plasma polymerized N,N-diethylacrylamide (ppDEA) thin films was carried out in a home-built capacitively coupled rf (13.56 MHz) plasma reactor under the continuous wave mode [158]. The N,N-diethylacrylamide monomer was purchased from ABCR (Karlsruhe, Germany). The monomer was outgassed three times before use, but was not purified further. The monomer vapor pressure during the plasma polymerization process was about 0.03 mbar. In order to improve the adhesion between the substrates and the ppDEA films, 50 W ppDEA was firstly deposited onto the substrate for approx. 10 s, and then the plasma power was reduced to 2 W. The previous contact angle measurements demonstrated that a 2 W ppDEA was temperature sensitive with a LCST at 38 - 41°C [158]. The film thickness was controlled by adjusting the deposition time at an input power of 2 W.

7.9. Preparation of Silicon Wafers for LbL procedure

Silicon wafers were cleaned in ultra sonication bath of acetone, isopropanol, distilled water, freshly prepared piranha solution (H_2O_2 : H_2SO_4 = 1:3), distilled water in sequence, and finally dried in N_2 flow.

7.10. Polyelectrolyte/Salt Solution Preparation

PAH and PSS solutions containing salts were prepared using MilliQ water (18.2 Ω). The concentration of the solution c = 3×10^{-3} mol/L was based on the molecular weight per repeat unit within each polymer. Additionally, salt either NaCl or $CaCl_2$ was added to the polyelectrolyte solution in a concentration of 0.2 to 1 mol/L.

7.11. Preparation of Gold Nanoparticle

The gold nanoparticle solution was provided by Marcus Schmelzeisen. The positive charged nanoparticles were synthesized according to the procedure described by Gittins and Caruso [191]. The 4-(Dimethylamino)pyridine ligand was exchanged against the ligand N,N,N-Trimethyl(11-mercaptoundecyl)-ammonium chloride. A solution of N,N,N-Trimethyl(11-mercaptoundecyl)-ammonium chloride (5.69 mg in 30 mL) in ethanol, which was set to a pH-value of 10 with 10% KOH solution, was added to an aqueous solution of the gold nanoparticles (20 mL). This mixture was left overnight. The obtained aqueous solution had a concentration of 1 mg/mL. Scanning electron microscopy revealed a diameter of 4.1 ± 1.6 nm.

Synthesis of N,N,N-Trimethyl(11-mercaptoundecyl)ammonium chloride

N,N,N-Trimethyl-10-undecenylammonium bromide: 12.5 mL undecenylbromide was given to a solution of trimethylamine in methanol (10 g in 50 mL) at room temperature. The mixture was stirred for two days. Afterwards

the solvents was evaporated and the remaining solid dissolved in ∼30 mL dichloromethane. The product was precipitated in 500 mL hexane as colorless solid.

Characterization:

^{1}H NMR (CD_3OD): 1.23-1.47 (m, 12H,CH_2), 1.70-1.83 (m, 2H,$CH_2CH_2N^+$), 1.96-2.08 (m, 2 H, $CH_2CH{=}CH_2$), 3.09 (s, 9 H, NMe_3^+), 3.25-3.38 (m,2H,CH_2N^+), 4.90-5.04 (m, 2 H, $CH{=}CH_2$), 5.72-5.91 (m, 1 H,$CH{=}CH_2$).

N,N,N-Trimethyl(11-mercaptoundecyl)ammonium chloride: 2.28 g freshly distilled thioacetic acid and 0.1 g 2,2'-Azo(isobutyronitrile) (AIBN) were given into a solution of N,N,N-trimethyl-10-undecenylammonium bromide in chloroform (2.92 g in 25 mL). The mixture was stirred at 80°C for 20 h. Subsequently all solvents was distilled off. A yellow precipitate remained which was washed 6 times with ice cold diethyl ether. After drying in vaccum 10% HCl (20 mL) was added to the solid and for 1 h heated under reflux. The solvent was removed in vaccum and the remaining solid was recrystallized with charcol under argon atmosphere. A colorless solid is obtained.

Characterization:

^{1}H NMR (D_2O): 1.24-1.49 (m, 14H,CH_2), 1.53-1.66 (m, 2 H, CH_2CH_2SH), 1.67-1.84 (m, 2 H, $CH_2CH_2NMe_3^+$),2.52 (t, 8 Hz, 2 H, CH_2SH), 3.12 (s, 9 H, NMe_3^+), 3.30-3.41 (m,2H,$CH_2NMe_3^+$).

8. Summary

In this study, polymers were used to create 3D patterned surfaces. The applications range from PMMA and PNIPAM polymerbrushes, over solvent assisted restructuring of polystyrene, to polyelectrolyte multilayer structures consisting of PAH/PSS.

In the first part poly(methyl methacrylate) (PMMA) brushes were synthesized with atom transfer radical polymerization (ATRP) in the room temperature ionic liquid 1-butyl-3-methylimidazolium hexafluorophosphate ([Bmim][PF_6]). Kinetic studies revealed a linear and dense brush growth with a rate of 4600 g/mol per nm. An average grafting density of 0.36 μmol/m^2 was achieved. Microdroplets of [Bmim][PF_6] and the ATRP catalyst (1 μL) were applied to a silicon surface as microreactors. A polymer brush layer of 13 nm was prepared by sequential addition of the monomer methyl methacrylate. However, this procedure is limited limited through the evaporation of the monomer which evaporates within 100 s.

The second part focuses on the patterning of surfaces with a state of the art method, inkjet printing. A piezoelectric drop-on-demand print system was used to restructure a poly(styrene) plate with 0.4 nL droplets of toluene. The subsequent formed microcavities are applicable as microlenses where the focal length can be adjusted by the number of droplets used for the restructuring. Experimentally, the focal length was determined to be in the range from 4.5 mm to 0.21 mm.

In the second structuring process the polyelectrolytes poly(allylamine hydrochloride) (PAH) and poly(styrene sulfonate) (PSS) were used to create 3D-structures by a layer-by-layer (LbL) deposition. 3D-structures such as lines, chessboards, rings and piles were designed. The thickness of one bilayer was identified to be in the range 0.6 - 1.1 nm using NaCl as electrolyte with a concentration of 0.5 mol/L. The width of the structures was in average 230 μm.

Also nanomechanical cantilever sensors (NCS) were coated by this quick and reproducible procedure. This resulted in an additional mass loaded onto the cantilevers of 0.55 ng for 5 bilayers and 1.08 ng for 10 bilayers. Furthermore the fabricated sensor was exposed to water vapor of defined content. The deflection of the NCS increased steadily with increasing humidity. This is caused by the swelling of the polymer film.
Nanomechanical cantilever sensors (NCS) were also used to investigate the thermal response of a 7 nm thick poly(N-isopropylacrylamide) (PNIPAM) polymer brush and a 187 nm thick ppDEA layer made from a plasma polymerization process of N,N-diethylacrylamide. The NCS deflection showed two different regimes: At temperatures $<$ LCST the deflection was dominated by dehydration, and at temperatures $>$ LCST the NCS response was attributed mainly to slow relaxation processes of the collapsed polymer layers. It was found that the minima in the differential deflection of NCS are in agreement with the LCST of 32°C and 44°C of the selected polymers, respectively.
In the final part of this thesis μ-reflectivity and μ-GISAXS are introduced as new methods to perform x-ray scattering experiments on microsized samples such as NCS and printed PEM line structures. The thickness of each individual PMMA coated NCS was determined to be in the range from 329 to 352 Å using μ-reflectivity. Within an error of $\sim$7% this is confirmed by imaging ellipsometry as a complementary method. Additionally, the polymerbrushes showed the phenomenon of correlated roughness which is obtained from the detector scan of a μ-GISAXS experiment. As a second example a printed polyelectrolyte multilayer line of PAH/PSS was investigated. The procedure of multilayer fabrication was modified to incorporate gold nanoparticles into the film structure. From the μ-GISAXS data the successful incorporation of the particles was found and the use of the Unified Fit Model revealed that the particles were not clustered and were surrounded by a polymershell.

List of Abbreviations

λ	wavelength
μL	micro liter
μm	micro meter
Å	Angstrom
$^{\circ}$C	degree Celsius
[Bmim][PF_6]	1-butyl-3-methylimidazolium hexafluorophosphate
2D	two dimensional
2-EiBBR	2-bromo-2-methylpropionate
3D	three dimensional
a.u.	arbitrary unit
AFM	atomic force microscopy or microscope
AG	Aktien Gesellschaft
AOI	angle of incidence
ATRP	atom transfer radical polymerization
BA	Born approximation
Be CLRs	parabolic compound refractive lenses made of beryllium
BiPy	2,2′-bipyridine
BL	bilayer
BW4	beamline with wiggler 4
C1-C8	cantilever 1 to cantilever 8
Calc.	calculated
CCA	constant contact angle
CCD	charged coupled device
CCR	constant contact radius
CHESS	Cornell High Energy Synchrotron Source
cm^2	centi meter squared

Corp.	corporation
cos	cosinus
D	distance
D	polydispersity index
D	diffusion coefficent
d	thickness
deg or °	degree
DESY	Deutsches Elektronen-Synchrotron
DMF	dimethylformamide
DoD	drop-on-demand
DWBA	Distorted wave Born approximation
e.g.	for example
elli	ellipsometry
eq.	equation
ESRF	European Synchrotron Radiation Facility
Exp.	experimental
fig.	figure
g	gram
g	gramm
GISAXS	grazing incidence small angle x-ray scattering
GIUSAXS	grazing incidence ultra small angle x-ray scattering
GmbH	Gesellschaft mit beschränkter Haftung
GPC	gel permeation chromatography
h	hour
HASYLAB	Hamburger Synchrotronstrahlungslabor
HeNe-Laser	Helium-Neon-Laser
HPLC	high pressure liquid chromatography
Hz	Hertz
i.e.	that is
IL	ionic liquid
Inc.	incorporation
k_p	propagation constant
kDa	kilo Dalton
LbL	layer-by-layer

LCD	liquid crystal display
LCST	lower critical solution temperature
Ltd.	limited
M_n	number average molecular weight
M_w	weight average molecular weight
mbar	milli bar
MC	micro cantilever
MCS	micro cantilever sensors
Me_6TREN	tris(2-dimethylaminoethyl)amine
MEMS	microelectromechanical systems
mg	milli gram
MHz	mega Hertz
min	minute-s
mL	milli liter
mm	milli meter
MMA	methyl methacrylate
mmHg	milli meter mercury
mmol	milli mol
MPIP	Max Planck Institute for Polymer Research
n	refractive index
NCS	nanomechanical cantilever sensor
NIPAM	N-isopropylacrylamide
nL	nano liter
nm	nano meter
NMC	nanomechanical cantilever
NMR	nuclear magnetic resonance
No. or #	number
PAH	poly(allylamine hydrochloride)
PCSA	polarizer compensator sample analyzer
PDEA	poly(N,N-diethylacrylamide)
PEEK	polyaryletheretherketone
PEM	polyelectrolyte multilayer
PhD	Doctor of Philosophy
pL	pico liter

PMDETA	N,N′,N′,N″,N″-pentamethyldiethylentriamine
PMMA	poly(methyl methacrylate)
PNIPAM	poly(N-isopropylacrylamide)
ppDEA	plasma polymerized N,N-diethylacrylamide
PS	poly(styrene)
PSS	poly(styrene sulfonate)
PVME	poly(vinylmethylether)
R	reflectivity
RAFT	Reversible additionfragmentation chain transfer
ROI	region of interest
ROMP	Ring opening metathesis polymerisation
s	second-s
SAM	self assembled monolayer
SEM	scanning electron microscope
sin	sinus
SPM	scanning probe microscopy or microscope
T	temperature
t	time
THF	tetrahydrofuran
TPCL	three phase contact line
USA	United States of America
V	volume
VPTT	volume phase transition temperature
vs.	versus
W	Watt

Bibliography

[1] Koch, K., Bhushan, B., und Barthlott, W., *Progress in Materials Science* **2009**, *54*(2), 137–178, Multifunctional surface structures of plants: An inspiration for biomimetics.

[2] Fuchs, E., *Nature* **2007**, *445*(7130), 834–842, Scratching the surface of skin development.

[3] Zhang, J. H., Sheng, X. L., und Jiang, L., *Langmuir* **2009**, *25*(3), 1371–1376, The Dewetting Properties of Lotus Leaves.

[4] Yanik, M. F., *Trends in Biotechnology* **2009**, *27*(1), 1–2, Towards gecko-feet-inspired bandages.

[5] Ertl, G., *Angewandte Chemie-International Edition* **2008**, *47*(19), 3524–3535, Reactions at surfaces: From atoms to complexity (Nobel lecture).

[6] Wegmann, M., Michen, B., und Graule, T., *Journal of the European Ceramic Society* **2008**, *28*(8), 1603–1612, Nanostructured surface modification of microporous ceramics for efficient virus filtration.

[7] Bruch, T., Graalfs, H., Jacob, L., und Frech, C., *Journal of Chromatography A* **2009**, *1216*(6), 919–926, Influence of surface modification on protein retention in ion-exchange chromatography Evaluation using different retention models.

[8] Matheson, R. R., *Polymer Reviews* **2006**, *46*(4), 341–346, Paint and coatings technology: Current industrial trends.

[9] Small, D. J. und Courtney, P. J., *Advanced Materials & Processes* **2005**, *163*(5), 44–47, Fundamentals of industrial adhesives.

[10] Raviv, U., Giasson, S., Kampf, N., Gohy, J. F., Jerome, R., und Klein, J., *Nature* **2003**, *425*(6954), 163–165, Lubrication by charged polymers.

[11] Hans-Jürgen Butt, Karlheinz Graf, M. K., *Physics and Chemistry of Interfaces;* WILEY-VCH, Weinheim, 2003.

[12] Hawker, C. J. und Wooley, K. L., *Science* **2005**, *309*(5738), 1200–1205, The convergence of synthetic organic and polymer chemistries.

[13] Braunecker, W. A. und Matyjaszewski, K., *Progress in Polymer Science* **2007**, *32*(1), 93–146, Controlled/living radical polymerization: Features, developments, and perspectives.

[14] Advincula, R. C. H., *Polymer brushes;* Wiley-VCH, Weinheim, 2004.

[15] G. Decher, J. B. S., Eds., *Multilayer Thin Films;* Vol. 1; Wiley-VCH, Weinheim, 2003.

[16] Sirringhaus, H., Kawase, T., Friend, R. H., Shimoda, T., Inbasekaran, M., Wu, W., und Woo, E. P., *Science* **2000**, *290*(5499), 2123–2126, High-resolution inkjet printing of all-polymer transistor circuits.

[17] Judy, J., *Smart Materials & Structures* **2001**, *10*(6), 1115–1134, Microelectromechanical systems (MEMS): fabrication, design and applications.

[18] Whitesides, G. M., *Nature* **2006**, *442*(7101), 368–373, The origins and the future of microfluidics.

[19] Ottevaere, H., Cox, R., Herzig, H. P., Miyashita, T., Naessens, K., Taghizadeh, M., Volkel, R., Woo, H. J., und Thienpont, H.; Comparing glass and plastic refractive microlenses fabricated with different technologies; In *1st Topical Meeting of the European-Optical-Society on Optical Microsystems*, pages S407–S429, Capri, ITALY, 2006. Iop Publishing Ltd; ISI Document Delivery No.: 056FN Times Cited: 17 Cited Reference Count: 55 Ottevaere, H. Cox, R. Herzig, H. P. Miyashita, T. Naessens, K. Taghizadeh, M. Voelkel, R. Woo, H. J. Thienpont, H.

[20] Tekin, E., Smith, P. J., und Schubert, U. S., *Soft Matter* **2008**, *4*(4), 703–713, Inkjet printing as a deposition and patterning tool for polymers and inorganic particles.

[21] Calvert, P., *Chemistry of Materials* **2001**, *13*(10), 3299–3305, Inkjet printing for materials and devices.

[22] Hon, K. K. B., Li, L., und Hutchings, I. M., *Cirp Annals-Manufacturing Technology* **2008**, *57*(2), 601–620, Direct writing technology-Advances and developments.

[23] Bietsch, A., Zhang, J. Y., Hegner, M., Lang, H. P., und Gerber, C., *Nanotechnology* **2004**, *15*(8), 873–880, Rapid functionalization of cantilever array sensors by inkjet printing.

[24] Lang, H. P. und Gerber, C.; Microcantilever sensors; In *Stm and Afm Studies On*, Vol. 285 of *Topics in Current Chemistry*, pages 1–27. Springer-Verlag Berlin, Berlin, 2008; ISI Document Delivery No.: BIG70 Times Cited: 0 Cited Reference Count: 135 Lang, Hans Peter Gerber, Christoph BIO Review HEIDELBERGER PLATZ 3, D-14197 BERLIN, GERMANY.

[25] Fritz, J., Baller, M. K., Lang, H. P., Rothuizen, H., Vettiger, P., Meyer, E., Guntherodt, H. J., Gerber, C., und Gimzewski, J. K., *Science* **2000**, *288*(5464), 316–318, Translating biomolecular recognition into nanomechanics.

[26] Butt, H. J., Berger, R., Bonaccurso, E., Chen, Y., und Wang, J., *Advances in Colloid and Interface Science* **2007**, *133*(2), 91–104, Impact of atomic force microscopy on interface and colloid science.

[27] Robert, H. W., *Reports on Progress in Physics* **1996**, (3), 427, Confocal optical microscopy.

[28] Azzam, R. M. A. ; Bashara, N. M., *Ellipsometry and polarized light;* North-Holland, Amsterdam, 1977.

[29] Muller-Buschbaum, P., *Analytical and Bioanalytical Chemistry* **2003**, *376*(1), 3–10, Grazing incidence small-angle X-ray scattering: an advanced scattering technique for the investigation of nanostructured polymer films.

[30] Tompkins, H., *A users guide to Ellipsometry;* Academic Press, Boston, 1993.

[31] Wolkenhauer, M.; Advanced practical course: Physics and chemistry of interfaces: Ellipsometry, **2003**.

[32] Wolkenhauer, M.; *Durchdringungs- und Adsorptionsverhalten von Stern-Polymeren;* Phd, Johannes Gutenberg University Mainz, **2002**.

[33] Russell, T. P., *Materials Science Reports* **1990**, *5*(4), 171–271, X-ray and neutron reflectivity for the investigation of polymers.

[34] Tolan, M.; X-ray scattering from soft-matter thin films - materials science and basic research - introduction; In *X-Ray Scattering from Soft-Matter Thin Films*, Vol. 148 of *Springer Tracts in Modern Physics*, pages 1–+. Springer-Verlag Berlin, Berlin, 1999; ISI Document Delivery No.: BM31K Times Cited: 1 Cited Reference Count: 417 Review HEIDELBERGER PLATZ 3, D-14197 BERLIN, GERMANY.

[35] O. Glatter, O. K., *Small angle X-ray scattering;* Academic Press, 1982.

[36] Froemsdorf, A. **Jan.2009**, www.gisaxs.de.

[37] Smilgies, D.-M.; http://staff.chess.cornell.edu/ smilgies/gisaxs/gisaxs.php, **Feb.2008**.

[38] Dosch, H., Batterman, B. W., und Wack, D. C., *Physical Review Letters* **1986**, *56*(11), 1144, Depth-Controlled Grazing-Incidence Diffraction of Synchrotron X Radiation.

[39] Dosch, H., *Physical Review B* **1987**, *35*(5), 2137–2143, EVANESCENT ABSORPTION IN KINEMATIC SURFACE BRAGG-DIFFRACTION.

[40] Dosch, H., Mailander, L., Reichert, H., Peisl, J., und Johnson, R. L., *Physical Review B* **1991**, *43*(16), 13172–13186, LONG-RANGE ORDER NEAR THE CU3AU(001) SURFACE BY EVANESCENT X-RAY-SCATTERING.

[41] Yoneda, Y., *Physical Review* **1963**, *131*(5), 2010, ANOMALOUS SURFACE REFLECTION OF X RAYS.

[42] Vineyard, G. H., *Physical Review B* **1982**, *26*(8), 4146–4159, GRAZING-INCIDENCE DIFFRACTION AND THE DISTORTED-WAVE APPROXIMATION FOR THE STUDY OF SURFACES.

[43] Holy, V. und Baumbach, T., *Physical Review B* **1994**, *49*(15), 10668–10676, NONSPECULAR X-RAY REFLECTION FROM ROUGH MULTILAYERS.

[44] Roth, S. V., Dohrmann, R., Dommach, M., Kuhlmann, M., Kroger, I., Gehrke, R., Walter, H., Schroer, C., Lengeler, B., und Muller-Buschbaum, P., *Review of Scientific Instruments* **2006**, *77*(8), 085106–7, Small-angle options of the upgraded ultrasmall-angle x-ray scattering beamline BW4 at HASYLAB.

[45] Lengeler, B., Schroer, C. G., Kuhlmann, M., Benner, B., Guenzler, T. F., Kurapova, O., Zontone, F., Snigirev, A., und Snigireva, I.; Refractive x-ray lenses; In *7th Biennial Conference on High Resolution X-Ray Diffraction and Imaging*, pages A218–A222, Prague, CZECH REPUBLIC, 2004. Iop Publishing Ltd; ISI Document Delivery No.: 941VY Times Cited: 20 Cited Reference Count: 28.

[46] AG, N., *Operating Manual NanoFocus µSurf©;* NanoFocus AG, Oberhausen, 2004.

[47] Minsky, M.; Microscopy apparatus, **1957**.

[48] *Benutzerhandbuch Nano-Plotter 2.0/ Software NPC16;* Gesellschaft fr Silizium-Mikrosysteme mbH, 2004.

[49] www.gesim.de.

[50] Nett, S. K.; *ATRP Synthese von Poly(N-Isopropylacrylamid)-Bürsten in wässrigem Medium und Anpassung des Nano-Plotters™ zur Beschichtung von Mikrocantilever Sensoren;* Diploma, Johannes Gutenberg University of Mainz, **2006**.

[51] Lang, H. P., Berger, R., Andreoli, C., Brugger, J., Despont, M., Vettiger, P., Gerber, C., Gimzewski, J. K., Ramseyer, J. P., Meyer, E., und Guntherodt, H. J., *Applied Physics Letters* **1998**, *72*(3), 383–385, Sequential position readout from arrays of micromechanical cantilever sensors.

[52] Wasserscheid, P. H., *Ionic Liquids in Synthesis;* WILEY-VCH, Weinheim, 2008.

[53] Cinzia Chiappe, D. P.; Ionic liquids: solvent properties and organic reactivity, **2005**.

[54] Welton, T.; Room-temperature ionic liquids. solvents for synthesis and catalysis, **1999**.

[55] Parvulescu, V. I. und Hardacre, C., *Chemical Reviews* **2007**, *107*(6), 2615–2665, Catalysis in ionic liquids.

[56] Shimoda, T., Morii, K., Seki, S., und Kiguchi, H., *Mrs Bulletin* **2003**, *28*(11), 821–827, Inkjet printing of light-emitting polymer displays.

[57] Bumbu, G. G., Wolkenhauer, M., Kircher, G., Gutmann, J. S., und Berger, D., *Langmuir* **2007**, *23*(4), 2203–2207, Micromechanical cantilever technique: A tool for investigating the swelling of polymer brushes.

[58] Tsarevsky, N. V. und Matyjaszewski, K., *Chemical Reviews* **2007**, *107*(6), 2270–2299, "Green" atom transfer radical polymerization: From process design to preparation of well-defined environmentally friendly polymeric materials.

[59] Kubisa, P., *Progress in Polymer Science* **2004**, *29*(1), 3–12, Application of ionic liquids as solvents for polymerization processes.

[60] Hong, H. L., Zhang, H. W., Mays, J. W., Visser, A. E., Brazel, C. S., Holbrey, J. D., Reichert, W. M., und Rogers, R. D., *Chemical Communications* **2002**, (13), 1368–1369, Conventional free radical polymerization in room temperature ionic liquids: a green approach to commodity polymers with practical advantages.

[61] Carmichael, A. J., Haddleton, D. M., Bon, S. A. F., und Seddon, K. R., *Chemical Communications* **2000**, (14), 1237–1238, Copper(I) mediated living radical polymerisation in an ionic liquid.

[62] Perrier, S., Davis, T. P., Carmichael, A. J., und Haddleton, D. M.; First report of reversible addition-fragmentation chain transfer (raft) polymerisation in room temperature ionic liquids, **2002**.

[63] Harrisson, S., Mackenzie, S. R., und Haddleton, D. M., *Chemical Communications* **2002**, (23), 2850–2851, Unprecedented solvent-induced acceleration of free-radical propagation of methyl methacrylate in ionic liquids.

[64] Biedron, T. und Kubisa, P., *Macromolecular Rapid Communications* **2001**, *22*(15), 1237–1242, Atom-transfer radical polymerization of acrylates in an ionic liquid.

[65] Ma, H. Y., Wan, X. H., Chen, X. F., und Zhou, Q. F., *Polymer* **2003**, *44*(18), 5311–5316, Reverse atom transfer radical polymerization of methyl methacrylate in imidazolium ionic liquids.

[66] Zhang, H. Q., Klumperman, B., Ming, W. H., Fischer, H., und van der Linde, R., *Macromolecules* **2001**, *34*(18), 6169–6173, Effect of Cu(II) on the kinetics of the homogeneous atom transfer radical polymerization of methyl methacrylate.

[67] Matyjaszewski, K., Patten, T. E., und Xia, J. H., *Journal of the American Chemical Society* **1997**, *119*(4), 674–680, Controlled/"living" radical polymerization. Kinetics of the homogeneous atom transfer radical polymerization of styrene.

[68] Wang, J. L., Grimaud, T., und Matyjaszewski, K., *Macromolecules* **1997**, *30*(21), 6507–6512, Kinetic study of the homogeneous atom transfer radical polymerization of methyl methacrylate.

[69] Ejaz, M., Yamamoto, S., Ohno, K., Tsujii, Y., und Fukuda, T., *Macromolecules* **1998**, *31*(17), 5934–5936, Controlled graft polymerization of methyl methacrylate on silicon substrate by the combined use of the Langmuir-Blodgett and atom transfer radical polymerization techniques.

[70] Ejaz, M., Tsujii, Y., und Fukuda, T., *Polymer* **2001**, *42*(16), 6811–6815, Controlled grafting of a well-defined polymer on a porous glass filter by surface-initiated atom transfer radical polymerization.

[71] Huang, X. und Wirth, M. J.; Surface initiation of living radical polymerization for growth of tethered chains of low polydispersity, **1999**.

[72] von Werne, T. und Patten, T. E.; Atom transfer radical polymerization from nanoparticles: A tool for the preparation of well-defined hybrid nanostructures and for understanding the chemistry of controlled/"living" radical polymerizations from surfaces, **2001**.

[73] Kong, X. X., Kawai, T., Abe, J., und Iyoda, T., *Macromolecules* **2001**, *34*(6), 1837–1844, Amphiphilic polymer brushes grown from the silicon surface by atom transfer radical polymerization.

[74] Ramakrishnan, A., Dhamodharan, R., und Ruhe, J., *Macromolecular Rapid Communications* **2002**, *23*(10-11), 612–616, Controlled growth of PMMA brushes on silicon surfaces at room temperature.

[75] Degennes, P. G., *Macromolecules* **1980**, *13*(5), 1069–1075, Conformations of Polymers Attached to an Interface.

[76] Alexander, S., *Journal De Physique* **1977**, *38*(8), 983–987, Adsorption of Chain Molecules with a Polar Head a-Scaling Description.

[77] Picknett, R. G. und Bexon, R., *Journal of Colloid and Interface Science* **1977**, *61*(2), 336–350, EVAPORATION OF SESSILE OR PENDANT DROPS IN STILL AIR.

[78] Fang, X. H., Li, B. Q., Petersen, E., Ji, Y., Sokolov, J. C., und Rafailovich, M. H., *Journal of Physical Chemistry B* **2005**, *109*(43), 20554–20557, Factors controlling the drop evaporation constant.

[79] Butt, H. J., Golovko, D. S., und Bonaccurso, E., *Journal of Physical Chemistry B* **2007**, *111*(19), 5277–5283, On the derivation of Young's equation for sessile drops: Nonequilibrium effects due to evaporation.

[80] Schonfeld, F., Graf, K., Hardt, S., und Butt, H. J., *International Journal of Heat and Mass Transfer* **2008**, *51*(13-14), 3696–3699, Evaporation dynamics of sessile liquid drops in still air with constant contact radius.

[81] Cheng, A. K. H., Soolaman, D. M., und Yu, H. Z., *Journal of Physical Chemistry B* **2006**, *110*(23), 11267–11271, Evaporation of microdroplets of ethanol-water mixtures on gold surfaces modified with self-assembled monolayers.

[82] Liu, C. J., Bonaccurso, E., und Butt, H. J., *Physical Chemistry Chemical Physics* **2008**, *10*(47), 7150–7157, Evaporation of sessile water/ethanol drops in a controlled environment.

[83] Xia, Y. N. und Whitesides, G. M., *Annual Review of Materials Science* **1998**, *28*, 153–184, Soft lithography.

[84] photolithography, G. r. o., *a special issue of IBM J. Res. Dev.* **1997**, *(1-3)*, Optical lithography.

[85] N., H., Pispas, S., und Floudas, G., *Block copolymers : synthetic strategies, physical properties, and applications;* Wiley-Interscience: Hoboken, Weinheim, 2003.

[86] de Gans, B. J., Duineveld, P. C., und Schubert, U. S., *Advanced Materials* **2004**, *16*(3), 203–213, Inkjet printing of polymers: State of the art and future developments.

[87] Deegan, R. D., Bakajin, O., Dupont, T. F., Huber, G., Nagel, S. R., und Witten, T. A., *Nature* **1997**, *389*(6653), 827–829, Capillary flow as the cause of ring stains from dried liquid drops.

[88] Deegan, R. D., Bakajin, O., Dupont, T. F., Huber, G., Nagel, S. R., und Witten, T. A., *Physical Review E* **2000**, *62*(1), 756–765, Contact line deposits in an evaporating drop.

[89] Ko, H. Y., Park, J., Shin, H., und Moon, J., *Chemistry of Materials* **2004**, *16*(22), 4212–4215, Rapid self-assembly of monodisperse colloidal spheres in an ink-jet printed droplet.

[90] de Gans, B. J. und Schubert, U. S., *Langmuir* **2004**, *20*(18), 7789–7793, Inkjet printing of well-defined polymer dots and arrays.

[91] Park, J. und Moon, J., *Langmuir* **2006**, *22*(8), 3506–3513, Control of colloidal particle deposit patterns within picoliter droplets ejected by ink-jet printing.

[92] Bonaccurso, E., Butt, H. J., Hankeln, B., Niesenhaus, B., und Graf, K., *Applied Physics Letters* **2005**, *86*(12), 3, Fabrication of microvessels and microlenses from polymers by solvent droplets.

[93] Land, M. F., *Pure and Applied Optics* **1997**, *6*(6), 599–602, Microlens arrays in the animal kingdom.

[94] K. Iga, Y. K. und Oikawa, M., *Fundamentals of Microoptics: Distributed-Index, Microlens, and Stacked Planar Optics;* Tokyo, 1984.

[95] Yabu, H. und Shimomura, M., *Langmuir* **2005**, *21*(5), 1709–1711, Simple fabrication of micro lens arrays.

[96] Chang, C. Y., Yang, S. Y., Huang, L. S., und Jeng, T. M., *Journal of Micromechanics and Microengineering* **2006**, *16*(5), 999–1005, A novel method for rapid fabrication of microlens arrays using micro-transfer molding with soft mold.

[97] Chang, C. Y., Yang, S. Y., Huang, L. S., und Hsieh, K. H., *Optics Express* **2006**, *14*(13), 6253–6258, Fabrication of polymer microlens arrays using capillary forming with a soft mold of micro-holes array and UV-curable polymer.

[98] Keyworth, B. P., Corazza, D. J., McMullin, J. N., und Mabbott, L., *Applied Optics* **1997**, *36*(10), 2198–2202, Single-step fabrication of refractive microlens arrays.

[99] Danzebrink, R. und Aegerter, M. A.; Deposition of micropatterned coating using an ink-jet technique; In *2nd International Conference on Coating on Glass (ICCG)*, pages 115–118, Saarbrucken, Germany, 1998. Elsevier Science Sa; ISI Document Delivery No.: 235KM Times Cited: 23 Cited Reference Count: 14.

[100] Yang, S., Krupenkin, T. N., Mach, P., und Chandross, E. A., *Advanced Materials* **2003**, *15*(11), 940–+, Tunable and latchable liquid microlens with photopolymerizable components.

[101] Krupenkin, T., Yang, S., und Mach, P., *Applied Physics Letters* **2003**, *82*(3), 316–318, Tunable liquid microlens.

[102] Kawase, T., Sirringhaus, H., Friend, R. H., und Shimoda, T., *Advanced Materials* **2001**, *13*(21), 1601–+, Inkjet printed via-hole interconnections and resistors for all-polymer transistor circuits.

[103] de Gans, B. J., Hoeppener, S., und Schubert, U. S., *Advanced Materials* **2006**, *18*(7), 910–+, Polymer-relief microstructures by inkjet etching.

[104] Stupperich-Sequeira, C., Graf, K., und Wiechert, W., *Mathematical and Computer Modelling of Dynamical Systems* **2006**, *12*(4), 263–276, Modelling and simulation of micro-well formation.

[105] Gu, E., Choi, H. W., Liu, C., Griffin, C., Girkin, J. M., Watson, I. M., Dawson, M. D., McConnell, G., und Gurney, A. M., *Applied Physics Letters* **2004**, *84*(15), 2754–2756, Reflection/transmission confocal microscopy characterization of single-crystal diamond microlens arrays.

[106] von Klitzing, R., *Physical Chemistry Chemical Physics* **2006**, *8*(43), 5012–5033, Internal structure of polyelectrolyte multilayer assemblies.

[107] Decher, G., Hong, J. D., und Schmitt, J.; Buildup of ultrathin multilayer films by a self-assembly process .3. consecutively alternating adsorption of anionic and cationic polyelectrolytes on charged surfaces; In

5th International Conf on Langmuir-Blodgett Films, pages 831–835, Paris, France, 1991. Elsevier Science Sa Lausanne; ISI Document Delivery No.: HV025 Times Cited: 1080 Cited Reference Count: 13.

[108] Salomaki, M., Laiho, T., und Kankare, J., *Macromolecules* **2004**, *37*(25), 9585–9590, Counteranion-Controlled Properties of Polyelectrolyte Multilayers.

[109] Buscher, K., Graf, K., Ahrens, H., und Helm, C. A., *Langmuir* **2002**, *18*(9), 3585–3591, Influence of Adsorption Conditions on the Structure of Polyelectrolyte Multilayers.

[110] Shiratori, S. S. und Rubner, M. F., *Macromolecules* **2000**, *33*(11), 4213–4219, pH-Dependent Thickness Behavior of Sequentially Adsorbed Layers of Weak Polyelectrolytes.

[111] Losche, M., Schmitt, J., Decher, G., Bouwman, W. G., und Kjaer, K., *Macromolecules* **1998**, *31*(25), 8893–8906, Detailed structure of molecularly thin polyelectrolyte multilayer films on solid substrates as revealed by neutron reflectometry.

[112] Steitz, R., Leiner, V., Siebrecht, R., und v. Klitzing, R., *Colloids and Surfaces A: Physicochemical and Engineering Aspects* **2000**, *163*(1), 63–70, Influence of the ionic strength on the structure of polyelectrolyte films at the solid/liquid interface.

[113] Ariga, K., Hill, J. P., und Ji, Q. M., *Physical Chemistry Chemical Physics* **2007**, *9*(19), 2319–2340, Layer-by-layer assembly as a versatile bottom-up nanofabrication technique for exploratory research and realistic application.

[114] Zotti, G., Vercelli, B., und Berlin, A., *Accounts of Chemical Research* **2008**, *41*(9), 1098–1109, Monolayers and multilayers of conjugated polymers as nanosized electronic components.

[115] Hoven, C. V., Garcia, A., Bazan, G. C., und Nguyen, T. Q., *Advanced Materials* **2008**, *20*(20), 3793–3810, Recent Applications of Conjugated Polyelectrolytes in Optoelectronic Devices.

[116] Han, J. T., Zheng, Y., Cho, J. H., Xu, X., und Cho, K., *Journal of Physical Chemistry B* **2005**, *109*(44), 20773–20778, Stable superhydrophobic organic-inorganic hybrid films by electrostatic self-assembly.

[117] Zhang, J. T., Chua, L. S., und Lynn, D. M., *Langmuir* **2004**, *20*(19), 8015–8021, Multilayered thin films that sustain the release of functional DNA under physiological conditions.

[118] Park, M. K., Deng, S. X., und Advincula, R. C., *Journal of the American Chemical Society* **2004**, *126*(42), 13723–13731, pH-sensitive bipolar ion-permselective ultrathin films.

[119] Lee, D., Nolte, A. J., Kunz, A. L., Rubner, M. F., und Cohen, R. E., *Journal of the American Chemical Society* **2006**, *128*(26), 8521–8529, pH-Induced Hysteretic Gating of Track-Etched Polycarbonate Membranes: Swelling/Deswelling Behavior of Polyelectrolyte Multilayers in Confined Geometry.

[120] Caruso, F., Caruso, R. A., und Mohwald, H., *Science* **1998**, *282*(5391), 1111–1114, Nanoengineering of inorganic and hybrid hollow spheres by colloidal templating.

[121] Donath, E., Sukhorukov, G. B., Caruso, F., Davis, S. A., und Mohwald, H., *Angewandte Chemie-International Edition* **1998**, *37*(16), 2202–2205, Novel hollow polymer shells by colloid-templated assembly of polyelectrolytes.

[122] Cho, J., Char, K., Hong, J. D., und Lee, K. B., *Advanced Materials* **2001**, *13*(14), 1076–+, Fabrication of highly ordered multilayer films using a spin self-assembly method.

[123] Porcel, C. H., Izquierdo, A., Ball, V., Decher, G., Voegel, J. C., und Schaaf, P., *Langmuir* **2005**, *21*(2), 800–802, Ultrathin coatings and (poly(glutamic acid)/polyallylamine) films deposited by continuous and simultaneous spraying.

[124] Izquierdo, A., Ono, S. S., Voegel, J. C., Schaaff, P., und Decher, G., *Langmuir* **2005**, *21*(16), 7558–7567, Dipping versus spraying: Exploring the deposition conditions for speeding up layer-by-layer assembly.

[125] Kolasinska, M., Krastev, R., Gutberlet, T., und Warszynski, P., *Langmuir* **2009**, *25*(2), 1224–1232, Layer-by-Layer Deposition of Polyelectrolytes. Dipping versus Spraying.

[126] Liu, Y. J., Wang, Y. X., und Claus, R. O., *Chemical Physics Letters* **1998**, *298*(4-6), 315–319, Layer-by-layer ionic self-assembly of Au colloids into multilayer thin-films with bulk metal conductivity.

[127] Jiang, X. und Hammond, P. T., *Langmuir* **2000**, *16*(22), 8501–8509, Selective Deposition in Layer-by-Layer Assembly: Functional Graft Copolymers as Molecular Templates.

[128] Gao, M. Y., Sun, J. Q., Dulkeith, E., Gaponik, N., Lemmer, U., und Feldmann, J., *Langmuir* **2002**, *18*(10), 4098–4102, Lateral patterning of CdTe nanocrystal films by the electric field directed layer-by-layer assembly method.

[129] Jang, H., Kim, S., und Char, K., *Langmuir* **2003**, *19*(8), 3094–3097, Multilayer line micropatterning using convective self-assembly in microfluidic channels.

[130] Sukhishvili, S. A. und Granick, S., *Journal of the American Chemical Society* **2000**, *122*(39), 9550–9551, Layered, erasable, ultrathin polymer films.

[131] Hiller, J., Mendelsohn, J. D., und Rubner, M. F., *Nature Materials* **2002**, *1*(1), 59–63, Reversibly erasable nanoporous anti-reflection coatings from polyelectrolyte multilayers.

[132] Yang, S. Y. und Rubner, M. F., *Journal of the American Chemical Society* **2002**, *124*(10), 2100–2101, Micropatterning of polymer thin films with pH-sensitive and cross-linkable hydrogen-bonded polyelectrolyte multilayers.

[133] Shi, F., Dong, B., Qiu, D. L., Sun, J. Q., Wu, T., und Zhang, X., *Advanced Materials* **2002**, *14*(11), 805–809, Layer-by-layer self-assembly of reactive polyelectrolytes for robust multilayer patterning.

[134] Gong, X., Yang, J., Han, L., und Gao, C., *Langmuir* **2008**, *24*(24), 13925–13933, Influence of Drying Time of Polyelectrolyte Multilayers on the Compression-Induced Pattern Formation.

[135] Toda, M., Itakura, A. N., Igarashi, S., Buscher, K., Gutmann, J. S., Graf, K., und Berger, R., *Langmuir* **2008**, *24*(7), 3191–3198, Surface stress, thickness, and mass of the first few layers of polyelectrolyte.

[136] Bresenham, J. E., *Ibm Systems Journal* **1965**, *4*(1), 25–30, ALGORITHM FOR COMPUTER CONTROL OF A DIGITAL PLOTTER.

[137] Pitteway, M. L., *Computer Journal* **1967**, *10*(3), 282–&, ALGORITHM FOR DRAWING ELLIPSES OR HYPERBOLAE WITH DIGITAL PLOTTER.

[138] Lavrik, N. V., Sepaniak, M. J., und Datskos, P. G., *Review of Scientific Instruments* **2004**, *75*(7), 2229–2253, Cantilever transducers as a platform for chemical and biological sensors.

[139] Bhushan, B.; Nanomechanical cantilever array sensors; In *Springer Handbook of Nanotechnology*, pages 443–459. Springer, 2007.

[140] Singamaneni, S., LeMieux, M. C., Lang, H. P., Gerber, C., Lam, Y., Zauscher, S., Datskos, P. G., Lavrik, N. V., Jiang, H., Naik, R. R., Bunning, T. J., und Tsukruk, V. V., *Advanced Materials* **2008**, *20*(4), 653–680, Bimaterial microcantilevers as a hybrid sensing platform.

[141] Goeders, K. M., Colton, J. S., und Bottomley, L. A., *Chemical Reviews* **2008**, *108*(2), 522–542, Microcantilevers: Sensing chemical interactions via mechanical motion.

[142] Bumbu, G. G., Kircher, G., Wolkenhauer, M., Berger, R., und Gutmann, J. S., *Macromolecular Chemistry and Physics* **2004**, *205*(13), 1713–1720, Synthesis and characterization of polymer brushes on micromechanical cantilevers.

[143] Barnes, J. R., Stephenson, R. J., Woodburn, C. N., Oshea, S. J., Welland, M. E., Rayment, T., Gimzewski, J. K., und Gerber, C., *Review of Scientific Instruments* **1994**, *65*(12), 3793–3798, A FEMTOJOULE CALORIMETER USING MICROMECHANICAL SENSORS.

[144] Berger, R., Gerber, C., Gimzewski, J. K., Meyer, E., und Guntherodt, H. J., *Applied Physics Letters* **1996**, *69*(1), 40–42, Thermal analysis using a micromechanical calorimeter.

[145] Barnes, J. R., Stephenson, R. J., Welland, M. E., Gerber, C., und Gimzewski, J. K., *Nature* **1994**, *372*(6501), 79–81, PHOTOTHERMAL SPECTROSCOPY WITH FEMTOJOULE SENSITIVITY USING A MICROMECHANICAL DEVICE.

[146] Berger, R., Lang, H. P., Gerber, C., Gimzewski, J. K., Fabian, J. H., Scandella, L., Meyer, E., und Guntherodt, H. J., *Chemical Physics Letters* **1998**, *294*(4-5), 363–369, Micromechanical thermogravimetry.

[147] Zhou, F., Shu, W. M., Welland, M. E., und Huck, W. T. S., *Journal of the American Chemical Society* **2006**, *128*(16), 5326–5327, Highly reversible and multi-stage cantilever actuation driven by polyelectrolyte brushes.

[148] Hu, L., Chu, L. Y., Yang, M., Yu, J., und Wang, H. D., *Chemical Engineering & Technology* **2007**, *30*(4), 523–529, A composite thermo-responsive membrane system for improved controlled-release.

[149] Jonas, A. M., Hu, Z. J., Glinel, K., und Huck, W. T. S., *Nano Letters* **2008**, *8*(11), 3819–3824, Effect of Nanoconfinement on the Collapse Transition of Responsive Polymer Brushes.

[150] Jones, D. M., Smith, J. R., Huck, W. T. S., und Alexander, C., *Advanced Materials* **2002**, *14*(16), 1130–1134, Variable adhesion of micropatterned thermoresponsive polymer brushes: AFM investigations of poly (N-isopropylacrylamide) brushes prepared by surface-initiated polymerizations.

[151] Filipcsei, G., Csetneki, I., Szilagyi, A., und Zrinyi, M.; Magnetic field-responsive smart polymer composites; In *Oligomers Polymer Composties*

Molecular Imprinting, Vol. 206 of *Advances in Polymer Science*, pages 137–189. Springer-Verlag Berlin, Berlin, 2007; ISI Document Delivery No.: BFZ31 Times Cited: 5 Cited Reference Count: 100 Review HEIDELBERGER PLATZ 3, D-14197 BERLIN, GERMANY.

[152] Mendes, P. M., *Chemical Society Reviews* **2008**, *37*(11), 2512–2529, Stimuli-responsive surfaces for bio-applications.

[153] Santer, S. und Ruhe, J., *Polymer* **2004**, *45*(25), 8279–8297, Motion of nano-objects on polymer brushes.

[154] Heskins, M., G. J. E., *J. Macromol. Sci. Chem. A2* **1968**, page 14411455.

[155] Tsuboi, Y., Yoshida, Y., Okada, K., und Kitamura, N., *Journal of Physical Chemistry B* **2008**, *112*(9), 2562–2565, Phase separation dynamics of aqueous solutions of thermoresponsive polymers studied by a laser T-jump technique.

[156] Sun, T. L., Wang, G. J., Feng, L., Liu, B. Q., Ma, Y. M., Jiang, L., und Zhu, D. B., *Angewandte Chemie-International Edition* **2004**, *43*(3), 357–360, Reversible switching between superhydrophilicity and superhydrophobicity.

[157] Annaka, M., Yahiro, C., Nagase, K., Kikuchi, A., und Okano, T., *Polymer* **2007**, *48*(19), 5713–5720, Real-time observation of coil-to-globule transition in thermosensitive poly (N-isopropylacrylamide) brushes by quartz crystal microbalance.

[158] Chu, L. Q., Zou, X. N., Knoll, W., und Forch, R., *Surface & Coatings Technology* **2008**, *202*(10), 2047–2051, Thermosensitive surfaces fabricated by plasma polymerization of N,N-diethylacrylamide.

[159] Hoy, R. S. und Grest, G. S., *Macromolecules* **2007**, *40*(23), 8389–8395, Entanglements of an end-grafted polymer brush in a polymeric matrix.

[160] Ruths, M., Johannsmann, D., Ruhe, J., und Knoll, W., *Macromolecules* **2000**, *33*(10), 3860–3870, Repulsive forces and relaxation on compression of entangled, polydisperse polystyrene brushes.

[161] Tagit, O., Tomczak, N., und Vancso, G. J., *Small* **2008**, *4*(1), 119–126, Probing the morphology and nanoscale mechanics of single poly(N-isopropylacrylamide) microgels across the lower-critical-solution temperature by atomic force microscopy.

[162] Kujawa, P. und Winnik, F. M., *Macromolecules* **2001**, *34*(12), 4130–4135, Volumetric studies of aqueous polymer solutions using pressure perturbation calorimetry: A new look at the temperature-induced phase transition of poly(N-isopropylacrylamide) in water and D2O.

[163] Wen-Hwa, C., Mehregany, M., und Mullen, R. L., *Journal of Micromechanics and Microengineering* **1993**, *3*(1), 4–7, Analysis of tip deflection and force of a bimetallic cantilever microactuator.

[164] Wang, W., Troll, K., Kaune, G., Metwalli, E., Ruderer, M., Skrabania, K., Laschewsky, A., Roth, S. V., Papadakis, C. M., und Muller-Buschbaum, P., *Macromolecules* **2008**, *41*(9), 3209–3218, Thin films of poly(N-isopropylacrylamide) end-capped with n-butyltrithiocarbonate.

[165] Jenkins, A. T. A., Hu, J., Wang, Y. Z., Schiller, S., Foerch, R., und Knoll, W., *Langmuir* **2000**, *16*(16), 6381–6384, Pulsed plasma deposited maleic anhydride thin films as supports for lipid bilayers.

[166] Cheng, X. H., Canavan, H. E., Stein, M. J., Hull, J. R., Kweskin, S. J., Wagner, M. S., Somorjai, G. A., Castner, D. G., und Ratner, B. D., *Langmuir* **2005**, *21*(17), 7833–7841, Surface chemical and mechanical properties of plasma-polymerized N-isopropylacrylamide.

[167] Klein, C. A., *Journal of Applied Physics* **2000**, *88*(9), 5487–5489, How accurate are Stoney's equation and recent modifications.

[168] Yu, H. H. und Jiang, D. S., *Chinese Journal of Polymer Science* **2002**, *20*(1), 1–7, Ionic self-assembly and humidity sensitivity of polyelectrolyte multilayers.

[169] Lv, X., Li, Y., Li, P., und Yang, M. J., *Sensors and Actuators B-Chemical* **2009**, *135*(2), 581–586, A resistive-type humidity sensor based on crosslinked polyelectrolyte prepared by UV irradiation.

[170] Ralf Kgler, J. S. W. K., *Macromolecular Chemistry and Physics* **2002**, *203*(2), 413–419, The Swelling Behavior of Polyelectrolyte Multilayers in Air of Different Relative Humidity and in Water.

[171] Nolte, A. J., Treat, N. D., Cohen, R. E., und Rubner, M. F., *Macromolecules* **2008**, *41*(15), 5793–5798, Effect of relative humidity on the Young's modulus of polyelectrolyte multilayer films and related nonionic polymers.

[172] Stoney, G. G., *Proceedings of the Royal Society of London Series a-Containing Papers of a Mathematical and Physical Character* **1909**, *82*(553), 172–175, The tension of metallic films deposited by electrolysis.

[173] Igarashi, S., Itakura, A. N., Toda, M., Kitajima, M., Chu, L., Chifene, A. N., Forch, R., und Berger, R., *Sensors and Actuators B-Chemical* **2006**, *117*(1), 43–49, Swelling signals of polymer films measured by a combination of micromechanical cantilever sensor and surface plasmon resonance spectroscopy.

[174] Riekel, C., *Reports on Progress in Physics* **2000**, *63*(3), 233–262, New avenues in x-ray microbeam experiments.

[175] Roth, S. V., Burghammer, M., Riekel, C., Muller-Buschbaum, P., Diethert, A., Panagiotou, P., und Walter, H., *Applied Physics Letters* **2003**, *82*(12), 1935–1937, Self-assembled gradient nanoparticle-polymer multilayers investigated by an advanced characterization method: microbeam grazing incidence x-ray scattering.

[176] Roth, S. V., Muller-Buschbaum, P., Burghammer, M., Walter, H., Panagiotou, P., Diethert, A., und Riekel, C.; Microbeam grazing incidence small angle x-ray scattering - a new method to investigate heterogeneous thin films and multilayers; In *17th International Congress on X-Ray Optics and Microanalysis*, pages 1765–1773, Chamonix, FRANCE, 2003. Pergamon-Elsevier Science Ltd; ISI Document Delivery No.: 867MZ Times Cited: 3 Cited Reference Count: 49.

[177] Muller-Buschbaum, P., Gutmann, J. S., Stamm, M., Cubitt, R., Cunis, S., von Krosigk, G., Gehrke, R., und Petry, W.; Dewetting of thin polymer-

blend films examined with gisas; In *6th International Conference on X-ray and Neutron Scattering*, pages 53–59, Noordwijkerhout, Netherlands, 1999. Elsevier Science Bv; ISI Document Delivery No.: 307CF Times Cited: 27 Cited Reference Count: 59.

[178] Muller-Buschbaum, P., Roth, S. V., Burghammer, M., Bauer, E., Pfister, S., David, C., und Riekel, C.; Local defects in thin polymer films: a scanning sub-microbeam grazing incidence small angle scattering investigation; In *8th International Conference on Surface X-Ray and Neutron Scattering (SXNS-8)*, pages 148–151, Bad Honnef, GERMANY, 2004. Elsevier Science Bv; ISI Document Delivery No.: 901VB Times Cited: 1 Cited Reference Count: 11.

[179] Wolkenhauer, M., Bumbu, G. G., Cheng, Y., Roth, S. V., und Gutmann, J. S., *Applied Physics Letters* **2006**, *89*(5), 3, Investigation of micromechanical cantilever sensors with microfocus grazing incidence small-angle X-ray scattering.

[180] www.python.org.

[181] www.scipy.org.

[182] Muller-Buschbaum, P., Gutmann, J. S., Lorenz, C., Schmitt, T., und Stamm, M., *Macromolecules* **1998**, *31*(26), 9265–9272, Decay of interface correlation in thin polymer films.

[183] Gutmann, J. S., Muller-Buschbaum, P., Schubert, D. W., Stribeck, N., Smilgies, D., und Stamm, M.; Roughness correlations in ultra-thin polymer blend films; In *6th International Conference on X-ray and Neutron Scattering*, pages 40–44, Noordwijkerhout, Netherlands, 1999. Elsevier Science Bv; ISI Document Delivery No.: 307CF Times Cited: 14 Cited Reference Count: 26.

[184] Beaucage, G., *Journal of Applied Crystallography* **1995**, *28*, 717–728, Approximations leading to a unified exponential power-law approach to small-angle scattering.

[185] Beaucage, G., *Journal of Applied Crystallography* **1996**, *29*, 134–146, Small-angle scattering from polymeric mass fractals of arbitrary mass-fractal dimension.

[186] Beaucage, G., Rane, S., Sukumaran, S., Satkowski, M. M., Schechtman, L. A., und Doi, Y., *Macromolecules* **1997**, *30*(14), 4158–4162, Persistence length of isotactic poly(hydroxy butyrate).

[187] Lenz, S., Bonini, M., Nett, S. K., Lechmann, M. C., Emmerling, S., Kappes, R., Memesa, M., Timmann, A., Roth, S., und Gutmann, J., *The European Physical Journal - Applied Physics* **2009**, *submitted*, Global scattering functions: A tool for Grazing Incidence Small Angle X-Ray Scattering (GISAXS) data analysis of low correlated lateral structures.

[188] Keller, R. N. und Wycoff, H. D., *Inorganic Syntheses* **1946**, *2*, 1–4, Copper(I) Chloride.

[189] Cammarata, L., Kazarian, S. G., Salter, P. A., und Welton, T., *Physical Chemistry Chemical Physics* **2001**, *3*(23), 5192–5200, Molecular states of water in room temperature ionic liquids.

[190] Deshmukh, M. V., Vaidya, A. A., Kulkarni, M. G., Rajamohanan, P. R., und Ganapathy, S., *Polymer* **2000**, *41*(22), 7951–7960, LCST in poly(N-isopropylacrylamide) copolymers: high resolution proton NMR investigations.

[191] Gittins, D. I. und Caruso, F., *Angewandte Chemie-International Edition* **2001**, *40*(16), 3001–3004, Spontaneous phase transfer of nanoparticulate metals from organic to aqueous media.

[192] http://www.bmcm.de/us/pr-usb-pio.html, **2009**.

[193] **2009**, http://www.enthought.com/.

A. Publications

Peer reviewed articles

1. Pericet-Camara, R., Best, A., **Nett, S. K.**, Gutmann, J. S., und Bonaccurso, E., *Opt. Express* **2007**, *15*(15), 9877–9882, Arrays of microlenses with variable focal lengths fabricated by restructuring polymer surfaces with an ink-jet device.

2. **Nett, S. K.**, Kircher, G., und Gutmann, J. S., *Macromolecular Chemistry and Physics* **2009**, *submitted*, PMMA Brushes Prepared in an Ionic Liquid.

3. Bradley, C., Jalili, N., **Nett, S.K.**, Chu, L., Förch, R., Gutmann, J. S., und Berger, R., *Macromolecular Chemistry and Physics* **2009**, *submitted*, Response Characteristics of Thermal Responsive Polymers using Nanomechancial Cantilever Sensors.

4. Lenz, S., Bonini, M., **Nett, S.K.**, Lechmann, M. C., Emmerling, S., Kappes, R., Memesa, M., Timmann, A., Roth, S., und Gutmann, J., *The European Physical Journal - Applied Physics* **2009**, *submitted*, Global scattering functions: A tool for Grazing Incidence Small Angle X-Ray Scattering (GISAXS) data analysis of low correlated lateral structures.

Proceedings

1. **S.K. Nett**, Memesa M., Chen Y., Roth S. V., Gutmann J.S.; DNA-b-PPO coated micro mechanical cantilever arrays studied with micro-focus GISAXS; Annual HASYLAB report **2006**.

2. Cheng, Y.-J., M. Memesa, **Nett, S.K.**, J. S. Gutmann: Crystalline Titania Nanoplatelet Templated by Block Copolymer of PMMA-b-PEO and its

Photophysical Properties. *Mater. Res. Soc. Symp. Proc.*, **2007**, 974, CC10-29

3. **Nett, S.K.**, Memesa, M., Cheng, Y., Lenz, S., Timmann, A., Roth, S.V., Gutmann, J.S.; Analysis of Poly(N-Isopropylamide) brushes on micro cantilevers using μ-GISAXS; Annual HASYLAB report **2007**.

Conference contributions

1. **Sebastian K. Nett**, Gunnar Kircher, Markus Wolkenhauer, and Jochen S. Gutmann; ATRP-Synthesis of Polymer Brushes in aqueous Solution for Silicon Surface Modification; Poster at DPG Tagung Berlin **2006**.

2. **S.K. Nett**, G. Kircher, S.V. Roth, A. Timmann, J.S. Gutmann; Polymer coated micro mechanical cantilever arrays; Poster at HASYLAB Users' Meeting **2007**.

3. **Sebastian K. Nett**, Gunnar Kircher, and Jochen S. Gutmann; Polymer coated micro mechanical cantilever arrays; Poster DPG Tagung Berlin **2007**.

4. **S.K. Nett**, S. Lenz, M. Memesa, Y. Cheng, G. Kircher, S.V. Roth, A. Timmann, J.S. Gutmann; Reflectivity experiments using μ-focused GISAXS on μ-mechanical cantilevers; Poster at 2nd workshop on GISAXS Hamburg **2007**.

5. **S.K. Nett**, S. Lenz, M. Memesa, Y. Cheng, G. Kircher, S. V. Roth, A. Timmann, J.S. Gutmann; Reflectivity experiments using μ-focused GISAXS on μ-mechanical cantilevers; Poster at HASYLAB Users' Meeting **2008**.

6. **Sebastian K. Nett**, Calvin Bradley, Mine Memesa, Yajun Cheng, Sebastian Lenz, Rdiger Berger, and Jochen S. Gutmann; Poly(N-Isopropylacrylamide) as thermo responsive coating on Microcantilever Sensors; Poster at DPG Tagung Berlin **2008**.

7. **S.K. Nett**, Calvin Bradley, Mine Memesa, Yajun Cheng, Sebastian Lenz, Rdiger Berger, and Jochen S. Gutmann; Poly(N-Isopropylacrylamide) as

thermo responsive coating on Microcantilever Sensors; Poster at Nanomechanical-Cantilever Workshop Mainz **2008**.

8. S. Emmerling, S. Lenz, M. Lechmann, R. Kappes, **S.K. Nett**, Y. Zhang, R. Berger, J.S. Gutmann; μ-GISAXS investigation of functional surfaces with limited size; Poster at HASYLAB Users' Meeting **2009**.

B. Software

B.1. NPL Program for Video Assisted Drop Positioning

Printing on NCS is realized with the following NPL-Program. A sample holder is used with four positions for NCS [50]. For this holder a predefined workplate layout "cell_MCS_4+WSP.npw" exists which can be used with the program. On the target "manual grabber points" were set by hand using the video microscope. Then the program red the positions and spots on these positions. With slight modifications the program can also used for other targets in the same way.

```
program Disp_Grabber_Points;
#include "..\Lib\WashSampleCheck_Normal.inc"
var xy0, xy1:tPoint;
var kindTarget, kindTarget_group, targetId, id,
    trows, tcols, i, j, nPoints, n, nDrops,
    wellRow, wellCol, dispTips, MCS_Pos, Tip, cycles: integer;
    holder:string;
var x1, y1, x0, y0, Z_manual, airGap, dry_time:real;

function n_GrabPoints(tarId:integer):integer;
var xy_n: tPoint;
    n, r, c, n_spots :integer;
begin
r:=GetRows(tarId);
c:=GetColumns(tarId);
n_spots := r*c;   // the data of the points is obviously
                  // stored in a col row layout with one Col
Writeln("Cols:", c);
Writeln("Rows:", r);
Writeln("n_spots:", n_spots);
n_GrabPoints := n_spots; //
end;//function
```

```
begin
PositionAbsoluteZ( z=0.0 );
// Set z-value for Dispensing !! Set carefully!!
Z_manual := 44; //For NCS sample holder

// Userinput of values
wellRow := 1;
wellCol := 1;
airGap := 0;
nDrops := 1;
MCS_Pos = 1;
Tip := 1;
cycles := 1;
dry_time := 1;

Window( "Parameters", "MCS-Position:", MCS_Pos, "Number of Droplets:", nDrops,
        "Tip: ", Tip, "Cycles: ", cycles, "Dry Time: ", dry_time);

//"Sample Well-Row", wellRow, "Sample Well-Col", wellCol

//MCS Postion
if MCS_Pos = 1 then holder = "target_1";
if MCS_Pos = 2 then holder = "target_2";
if MCS_Pos = 3 then holder = "target_3";
if MCS_Pos = 4 then holder = "target_4";
if MCS_Pos = 5 then holder = "target_5";

dispTips=1;
if (dispTips <> 0) then
begin
// First we find a target with the name "target"
kindTarget_group := 2;
kindTarget := 3;
targetId := -1;
id := GetFirstObject();
while id >= 0 do /**/
begin
if GetKind( object=id) = kindTarget then
begin
if ToLower(Substring(GetName(id), 0,8 )) = holder then
// Dispensing of Droplets on Manual Grabberpoints
begin
targetId := id;

nPoints := n_GrabPoints(tarId=targetId);
Writeln( "Points = ", nPoints);
for i := 1 to cycles do
begin
for n := 1 to nPoints do
begin
```

```
xy0 := GetPoint( object=targetId, index=n);
PositionAbsoluteXY( tip=Tip, x=xy0.x, y=xy0.y );
PositionAbsoluteZ( z=Z_manual);
PipetteDispense( tip_list=Tip, droplets=nDrops );
end; //for Dispense
//Pipette wieder auf 0 fahren
PositionAbsoluteZ( z=0.0 );
//Camera to x0,y0, Turn on Grabberwindow
PositionAbsoluteXY( tip=-1, x=xy0.x, y=xy0.y );
SetLiveVideo( on=true);
ShowGrabWindow();
TimerDelay( t=dry_time );
end; //for-loop cycles
break;
end; //if string abfrage
end; // if kindtarget
id := GetNextObject();
end; //while id
end; //if dispTips
end. //prog
```

B.2. NPL Program for Automated Printing of PEM

The following program is for dispensing a line structure of polyelectrolyte solutions with two Nanotips and automated wash and dry step with two passive tips. By the factor `delta` an offset between PAH and PSS solutions is introduced. The procedure for the wash and dry step is in the library `WashDry_with_PassiveTips.inc` which is put subsequent to the program.

```
program Automated_PEM_Structure;
#include "..\Lib\WashDry_with_PassiveTips.inc"

var dispHeight, dispSpeed:real;
var tarId, tarRow, tarCol, blockRow, blockCol, spotRow, spotCol:integer;
var state, dispTip, nDrops, dispTips:integer;
var Rinse, alternate:boolean;
var Tips, cycle, t, n_x_Lines, n_y_Lines, i, j, n:integer;
var lineLength, lineDistance, shift, xS, yS,
  x_Center, y_Center, adsorpT, delta_shift, freq:real;

var x0:array[0..20] of real;
var y0:array[0..20] of real;
```

```
var x1:array[0..20] of real;
var y1:array[0..20] of real;

begin
//Startparmeter
cycle = 1; //Number of Bilayers
dispSpeed := 5; //Set the dispensespeed for ADP-Function 3.5
freq := 100; \\Frequency for pipette
PipetteSetFrequency( tip_list=[], f=freq);
dispTips := [1,2]; //Used Tips!!!!
//DispenseHeigth
dispHeight := 32.45; //for trough
//Get Target Information
tarRow=1;
tarCol=1;
//Put in right Target Group name
tarId=GetTargetId( target_group_id=Slide, row=tarRow, column=tarCol);
x_Center := GetObjValue( object=tarId, valueIndex=4)+
(GetObjValue( object=tarId, valueIndex=1)/2);
y_Center := GetObjValue( object=tarId, valueIndex=5)+
(GetObjValue( object=tarId, valueIndex=2)/2);

//Line Parameter
n_x_Lines := 5;
n_y_Lines := 5;
lineLength := 4;
lineDistance := 1;
shift := 0.0; //to get offset between Lines of PSS and PAH
delta_shift := 0.05; //to increase the offset every 2 Lines
alternate := false;
adsorpT := 5;

//UserInput
Window( "Parameters", "Cycles: ", cycle, "# x-Lines: ", n_x_Lines,
"# y-Lines: ", n_y_Lines, "Alternate: ", alternate);

//Get Line Coordinates
//Coordinates of Matrix Point 1,1 as Reference Position
x0[0] = GetX( object=tarId, column=1 );
y0[0] = GetY( object=tarId, row=1 );

//Inital Positon on Spotmatrix
PositionAbsoluteZ( z=0 );
PositionAbsoluteXY( tip=Tips, x=x0[0], y=y0[0] );
PositionAbsoluteZ( z=dispHeight );

for t := 1 to cycle do
begin
    //Dispense Solution a) with Pipette1
    Tips := [1];
```

```
n := 0;
xS := x0[0];
for i:=1 to n_x_Lines do
begin
    x0[i] := xS;
    y0[i] := y0[0]-n*lineDistance;
    x1[i] := xS+lineLength;
    y1[i] := y0[0]-n*lineDistance;

    //Print Line
    PositionAbsoluteXY( tip=Tips, x=x0[i], y=y0[i] );
    PositionAbsoluteZ( z=dispHeight );
    ADP_DispenseLine( refTip=Tips, tipList=Tips, x0=x0[i],
    y0=y0[i], x1=x1[i], y1=y1[i], speed=dispSpeed);

    n := n+1;
end; //n_x_Lines

TimerDelay( t=adsorpT );
//automated Wash and Dry cycle
WashDry_Sample(x = x_Center, y = y_Center, targetHeight=
dispHeight, washVol = 150);

//Dispense Solution b) with Pipette2
Tips := [2];
n := 0;
xS := x0[0];
for i:=1 to n_x_Lines do
begin
    Writeln("Shift: ", shift);
    x0[i] := xS;
    y0[i] := y0[0]-n*lineDistance-shift;
    x1[i] := xS+lineLength;
    y1[i] := y0[0]-n*lineDistance-shift;

    //Every 2 Lines the shift between PAH and PSS is raised about
    //delta_shift
    if i mod 2 == 0 then shift := shift + delta_shift;

    Writeln ("Start x,y: ", x0[i], y0[i]);
    Writeln ("End x,y: ", x1[i], y1[i]);
    //Print Line
    PositionAbsoluteXY( tip=Tips, x=x0[i], y=y0[i] );
    PositionAbsoluteZ( z=dispHeight );
    ADP_DispenseLine( refTip=Tips, tipList=Tips, x0=x0[i], y0=y0[i],
     x1=x1[i], y1=y1[i], speed=dispSpeed);
    n :=n+1;
end; //n_x_Lines

PositionAbsoluteZ( z=0 );
```

```
    TimerDelay( t=adsorpT );
    //automated Wash and Dry cycle
    WashDry_Sample(x = x_Center, y = y_Center, targetHeight=
    dispHeight, washVol = 150);

    Writeln("Cycles: ", t);
end; //for cycle
end.
```

B.3. NPL Library for Automated Wash and Dry Step

This library can be included to any NPL programm with the command
`#include "..\Lib\WashDry_with_PassiveTips.inc"`

```
/**
Function uses 2 Passive Tips for flushing a surface with water
and drys by a nitrogen stream
Tip3 for washing
Tip4 for drying
external program: Ventilsteuerung.exe opens/ closes valve for N2

function WashDry_Sample(x : real x Position for Washing,
                        y : real y Postion for Washing,
                        targetHeight : real Height of Target,
                        washVol : real volume of water for flushing);

**/
//function wash at x,y z with washVol l of water
//dry the sample with a N2 flow by Ventilsteuerung

function WashDry_Sample(x:real, y:real, targetHeight: real, washVol:real):void;

var dispFlow, washX, washY, dryX, dryY:real;
var washTip, posTip, execHdl:integer;

begin

    washTip := [3]; //Passive Tip for washing
    posTip := [1]; //Tip as reference for positioning ???????Anpassen
    dispFlow := 300; //Flow for dispenser
    //x,y Positons for washing and drying
    washX := x;
    washY := y-18;
```

```
dryX := x;
dryY := y-27; //9mm between each tip
PositionAbsoluteZ( z=0 );
//1st Washstep
DiluterSetValveSystemFluid( tip_list=washTip );
DiluterLoad( tip_list=washTip, volume=washVol, flow=dispFlow, wait = 0);
PositionAbsoluteXY( tip=posTip, x=washX, y=washY );
PositionAbsoluteZ( z=targetHeight-5 );
DiluterWaitWhileBusy( tip_list=[]);//Wichtig, da wait = 0 fuer DiluterLoad
//Flush water on surface
DiluterSetValvePipette( tip_list=washTip );
DiluterDispense( tip_list=washTip, volume=washVol, flow=dispFlow );
//1st Dry step with 4. passive tip
PositionAbsoluteXY( tip=posTip, x=washX, y=washY-20 );
//Program Ventilsteuerung.exe
execHdl := Exec( command="C:/Ventilsteuerung2.exe", wait = 0 ); //open
TimerDelay( t=1, 1 );
PositionAbsoluteXY( tip=posTip, x=dryX, y=dryY );
PositionAbsoluteZ( z=targetHeight-5 );
TimerDelay( t=1, 1 );
Terminate(execHdl); //Terminates external program
//Move back to wash postion
PositionAbsoluteXY( tip=posTip, x=washX, y=washY );
execHdl := Exec( command="C:/Ventilsteuerung2.exe", wait = 0 ); //closed
TimerDelay( t=1, 1 );
Terminate(execHdl); //Terminates external program
//2nd Wash
DiluterSetValveSystemFluid( tip_list=washTip );
DiluterLoad( tip_list=washTip, volume=washVol, flow=dispFlow, wait = 0);
PositionAbsoluteXY( tip=posTip, x=washX, y=washY );
PositionAbsoluteZ( z=targetHeight-5 );
DiluterWaitWhileBusy( tip_list=[]);//Wichtig, da wait = 0 fuer DiluterLoad
//Flush water on surface
DiluterSetValvePipette( tip_list=washTip );
DiluterDispense( tip_list=washTip, volume=washVol, flow=dispFlow );
//2ndDry
//Dry with N2-Flow via 4.Passive Tip
//Program Ventilsteuerung.exe
PositionAbsoluteXY( tip=posTip, x=washX, y=washY-20 );
execHdl := Exec( command="C:/Ventilsteuerung2.exe", wait = 0 ); //open
TimerDelay( t=1, 1 );
PositionAbsoluteXY( tip=posTip, x=dryX-1, y=dryY-8 );
PositionAbsoluteZ( z=targetHeight-5 );
TimerDelay( t=1, 1 );
Terminate(execHdl); //Terminates external program
//Move back to wash postion
PositionAbsoluteXY( tip=posTip, x=washX, y=dryY );
execHdl := Exec( command="C:/Ventilsteuerung2.exe", wait = 0 ); //close
TimerDelay( t=1, 1 );
Terminate(execHdl); //Terminates external program
```

```
    execHdl := Exec( command="C:/Ventilsteuerung2.exe", wait = 0 ); //open
    TimerDelay( t=2, 1 );
    Terminate(execHdl); //Terminates external program
    execHdl := Exec( command="C:/Ventilsteuerung2.exe", wait = 0 ); //close
    TimerDelay( t=1, 1 );
    Terminate(execHdl);  //Terminates external program
    PositionAbsoluteZ( z=0 );
end; //endfunction

//function wash at x,y z with washVol l of water
//dry the sample with a N2 flow by Ventilsteuerung
function WashManual_DryAuto_Sample(x:real, y:real, targetHeight: real, washVol:real):void;

var dispFlow, washX, washY, dryX, dryY:real;
var washTip, posTip, execHdl:integer;

begin
    washTip := [3]; //Passive Tip for washing
    posTip := [1]; //Tip as reference for positioning ???????Anpassen
    dispFlow := 300; //Flow for dispenser

    //x,y Positons for washing and drying
    washX := x;
    washY := y-18;
    dryX := x;
    dryY := y-27; //9mm between each tip
    PositionAbsoluteZ( z=0 );
    //1st manual Washstep
    PositionAbsoluteXY( tip=posTip, x=washX+20, y=washY );
    //Ask for manual wash
    Confirmation( title="!!WASH!!", question="Did you rinse the wafer?");
    //1st Dry step with 4. passive tip
    PositionAbsoluteXY( tip=posTip, x=dryX+9, y=dryY+5 );
    PositionAbsoluteZ( z=targetHeight-6 );
    //Program Ventilsteuerung.exe
    execHdl := Exec( command="C:/Ventilsteuerung2.exe", wait = 0 ); //open
    TimerDelay( t=1, 1 );
    PositionAbsoluteXY( tip=posTip, x=dryX-9, y=dryY-5, speed = 5 );
    TimerDelay( t=0.5, 1 );
    PositionAbsoluteXY( tip=posTip, x=dryX-9, y=dryY+5, speed = 20);
    //PositionAbsoluteXY( tip=posTip, x=dryX+9, y=dryY-5, speed = 5 );
    //TimerDelay( t=02, 1 );
    //PositionAbsoluteXY( tip=posTip, x=dryX-9, y=dryY+5, speed = 5 );
    //PositionAbsoluteZ( z=targetHeight-6 );
    //TimerDelay( t=0.5, 1 );
    Terminate(execHdl); //Terminates external program
    //Move back to wash postion
    //PositionAbsoluteXY( tip=posTip, x=washX, y=washY );
    execHdl := Exec( command="C:/Ventilsteuerung2.exe", wait = 0 ); //closed
    TimerDelay( t=1, 1 );
```

```
    Terminate(execHdl); //Terminates external program
    PositionAbsoluteZ( z=0 );
end; //endfunction
```

B.4. NPL Program to Print Circular Structures

The program uses an algorithm to calculate the drop positions for a circle on a n-dimensional raster. The algorithm is based on the work of Bresenham 1965 [136] and Pitteway 1967 [137].

```
program Print_Circle;
function plot_circle(targetID:integer, dispHeight:real,
 r:integer, xmittel:integer, ymittel:integer, Tip:integer, nDrops:integer):void;
 var x_calc:array[1..200] of integer;
 var y_calc:array[1..200] of integer;
 var x, y, fehler, xp, yp, i,n: integer;
 var speed: real;

begin
//Parameter
speed := 500; //movement of tip: PositiontToBlock()
SetState( object=targetID );
PositionToBlock( tip=Tip, object=targetID, blockRow=1, blockColumn=1,
 spotRow=xmittel, spotColumn=ymittel );
PositionAbsoluteZ( z=dispHeight );

//Bresenham Algorithmus aus Skript I-Net
x := 0;
y := r;
fehler := 1-r;
i := 1;

x_calc[i] := 0;
y_calc[i] := r;
while x < y do
begin
    i := i+1; //increment to put x,y to array of variables
    x := x+1;
    if fehler<0 then
    begin
        fehler := fehler + 2*x-1;
    end; //if
    else
    begin
        fehler := fehler + 2*(x-y);
```

```
        y = y - 1;
    end; //else

    x_calc[i] := x;
    y_calc[i] := y;

end; //while
//Octant 1
for n:= 1 to i do
begin
    xp := xmittel+x_calc[n];
    yp := ymittel+y_calc[n];
    PositionToBlock( tip=Tip, object=targetID, blockRow=1, blockColumn=1,
     spotRow=xp, spotColumn=yp, speed=speed );
    PipetteDispense( tip_list=Tip, droplets=nDrops );
    SetState( object=targetID, state=2, row=xp, column=yp );
end;

//Octant 2
for n:=i to 2 step -1 do
begin
    xp := ymittel+y_calc[n];
    yp := xmittel+x_calc[n];
    PositionToBlock( tip=Tip, object=targetID, blockRow=1, blockColumn=1,
     spotRow=xp, spotColumn=yp, speed=speed  );
    PipetteDispense( tip_list=Tip, droplets=nDrops );
    SetState( object=targetID, state=2, row=xp, column=yp );
end;

//Octant 3
for n:=1 to i step 1 do
begin
    xp := ymittel+y_calc[n];
    yp := (xmittel-x_calc[n]);
    PositionToBlock( tip=Tip, object=targetID, blockRow=1, blockColumn=1,
     spotRow=xp, spotColumn=yp, speed=speed  );
    PipetteDispense( tip_list=Tip, droplets=nDrops );
    SetState( object=targetID, state=2, row=xp, column=yp );
end;

//Octant 4
for n:=i to 2 step -1 do
begin
    xp := xmittel+x_calc[n];
    yp := (ymittel-y_calc[n]);
    PositionToBlock( tip=Tip, object=targetID, blockRow=1, blockColumn=1,
     spotRow=xp, spotColumn=yp, speed=speed  );
    PipetteDispense( tip_list=Tip, droplets=nDrops );
    SetState( object=targetID, state=2, row=xp, column=yp );
end;
```

```
//Octant 5
for n:= 1 to i do
begin
    xp := xmittel-x_calc[n];
    yp := (ymittel-y_calc[n]);
    PositionToBlock( tip=Tip, object=targetID, blockRow=1, blockColumn=1,
     spotRow=xp, spotColumn=yp, speed=speed  );
    PipetteDispense( tip_list=Tip, droplets=nDrops );
    SetState( object=targetID, state=2, row=xp, column=yp );
end;

//Octant 6
for n:=i to 2 step -1 do
begin
    xp := ymittel-y_calc[n];
    yp := xmittel-x_calc[n];
    PositionToBlock( tip=Tip, object=targetID, blockRow=1, blockColumn=1,
     spotRow=xp, spotColumn=yp, speed=speed  );
    PipetteDispense( tip_list=Tip, droplets=nDrops );
    SetState( object=targetID, state=2, row=xp, column=yp );
end;

//Octant 7
for n:=1 to i step 1 do
begin
    xp := ymittel-y_calc[n];
    yp := (xmittel+x_calc[n]);
    PositionToBlock( tip=Tip, object=targetID, blockRow=1, blockColumn=1,
     spotRow=xp, spotColumn=yp, speed=speed  );
    PipetteDispense( tip_list=Tip, droplets=nDrops );
    SetState( object=targetID, state=2, row=xp, column=yp );
end;

//Octant 8
for n:=i to 2 step -1 do
begin
    xp := xmittel-x_calc[n];
    yp := (ymittel+y_calc[n]);
    PositionToBlock( tip=Tip, object=targetID, blockRow=1, blockColumn=1,
     spotRow=xp, spotColumn=yp, speed=speed  );
    PipetteDispense( tip_list=Tip, droplets=nDrops );
    SetState( object=targetID, state=2, row=xp, column=yp );
end;

PositionAbsoluteZ( z=0 );

end; //end of function plot_circle

var R, Xmittel, Ymittel: integer;
```

```
var dispHeight, speed: real;
var tarID, nDrops, Tips, j, cycles: integer;
var Rinse:boolean;

begin
//Parameter
Xmittel := 16;
Ymittel := 16;
R := 14;
dispHeight := 35.3;
tarID := 2; //slide0101 auf Workplate misc_trough_PEML.npw
nDrops := 3;
cycles := 10;
speed := 500;

for j=1 to cycles do
begin
    //plot circle with Tip 1
    Tips := [1];
    plot_circle(targetID=tarID, dispHeight=dispHeight, r=R,
                xmittel=Xmittel, ymittel=Ymittel, Tip=Tips, nDrops=nDrops);
    //Stop for Rinsing
    Rinse := Confirmation( title="Rinse Break", question="Did you rinse the wafer?");
    //plot circle with Tip 2
    Tips := [2];
    plot_circle(targetID=tarID, dispHeight=dispHeight, r=R,
                xmittel=Xmittel, ymittel=Ymittel, Tip=Tips, nDrops=nDrops);
    //Stop for Rinsing
    Rinse := Confirmation( title="Rinse Break", question="Did you rinse the wafer?");
    Writeln("Cycle #: ", j);
end;
end.
```

B.5. Program to Operate N_2 Valve

The N_2 valve is an electromagnetic valve, which is operated by an electronic switch connected to a USB controller. The USB controller is a "DIGITAL PC MEASURING SYSTEM - USB-PIO" from BMC Messsysteme GMbH, Germany. The program is written in C++ and is compiled into an executable program. When the program is executed then it checks the switch status and it changes the valve status to either open or close. In order to compile the software the drivers and the program library for the USB-PIO has to be installed. It can be downloaded from the manufacturer homepage [192].

```
#include <stdio.h>
#import "C:\Programme\BMC Messsysteme\ActiveX\memx.ocx"

int mempio_Port1_On()
{
MEMXLib::_DmeMPIOPtr pio;
pio.CreateInstance(__uuidof(MEMXLib::meMPIO));
if(pio == NULL) {
printf("PIO ActiveX not installed...\n");
return 1;
}
pio->CardId = 1;
pio->DirPort1 = MEMXLib::DirOut;
pio->SetLine(1, 1);
return 0;
}

int mempio_Port1_Off()
{
MEMXLib::_DmeMPIOPtr pio;
pio.CreateInstance(__uuidof(MEMXLib::meMPIO));
if(pio == NULL) {
printf("PIO ActiveX not installed...\n");
return 1;
}
pio->CardId = 1;
pio->DirPort1 = MEMXLib::DirOut;
pio->ResetLine(1, 1);
return 0;
}

int mempio_Port1_status()
{
MEMXLib::_DmeMPIOPtr pio;
pio.CreateInstance(__uuidof(MEMXLib::meMPIO));
if(pio == NULL) {
printf("PIO ActiveX not installed...\n");
return 1;
}
pio->CardId = 1;
if (pio->GetLine(1, 1) == 1){
return 1;
}
else {  return 0;
}

}

int main(int argc, char *argv[])
{
```

```
// get OLE up and running...
HRESULT result = OleInitialize(NULL);
if(!SUCCEEDED(result)) {
printf("Failed to initialize OLE\n");
exit(1);
}
if (mempio_Port1_status() == 0) {
mempio_Port1_On();
}
else { mempio_Port1_Off();
}

OleUninitialize();
return 0;
}
```

B.6. Script for Reflectivity Data Analysis

The following script is written in phyton (Version 2.5) and uses the libraries: SciPy 0.7.0, NumPy 1.2.1, Python Imaging Library 1.1.6, Matplotlib 0.98.5.2. Enthought is offering a complete installation on their webpage containing all libraries [193]. The analyzing software is divided into two parts: (i) a modul called bw4tiff.py, (ii) a script for analyzing. The general steps, how the data is analyzed, can be found in chapter 6.2

Modul bw4tiff.py

```
from scipy.misc.pilutil import *
import Image
import re
import os
import datetime
#from types import *


class bw4tiff:
 p_isMotorname = re.compile('!\s*Motorname:\w*')
 p_isNPoints = re.compile('!\s*Number of Points:\w*')
 p_isAccTime = re.compile('!\s*Accumulationtime:\w*')
 p_isCounter = re.compile('!\s*c\d+:\w*')
 p_isExposure = re.compile('!MarCCD\w*')
 p_isCouterData = re.compile('(\d*\s*)*')
```

```
p_isCommentLine= re.compile('!\w*')

def __init__(self, name):
 # initialize member variables
 self.name = name
 self.image = None
 self.date = None
 self.exp_info=dict()
 #self.counter_info=dict()
 self.counters=dict()
 self.basename = None
 self.basepath = None
 self.normalization="Unity"
 self.normalization_factor=1.0
 self.background=10.0
 self.ai=None
 self.lsd = None   #in Units of meters
 self.pixsize=None # in Units of LSD
 self.Dqx=None
 self.Dqy=None
 self.Dqz=None
 self.Prim_Beam_x = None
 self.Prim_Beam_y = None

 if self.is_tiff():
  # first we read the tiff data
  dummy_data = Image.open(self.name)
  # this is an 'I16' type tiff file which we silently upgrade to 'I'  and 'F'
  # in order to be able to convert it to a numpy array
  dummy_data = dummy_data.convert("I")
  dummy_data = dummy_data.convert("F")
  # Now we convert it to a numpy array called 'image'
  self.image = fromimage(dummy_data)
  del dummy_data
  # Now we parse the filename to be able to open the associated
  #   .dat file
  dotpos = self.name.rfind('.')
  # we now know where the extention starts
  # let's find out where the filename starts
  filename_start=self.name.rfind(os.sep)+1
  # basename is the filename w/o extention
  self.basename=self.name[filename_start:dotpos]
  # basepath is the file path w/o filename
  self.basepath=name[:filename_start]
  #print self.basename
  #print self.basepath
  self.parse_adjunct_datfile()


def parse_adjunct_datfile(self):
```

```
# depending on what numbering scheme we have, we take a different
# approach on parsing the associated .dat file
# (and on it's name creation)
#
# if the filename follows the scheme
# xxxxx_<5 digit no.>_<4 digit no.>
if re.compile("\w*_[0-9]{5}_[0-9]{4}$").match(self.basename):
# now we need to assemble the name
# and parse the .dat file
uspos = self.basename.rfind('_')
# we assume that we have a lowercase '.dat' extention only!!
datname=self.basepath+self.basename[:uspos]+".dat"
elif re.compile("\w*_[0-9]{5}$").match(self.basename):
# now we need to assemble the name
# and parse the .dat file
# we assume that we have a lowercase '.dat' extention only!!
datname=self.basepath+self.basename+".dat"
#
# Now we know which file to open and ty to open it
try:
 #print "trying to read "+datname
 f=open(datname, 'r')
except IOError:
 print 'Error opening ', datname
else:
# if we are here we were actually ale to execute the try statement
# so we continue to parse the file
#
# Now we scan over the lines in the file until we reach its end
# In each line parse its content ans read an additional line
#  if neccesary
for line in f:
if self.p_isMotorname.match(line) or self.p_isNPoints.match(line) or
   self.p_isAccTime.match(line) :
#we have found the '! Motorname' string
#OR we have found the '! Number of Points:' string
#OR we have found the '! Accumulationtime:' string
line = line.strip(' !')
data = line.split(',')
for elem in data:
    elem = elem.strip()
    token = elem.split(':')
    self.exp_info[token[0].strip()]=token[1].strip()
    #
    elif self.p_isCounter.match(line) :
    #we have found the '! d[0-9]:' string
    line = line.strip(' !')
    token = line.split(':')
    self.counters[token[0].strip()]=token[1].strip()
    #CounterNumber=???
```

```
  # we also find the number in the counter label
  m= re.match(".(\d+)", token[0])
  if m :
  self.counters[token[1].strip()]=int(m.group(1).strip())
  #
  elif self.p_isExposure.match(line) :
  #we have found the '!MarCCD' string
  line = line.strip(' !')
  data = line.split()
  isRightLine = None
  for i in range(len(data)):
    elem = data[i].strip()
    #print "analyzing "+elem
    # are we at the filename
    #!!! Be carefull that we do not check for multipple f's and case sensitivity
    if elem.endswith('.tif'):
    # we need to check, if the filename matches the basename
    if elem.find(self.basename)>=0 :
    isRightLine = 1
    #print "found right line"
    #we are at the right line, so we need to read the counters
    nextline = f.next()
    cntrs = nextline.strip().split()
    # Now we need to store the counters in the appropriate dict
    for j in range(len(cntrs)):
      # DON'T forgett that the numbering of counters starts at 1!
      # store BOTH values as integer Numbers
      self.counters[(j+1)]=int(cntrs[j])
      # are we at the part of the line, containing the measurement date
      if re.match("at", elem) and isRightLine:
      # if so, save assemble and the date
      date = data[i+1].strip(' ,').split('.')
      time = data[i+2].strip(' ,').split(':')
      self.date = datetime.datetime(int(date[2]), int(date[1]), int(date[0]),
                  int(time[0]), int(time[1]), int(time[2]), 0, None)
      # are we at the end of the line, containing the motor position
      if re.match("position:", elem) and isRightLine :
        # if so, save it
        self.exp_info[elem]=float(data[i+1].strip())
#
elif self.p_isCouterData.match(line) :
  #we have found the Counter data line
  pass
elif self.p_isCommentLine.match(line) :
  #we have found the '!' string
pass
else :
print "ERROR in parse_adjunct_datfile while reading the line: \n",line,"\n"

    f.close()
```

```
  #
def is_tiff(self):
  # This is a crude version, since it does not accept .tiff endings.
  # However this is the current state at BW4 so we are content with this
  # for now
  return self.name.lower().endswith('.tif')

def normalize_to(self, normfac, normname):
  # Set the normalization factor to
  self.normalization_factor = float(normfac)
  self.normalization = normname
  #self.normalization = str(self.normalization_factor)

def set_background(self, back):
  # Set the normalization factor to
  self.background = back

def normalize_to_counter(self, counter):
  ocounter = counter
  # first we check whether the value
  # associated with the key 'counter' is a number or not...
  # and if the associated dict entry is a number as well
  while (self.counters.has_key(counter) and isinstance(counter, int)
     and isinstance(self.counters[counter], int)) != True :
  # if this is not the case replace the old key
  # with the argument and  try again
  counter = self.counters[counter]
  #
  # technically we do not need to doulble check, but just to be save...
  if (self.counters.has_key(counter) and isinstance(counter, int)) :
  # if the key is a number...
    if isinstance(self.counters[counter] ,int):
    # and the argument is also a number and we can proceed straight away
      normfac = float(self.counters[counter])
      normname = str(ocounter)
    else :
     # if the key is a number but the argument is not
     #  something very strange has happened...
     # so e try to exit gracefully
     print "Unable to determine the normalization factor..."
     print "resetting normalization to unity..."
     normfac = 1
     normname ="Unity"
    # Set the normalization factor to the determined values
    self.normalization_factor = normfac
    self.normalization = normname

def get_image(self):
  return self.image
```

```
  def get_normalized_image(self):
    return (self.image-self.background)/self.normalization_factor

  ##Put by s.nett
  def get_norm_image(self):
    return (self.image-self.background)

  def set_primary_beam(self, x, y):
    self.Prim_Beam_x=x
    self.Prim_Beam_x=x

  def set_callibration_values(self, LSD, pixsize, ai):
    self.LSD = LSD
    self.pixsize = pixsize
    self.ai = ai
```

B.6.1. Script for Analysis

This is an example script which has to be modified for other data files.

```
import os
from bw4tiff_c import bw4tiff
from matplotlib import *
from scipy.io import write_array
from pylab import *
import fit_lib
import numpy
import pprint
import re
# psyco goes here
# Import Psyco if available
try:
import psyco
psyco.full()
print "Using psyco...."
except ImportError:
pass
# here we start the actual script
# read dir D:\gutmann\GISAXS\2006-08-24_11~44\gutmann0806
basedir = 'D:'+os.sep+'GISAXS'+os.sep+'Gutmann1208'
        +os.sep+'sn_a84'+os.sep+'c2'+os.sep
outdir = 'D:'+os.sep+'GISAXS'+os.sep+'gutmann1208'
        +os.sep+'Auswertung'+os.sep+'sn_a84'+os.sep

teststr_arr = ['sn_a84_refc2_']
#teststr_arr = ['sn_bl20_refs2_']
```

```
# Linear regression (incident angle/motor pos vs. Detector channel)
# of the measured data
# use this to determine a cut-out of interesting fit regions
#m=-918.557 #for gutmann0806
#b=1712.93  #for gutmann0806
#m = -838.5 #for gutmann0207
#b = 1461.2 #for gutmann0207
#m = -899.4 #for gutmann0407
#b = 1635.7 #for gutmann0407
m = -866.3 #for gutmann1208
b = 1722.5 #for gutmann1208

def lr_res(x, m, b):
return (m*x + b)

fwhm_box = 41.0

ion()
print basedir

#
# Version w/o envocation of a function
for teststr in teststr_arr:
refl_arr = numpy.array([])
chan_arr = numpy.array([])
mpos_arr = numpy.array([])
Ibox_arr = numpy.array([])
for bdir, subdirs, fls in os.walk(basedir):

for f in fls:
fullf = os.path.join(bdir,f)
ext = os.path.splitext(f)
#if os.path.islink(fullf): break
if (os.path.isfile(fullf) and re.compile
                ("\w*"+teststr+"\w*").match(f) and re.compile(".tif").match(ext[1])) :
# Hier sollten dann andere Dinge stehen
t = bw4tiff(fullf)
t.normalize_to_counter('c1')
i = t.get_normalized_image()
tp = t.exp_info["position:"]
ll = int(lr_res(tp,m,b)-(0.5*(fwhm_box-1.0)))
ul = int(lr_res(tp,m,b)+(0.5*(fwhm_box-1.0)))

c=i[ll:ul,983:1060]
y=numpy.sum(c,1)
x = arange(y.size)
# giving initial parameters
x0 = y.argmax()
sigma = 3.0
A = y.max()
```

```
p = fit_lib.fit_gauss(x, y, A, x0, sigma)
Ibox = sum(y,0)
A,x0,sigma = p[0]

# Append Data to the transfer arrays
mpos_arr=numpy.append(mpos_arr, [float(tp)])
refl_arr=numpy.append(refl_arr, [A])
chan_arr=numpy.append(chan_arr, [x0])
Ibox_arr=numpy.append(Ibox_arr, [Ibox])

t = None
else:
pass
print "writing output"
oa=numpy.array([mpos_arr, refl_arr, Ibox_arr, chan_arr]).transpose()
save(outdir+teststr+"_ref_ana.dat", oa, fmt='%8.8g')
print "done"
ylabel('Intensity /a.u.')
xlabel('Angle /Degree')
figure(1)
semilogy(mpos_arr, refl_arr, 'b+')
draw()
savefig(outdir+teststr+"C2_ref_ana_sum.png")
ylabel('Intensity /a.u.')
xlabel('Angle /Degree')
figure(2)
semilogy(mpos_arr, Ibox_arr, 'b+')
draw()
savefig(outdir+teststr+"C2_ref_ana_gauss.png")

ioff()
show()
```

C. Miscellaneous

C.1. Liquid Properties

Table C.1.: The characteristic properties of the liquids used in chapter 3.5: Boiling point BP, surface tension γ, Vapor pressure p_0, viscosity η, density ρ, contact angle θ. All values are at 20°C if not stated else.

Solvent	BP /°C	γ /mN/m	p_0 /mbar	η /mPa*s	ρ g/cm^3	θ /°
Dimethylformamide	153	36	3.7	0.92	0.95	66
Methylmethacrylate	101	20	40	0.6	0.94	43
[Bmim][PF_6]	??	48	$<< 0$	281	1.37	

C.2. Gasflowsystem

In order to have a defined humidity inside of the environmental cell of the Scentris setup (see section 2.6) the gasflowsystem was build by Masaya Toda in corporation with the electronic lab. Figure C.80 shows the layout of the system. It is possible to switch directly between a pure nitrogen stream and a nitrogen stream containing a defined amount of water vapor while the flow rate kept constant at 0.5 mL/min.

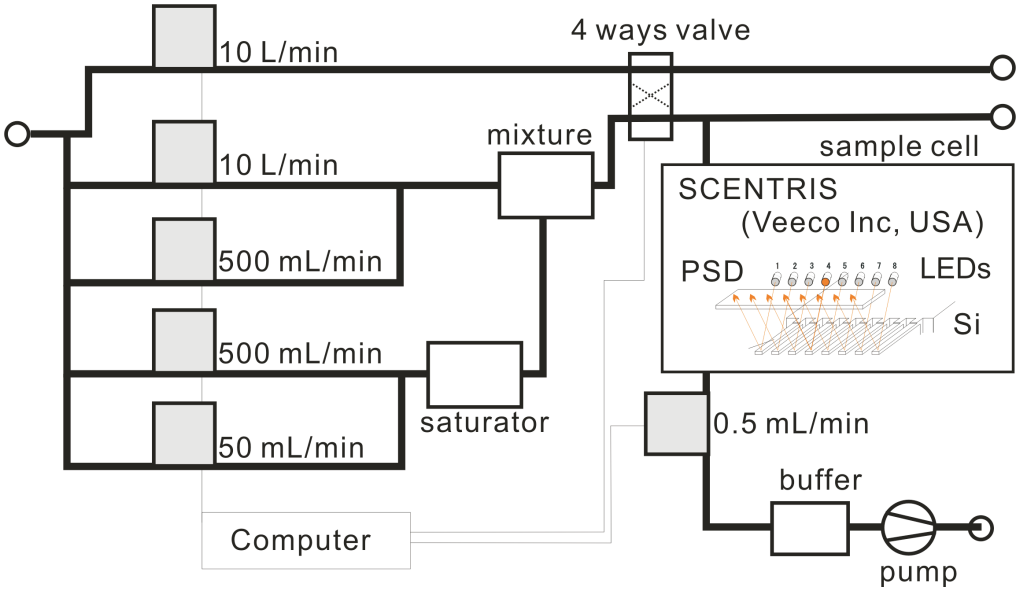

Fig. C.80.: Gasflowsystem to control the humidity from 5 to 80 % in the environmental sample cell used in the Scentris system (see section 2.6).